Faustino Wahaia

SPECTROSCOPIC AND IMAGING TECHNIQUES USING TERAHERTZ FREQUENCY BAND FOR BIOMEDICAL APPLICATIONS

Supervisor: *Prof. Luis Miguel Bernardo*

Thesis submitted to the Faculty of Sciences of the University of Porto for the degree of PhD in Physics

Department of Physics and Astronomy Faculty of Sciences of the University of Porto

2011

To Vincenza

Without you this work would have been almost impossible.

THANK YOU SO MUCH

Acknowledgements

Many people have participated in this work and I feel indebted for their help and support. And many others albeit not directly involved, have decisively contributed to make the present work possible. Particularly I would like to thank:

First, The Calouste Gulbenkian Foundation, for having attributed me the Doctoral Scholarship for four years (E-191746);

My Supervisor, Prof Luis Miguel Bernardo, for having accepted me as his PhD student, for his non-stop accompaniment of my progress in the work and for providing all the conditions to keep my work running and for giving me the responsibility and the opportunity in this work;

My Supervisor at Institute of Semiconductor Physics of Vilnius, Prof Gintaras Valusis for having received me at ISP and guided my first steps in to the word of terahertz electronics, for being always available to clear my otherwise insurmountable beginner's doubts, and for providing very insightful comments throughout the experimental sessions at the ISP;

To my colleagues of IFIMUP Francisco Marinho, Helder Crespo, João Silva, José António, Patricia Silva, Alexandra Angra Amorim and Miguel Miranda;

To my colleagues at ISP for their help, support and friendship, Dalius Saliuta, Irmantas Kasalynas, Jan Makutkevic, Ramunas Adomavicius and Rasa Suzanovicienê;

To the staff of the FCUP workshop, Francisco Carpinteiro and Carlos Torres specially.

Resumo

O presente trabalho descreve o desenvolvimento e a validação de técnicas de imagem e espectroscopia no diagnóstico de cancro, usando a banda de frequências terahertz. São introduzidos métodos teóricos para a determinação da origem do contraste observado nos espectros dos coeficientes de absorção e indices de refracção, obtidos por espectroscopia terahertz, e nas imagens terahertz, com tecido biológico normal e afectado por cancro. Especificamente, os tecidos estudados no presente trabalho foram os do colon e recto, em diferentes fases de desenvolvimento de cancro nomeadamente desde o tecido em estado normal ao estado mais avançado. O estudo experimental foi feito em amostras de tecido biologico da mesma tipologia e tratadas segundo procedimentos histopatológicos normalizados como a fixação em formol e/ou embebimento em parafina. O presente estudo demonstra que é possível distinguir o tecido normal do afectado por cancro, usando as técnicas de espectroscopia e imagem terahertz. Neste estudo são apresentados gráficos de curvas de coeficientes de absorção e índices de refracção correspondentes a tecidos normais e afectados por cancro assim como imagens de transmissão terahertz em 2D. Os resultados do presente trabalho são discutidos e, são estabelecidas as melhores condições de discriminação entre tecidos normais e cancerosos.

Abstract

The present thesis describes the development and validation of imaging and spectroscopic techniques for diagnosis of cancer in humans at THz frequency. Theoretical methods are introduced to determine the origin of the contrast observed in the absorption coefficients and refractive indices spectra of THz spectroscopy measurements and in the images of healthy and, affected biological tissues. The specific biological cancer tissues investigated in this thesis have been colon and rectal tissues in different phases of cancer development from healthy to strongly affected regions. The experimental studies have been made in samples, from the same tissue typology, treated by the standard histopathologic procedures as formalin-fixation and paraffin-embedding. The study shows that it is possible to distinguish between healthy and cancer affected tissue, using the terahertz spectroscopic and imaging techniques. Plots of the absorption coefficient and the index of refraction of healthy and cancer affected tissues as well as 2-D transmission THz images are presented. The experimental results are discussed and the best conditions for the tissues discrimination are established.

List of Publications

Paper in international peer review

- Colon Cancer detection by THz Techniques*;* Faustino Wahaia, Luis M. Bernardo, Gintaras Valusis, Jan Macutkevic, Irmantas Kasalynas and Dalius Seliuta - *submitted to the Journal of Biomedical Optics.*

- Detection of colon and rectum cancers by terahertz techniques, Faustino Wahaia, Luis M. Bernardo, Gintaras Valusis, Jan Macutkevic, Irmantas Kasalynas and Dalius Seliuta. Proc. SPIE 7715, 77152U (2010); doi:10.1117/12.847849.

International Conferences

- Detection of colon cancer by THz Techniques; Faustino Wahaia, Luis M. Bernardo, Gintaras Valusis, Jan Macutkevic, Irmantas Kasalynas and Dalius Seliuta - International Conference on Applications of Optics and Photonics, Braga, Portugal, 3-7 May 2011.

- Detection of colorectal cancer using THz Techniques; Faustino Wahaia, Luis M. Bernardo, Gintaras Valusis, Jan Macutkevic, Irmantas Kasalynas and Dalius Seliuta - Photonics Europe International Symposium, Brussels, Belgium, 12-16 April 2010.

- Detection of colon and rectum cancer by THz Techniques; Faustino Wahaia, Luis M. Bernardo, Gintaras Valusis, Jan Macutkevic, Irmantas Kasalynas and Dalius Seliuta - 1st Porto Workshop on Sources of Super-intense and Ultrashort Laser Pulses, 27 October 2009.

- Detection of colon and rectum cancer by THz Techniques, Faustino Wahaia, Luis M. Bernardo, Gintaras Valusis, Jan Macutkevic, Irmantas Kasalynas and Dalius

Seliuta - 15th Semiconducting and Insulating Materials Conference, 15-19 June 2009, Vilnius Lithuania.

National Conferences and Communications

- *Detection of colon cancer using THz Techniques*, Faustino Wahaia, Luís M. Bernardo, VI Jornadas IFIMUP February 2011 - Faculty of Sciences, University of Porto/Physics Department
- *Detection of colon and rectum cancer using THz Techniques*, Faustino Wahaia, Luís M. Bernardo, INESC Workshop, Instituto Superior Técnico de Lisboa (IST) Outubro 2009, Lisboa
- *Detection of colon and rectum cancer using THz Techniques*, Faustino Wahaia, Luís M. Bernardo, V Jornadas IFIMUP May 2009 - Faculty of Sciences, University of Porto/Physics Department
- *Terahertz Techniques for Detection of colorectal cancer using THz Techniques*, Faustino Wahaia, Luís M. Bernardo, IV Jornadas IFIMUP Juny 2008 - Faculty of Sciences, University of Porto/Physics Department
- *Introduction to THz Techniques for Biomedical Applications*, Faustino Wahaia, Luís M. Bernardo, III Jornadas IFIMUP 2007 - Instituto de Física dos Materiais da Universidade do Porto, Maio 2007

Contents

List of Figures

List of Tables

List of Abbreviations

BPD-DD	Balanced photodiode differential detector
BNA	Benzyl nitroaniline
BS	Beam splitter
BWO	Backward-wave oscillator
CWTI	Continuous wave THz imaging
DAST	Dimethylamino stilbazolium tonsylate
DC	Direct current
DFG	Difference frequency generation
DNA	Dioxi-nucleic acid
DR	Dynamic range
EO	Electro-optic
EOS	Electro-optic sampling
FWHM	Full width at half maximum
FEL	Free electron laser
FFT	Fast Fourier transform
FTS	Fourier transform spectroscopy
GIT	Gastrointestinal tract
IR	Infrared

ISP	Institute of semiconductor physics
LIA	Lock-in amplifier
LT-GaAs	Low temperature grown gallium arsenide
KDP	Potassium dihydrogen phosphate
MRI	Magnetic resonance imaging
NIR	Near infrared
OAPM	Off-axis parabolic mirror
OPB	Optical probe beam
PCA	Photoconductive antenna
PET	Positron emission tomography
QCL	Quantum cascade laser
RNA	Ribo-nuclei acid
SIC	Silicon carbide element
SNR	Signal-to-noise ratio
TDTS	Time-domain THz spectroscopy
TPI	Terahertz pulsed imaging
TTDTS	Transmission time-domain
TCWTI	Transmission continuous wave
THz	Terahertz
WP	Wolaston prism

Chapter 1

Introduction

1.1 Background

The Terahertz (1 THz = 1012 Hz) band lies between microwave and infrared region of the electromagnetic spectrum, as shown in Figure 1.1 The wavelength extends typically from 0.3 mm to 3 mm and consequently the frequency from 0.1 THz to 10 THz and the wavenumber from 3.33 to 333 cm^{-1}.

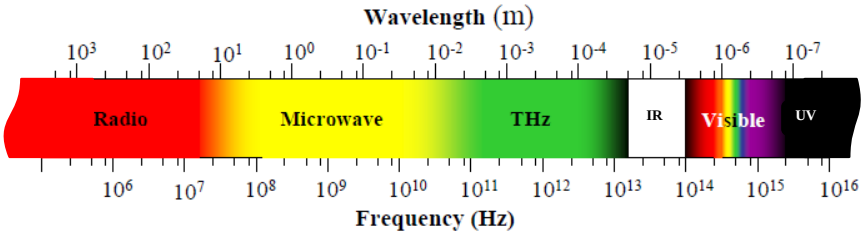

Figure 1.1: Spectrum of electromagnetic radiation showing the location of the terahertz (THz) range.

Since the pioneering research work in the THz frequency region initiated in 1975 [14–16] THz techniques are experiencing a huge development boom. David Auston at AT&T Bell Laboratories developed a photoconductive emitter, able to produce a single pulse of THz radiation after being stimulation by a short optical pulse [17],The invention of the mode-locked Ti:sapphire laser – generating ultrashort light pulses at a high repetition rate – helped to develop the photoconductive THz generation and opened the THz frequency region to spectroscopic studies.

Terahertz radiation is non-ionising and it penetrates a wide variety of non-polar materials such as clothing, paper, cardboard, wood, masonry, plastic and ceramics. However it is strongly absorbed by polar molecules, such as water, and it is highly reflected by

metals. Currently, THz imaging and spectroscopy are being developed and applied in different areas, such as physics, chemistry, medicine, defence, security, etc.

Time-domain THz-imaging and spectroscopy – employing the method of coherent gated detection, used in this work – are currently implemented by many research groups for applications in medicine. Biological fat tissue, bone, teeth and soft living tissue have been imaged, with the average power even below the level of blackbody radiation. Aimed to de detection of anomalies in tissues, associated with diseases, such techniques will hopefully become powerful research tools to contribute for the solution of the important health and social problems associated, for example, with cancer.

Since the water absorbs strongly in all THz frequency range, it limits the depth of biological tissue that can be tested in THz imaging and spectroscopy. As the water is one of the main constituents of biological tissues, the tissues penetration depth of THz radiation ranges from typically a few hundred microns in high water content tissues (muscle and adipose tissue) to several centimetres in tissues with a high fat content [18–21]. In the first tissue demonstration of THz imaging, it was possible to distinguish the muscle and fat porcine tissues. The different water content in these tissues was assumed to be responsible for the contrast. Since the publication of these results, the number of reported biomedical studies using THz has greatly increased including teeth and artificial skin models [18, 22], healthy skin and basal cell carcinoma in both vitro and in vivo [18,23]. Some of them exploit the sensitivity of the THz absorption to water, using the degree of hydration as a measure of tissue disease state [19, 21, 23]. Others have highlighted the contrast between normal (health) and diseased tissue [22, 24, 25]. assuming it was mainly due to differences in the fundamental properties of the tissues and its imbalances caused by the presence of a disease [26].

1.2 The Scope and Motivation of this Thesis Work

The present work is aimed to explore the potential of the new THz imaging and spectroscopy techniques, which are non-invasive and non-time consuming. Many biomolecules have resonant peaks in the terahertz range, associated to vibrational ou rotational modes and intermolecular interactions in the frequency interval of 0.1 – 10 THz. Therefore, the spectroscopic response of biological tissues contents a vast amount of information. These techniques are expected to bring a comprehensive screening and diagnostic of human diseases, particularly in the case of cancers which is the subject of this thesis work.

According to estimation by WHO, more than 85% of all cancers are difficult to detect in early phases and the clinicians recur to excision biopsy to remove parts of body

tissue for examination under microscope. This procedure has the inconveniences of time consuming and painful histopathological actions. We hope the THz techniques based in this thesis may help to decrease that percentage and to eliminate those inconveniences.

In this work we intend to demonstrate the ability of transmission time-domain THz spectroscopy (TDTS) and continuous wave terahertz imaging (CWTI) to distinguish basal cell carcinoma and other forms of malignancies (benign and normal tissue associated with cancer and related diseases), both in vitro and in vivo. Besides the proposed diagnostic, we hope this thesis could also (a) contribute to a better understanding of THz pulse propagation through complex media and (b) help in the development of a cost effective diagnostic THz endoscopic device, able to provide access to internal epithelial surfaces for early cancer detection, and finally (c) contribute to the development of major opportunities for the THz science into medicine.

1.3 Experimental Approach

In the present work, the experimental approach was building a TDTS set-up using photoconductive antennas for both transmitter and receiver. With this setup, experimental measurements have been performed and data have been collected and processed to determine frequency-dependent constants of measured biological tissues. Then, CWTI system has been set-up in order to scan samples of both normal and cancer affected regions.

1.4 Major Contribution of this Work

The novelties of this research work are: (1) Is one of the few studies ever done in colon cancer detection by THz techniques; (2) Is the first time that a comparative study is realized between formalin-fixed and paraffin-embedded colon tissues in order to determine whether there are additional contrast-contributing factors other than water; the study compares the results of TDTS and CWTI for two types of tissue histopathologic preparation (formalin-fixation, and drying and paraffin-embedding) of colon tissue. It confirms the findings of other researchers in the field that the observed contrast in TDTS and THz imaging measurements is not only caused by the increased water content in cancer tissue but there are other factors contributing to it; the research found that, even existing many other contrast factor, water content variations in respect to normal water presence in biological tissue structures could warn for a disease presence; (3) two techniques have been used, TDTS for absorption coefficient and refractive index spectra analysis and CWTI for image analysis, both on the same samples and at the same environment conditions.

1.5 Limitations

Preparation, conservation and handling of biological samples may cause some changes to the tissues that make difficult the generalization of the conclusions of the laboratory experiments. The presented results are for ex-vivo samples, but we are confident they can be extended to in-vivo ones.

It has been not possible to have access to a large diversity of biological tissue typologies, affected with cancer, as it would be desirable. It was due to the nature of the samples and the number of institutions and collecting procedures.

The problems associated with the physical conservation of the samples are also relevant. The formalin is 10% neutral buffered formalin (4% formaldehyde ($HCHO$) in phosphate buffered saline) and it is generally used to preserve the biological tissue from degradation, and to maintain the structure of the cells inclusive of sub-cellular components such as cell organelles (e.g., nucleus, endoplasmic reticulum, mitochondria). The formalin fixation preserves tissues or cells mainly by irreversibly cross-linking proteins [27]. Therefore, the main action of these aldehyde fixatives is to cross-link amino groups in proteins through the formation of CH_2 (methylene) linkage, while preserving the structural integrity of the cells and tissue. It can damage the biological functionality of proteins, particularly enzymes, and can also denature them to a certain extent.

The handling of the samples in an optical laboratory environment may also cause some limitations mainly due to dehydration caused by evaporation during set-up preparation and measurements.

1.6 Thesis overview

This thesis is divided in six chapters. In chapter 1, we give a short summary of the THz radiation background, the thesis scope and the motivation which led us to the realization of the present work. Some references of experimental work kicking off and practical challenges and limitations that we have faced. In chapter 2, we introduce fundamental physical principles of the generation and detection processes of THz radiation. Here, we also give an overview of some methods and source materials (LT-GaAs and ZnTe, specially) for both generation and detection. In chapter 3, we present theoretical background over the TDTS, data analysis methods used in this technique with highlight on the spectroscopic extraction of the frequency-dependent constants (the absorption coefficient α and the index of refraction n). In chapter 4, we present the TDTS on biological tissues in ex-vivo. Tissue histological preparation

procedures, a brief discussion on sample preparation and its mounting in TDTS sample holder, and a brief introduction on cancer-cell biology. We also give an account on our experimental study's performance and procedures. In chapter 5, we show the experimental results, data extraction and analysis, and discussions. We compare the spectra of α and n between formalin-fixed with those of paraffin-embedded colonic tissues. We also compare the α maps of the two kinds of samples. In chapter 6 we present our final discussion, conclusions and remarks.

Chapter 2

Theory and background

2.1 Introduction

The invention of TDTS led to a significant rise of research groups in this field. Motivated by the need of understanding the physics of the processes leading to the THz generation and detection, enormous efforts have been taken toward the development of new source materials, propagation models, improvement of generation-detection techniques and its applications, although the basic experimental principles have not undergone significant changes.

In this chapter we review the physical fundamentals related to the generation and detection of THz radiation. We limit our discussion to photoconductive antennas and optical rectification in non-linear crystals. The formalisms used to estimate the optical constants of materials using TDTS will be presented. The conclusions will be applied to explore the properties of biological material.

2.2 Terahertz Pulse Generation

The process of generation and detection of terahertz (THz) radiation using ultrashort laser pulses has been intensively studied during the last decade. In recent years many research groups have studied and developed numerous sources and techniques for generating THz radiation in an effort to thoroughly explore the THz frequency region [17]. Hence, terahertz sources can be broadly classified as incoherent thermal sources, coherent broadband pulsed sources and narrowband continuous-wave sources.

The incoherent thermal sources such as arc lamps or silicon carbide electric heating elements (SiC) emit a very broad range of frequencies among which are THz frequencies.

The majority of broadband pulsed THz sources are based on the excitation of appropriate materials with ultrashort laser pulses where electrons and holes are optically generated due to inter-band absorption of the optical pulses. They are then spatially separated by the electric field or due to the photo-Dember effect which arises from the charge mobility causing the acceleration of the carriers at different rates. A transient photocurrent varying on picosecond time scale generates THz radiation. An alternative mechanism for THz generation is the optical rectification, possible in crystals without inversion symmetry and with a sufficiently large nonlinear susceptibility. Although there are several techniques for the generation of continuous-wave THz radiation, the very common techniques are limited to low power THz radiation ($< 100\mu$W) the so called up-conversion techniques which mostly make use of electronic methods. There are also other techniques such as photo-mixing (optical heterodyne down-conversion), Far-infrared gas lasers, P-Type Ge-lasers, Quantum cascade lasers, etc [17, 28]. One other highly advanced technique is based on semiconductor deposition that allows to be constructed multiple quantum-well semiconductor structures for laser emission (called quantum cascade lasers). It has been demonstrated that these lasers emits at THz frequencies. The major advantage among many others is their small dimensions and emission power in the mW range. Its drawback is the requirement of very low temperatures ($\sim$ 203.1^{0}C or 70K) for better functioning. For more intense THz radiation, the generation techniques are based on the acceleration and deceleration of high energy electron beams in string magnetic fields such as free electron lasers (FEL) and backward wave oscillators (BWO) [29]. Table 2.1 presents the main THz generation and detection techniques.

Table 2.1: Generation and detection techniques associated with continuous-wave and pulsed THz systems

	Emission	**Detection**
Continuous-wave	Free-electron lasers (FEL) Molecular gas lasers Photomixing Quantum Cascade Lasers (QCL) Backward-wave oscillators (BWO)	Goley cell Bolometer Pyroelectric detector Bolometer
Pulsed	Bulk semiconductor surface Optical rectification Optical parametric generation Photoconductive antennas, etc.	Deuterated triglycine sulfate (DTGS) EO sampling Bolometer Photoconductive antenna

Albeit the broad diversity of techniques leading to the THz generation as it was

mentioned above, only photoconductive antennas and optical rectification (a traditional non-linear technique for THz generation), will be taken in account here, despite the last one was not used in the present work.

The THz generation by photoconductive antennas (PCAs) has proved to be the most efficient technique to convert VIS/IR pulses to THz radiation with respect to both intensity and spectral bandwidth [30]. Low-temperature-grown gallium-arsenate (LTG-GaAs) grown by molecular beam epitaxy at low substrate temperatures of about 200^0C followed by a rapid thermal annealing, has been the most widely used for PC-emitter and detector due to their unique properties such as ultrashort carrier lifetime, large resistivity, and relatively good carrier mobility [31].

2.3 Photoconductive Antennas

Photoconductive antennas (PCA), also known as Auston switches, were formerly pioneered by Auston [14] in the mid-1975s when pumping a high-resistivity silicon by a mode-locked Nd:glass laser [16]. Later, they have been developed for free space THz spectrometer applications by Grischkowsky [32]. The PCAs are usually constructed by depositing two electrodes, consisting of two strip-lines separated by $5 - 10\mu$m on a suitable semiconductor material with the right bandgap. This Hertzian dipole-type antenna has typically a width of $10 - 20\mu$m, and a length (L) of $50 - 200\mu$m. In its emitter configuration it is biased with a DC voltage and illuminated with a femtosecond laser pulses. The dipole-type antenna is the most widely used resonant antenna, which emits THz waves with a central wavelength of $\lambda_n = 2L/m$ where λ_n is wavelength in the substrate. The response wavelength in the free space is $\lambda = \lambda_n n$, where n is refractive index of the substrate. L represents the length of the antenna (the distance between the striplines as it will be shown later in this chapter) and m can be any positive integer. There are several PCA electrode configurations of common use. Figure 2.1 illustrates some of these configurations. There is also a nonresonant PCA type with a variable width that can lead to a broader frequency response range. Geometries of this type of PCA include the so called bow-tie, shown in Figure 2.2 (used in this work), spiral, and logarithmic periodic antennas.

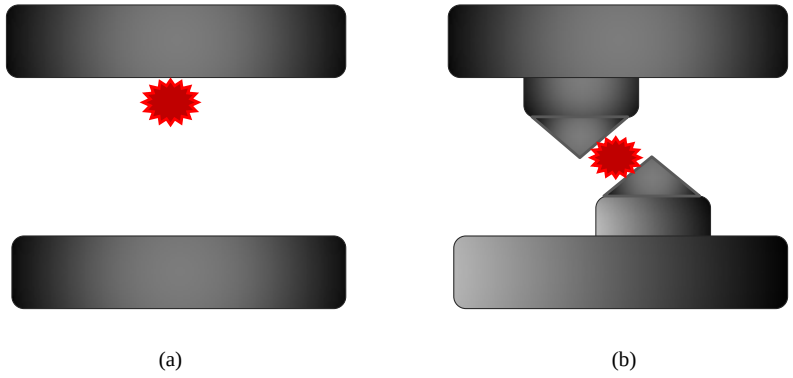

Figure 2.1: PCA electrode configurations. (a) Stripline and (b) offset electrode configuration

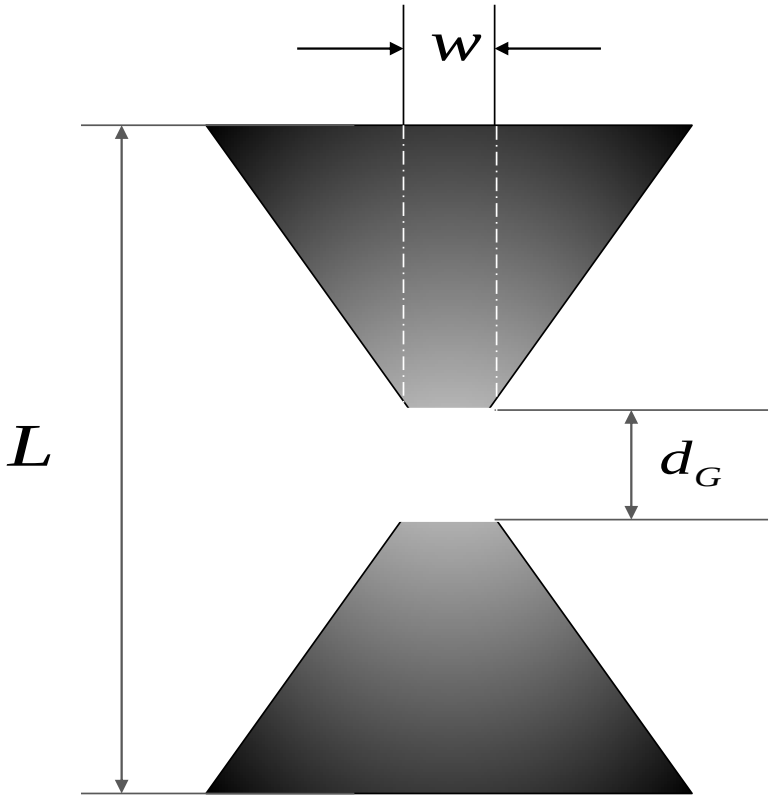

Figure 2.2: Schematic diagram of Bow-tie antenna

2.3.1 Generation of THz Radiation by Photoconductive Antennas

Photoconductive antennas are biased THz emitters and are capable of relatively large average THz powers up to 40 mW [33] and bandwidths as high as $\sim 10\,\mathrm{THz}$ [34]. The

photoconductive antenna uses high-speed photoconductors as transient current sources that generate the radiation, and metallic electrodes are used to bias the photoconductive gap and form the antenna. The physical mechanism for THz wave generation in PCAs is that when a femtosecond (fs) laser pulse with an arbitrary intensity profile $I(t)$, excites a biased semiconductor with photon energy ($E_{ph} = h\nu$) larger than its bandgap (i.e., the energy difference between the bottom of the conduction band and the top of the valence band) energy, $E_g = 1.24\text{eV}.\mu\text{m}/\lambda$, (Figure 2.3) and electron-hole pairs (EHP) are generated due to absorption of laser photons. Figure 2.4 illustrates a biased dipole-type PCA structure and pumped with a femtosecond optical pulse. This type of PCA was used in this work.

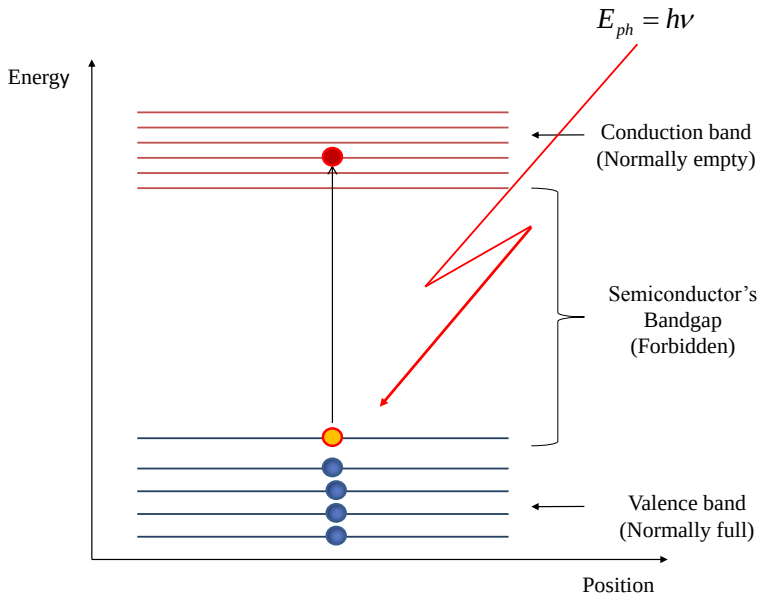

Figure 2.3: Photon absorption process in a semiconductor

For GaAs at room temperature and under normal atmospheric pressure, the bandgap energy is $E_g = 1.42eV$ [35] . The variations of bandgap with temperature is given by [36]

$$E_g(T) = E_g(0) - (\alpha T^2/T + \beta) \tag{2.1}$$

where T is the temperature and α and β are material constants.

Therefore, GaAs is an appropriate semiconductor to be excited by Ti:saphire laser pulses ($\lambda = 0,8\mu$). The rapid change of the density of the photocarriers and their in phase-acceleration due to applied bias field yield a large transient surface current. Consequently, an electromagnetic pulse, proportional to the time derivative of this current, is radiated into the free space (Figure 2.5). The intensity and bandwidth of

the THz radiation are largely affected by the material parameters such as the bandgap, carrier's lifetime, and resistivity.

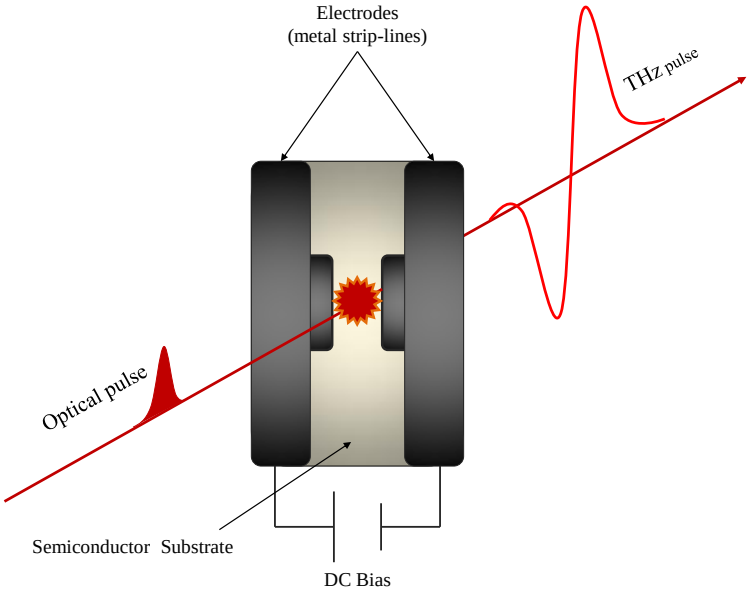

(a) Front view

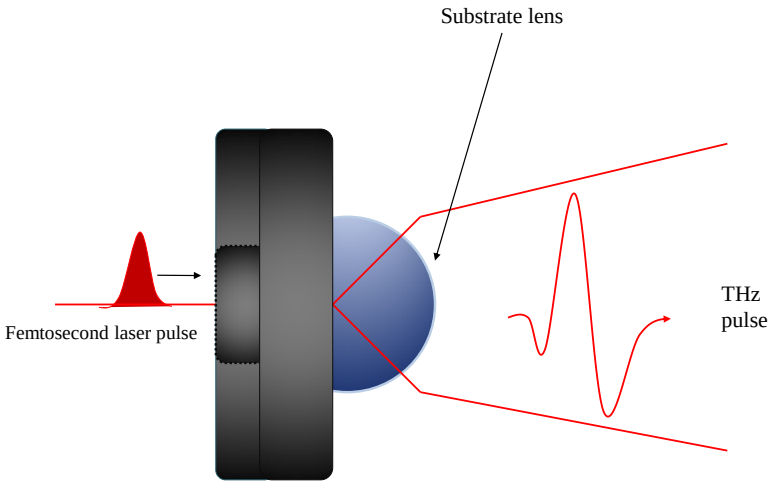

(b) Side view

Figure 2.4: Schematic views of a photo-conductive antenna (PCA): (a) front view (b) side view. A femtosecond laser pulse is shining on the central area of the PCA; electron–hole pairs are created depending on the wavelength (λ) of the laser and the semiconductor structure.

The radiated electric field $E_{THz}(t)$ by the dipole antenna (Figure 2.5), in free space, at a distance r much greater than the wavelength ($r \gg \lambda_{THz}$), far-field, is [37]

$$E_{THz}(t) = \frac{\mu_0}{4\pi}\frac{sin\theta}{r}\frac{d^2}{dt^2}\left[p(t_r)\right]\hat{\theta} \tag{2.2}$$

where $p(t_r)$ is the dipole moment at retarded time, $t_r = t - r/c$, and θ is the angle of direction of the dipole with position vector $\vec{r}$, as shown in Figure 2.5. The derivation of the dipole moment in time yields

$$\frac{dp(t)}{dt} = \frac{d}{dt}\int \rho(r',t)r'd^3r' = \int r'\frac{\partial\rho(r',t)}{\partial t}d^3r' \tag{2.3}$$

where $\rho(r',t)$ is the charge carriers' density. Since $\partial\rho/\partial t = \nabla\cdot\vec{J}$ then,

$$\frac{dp(t)}{dt} = \int r'\nabla\cdot J(r',t)d^3r' = \int J(r',t)d^3r' \tag{2.4}$$

where $J(r',t)$ is the current density, anda assuming unidimensional carriers' transport we obtain

$$\frac{dp(t)}{dt} = \int J(z',t)d^3r' = \int_{-\omega_{0/2}}^{\omega_{0/2}} I_{phc}(z',t)dz' = \omega_0 I_{phc}(t) \tag{2.5}$$

where I_{phc} is the intensity of the photocurrent. Hence the THz electric field can be expressed as [17]:

$$E_{THz}(t) = \frac{\mu_0\omega_0}{4\pi}\frac{\sin\theta}{r}\frac{d}{dt_r}\left(I_{phc}(t_r)\right)\hat{\theta} \propto \frac{dI_{phc}(t)}{dt} \tag{2.6}$$

where μ_0 is the vacuum permittivity, ω_0 is the spot size of the optical beam (usually $\omega_0 \approx 10\mu m < \lambda_{THz} = 300\mu m$ at 1 THz).

The production of ultrashort currents ($\sim$ 1ps lifetime at FWHM) is strongly dependent upon the carrier's lifetime (τ_e for electrons and τ_h for holes) in the semiconductor, GaAs, in this case [38]. The low temperature ($\sim 200^0C$) grown gallium arsenide (LT-GaAs), with and $\tau_e = 0.2$ps and $\tau_h = 0.4$ps, is the most used ultrafast THz emitter semiconductor [39]. Its photo-carriers have a trapping time considerably shorter than their recombination time and the photo-carriers' life-time can be approximated as their trapping time. The time-dependent photocurrent density in the emitter can be expressed as the convolution of the optical pulse envelope with the photocurrent impulse response [40]

$$I_{phc}(t) = \int I_{opt}(t-t')\left[en(t')\upsilon(t)\right]dt' \tag{2.7}$$

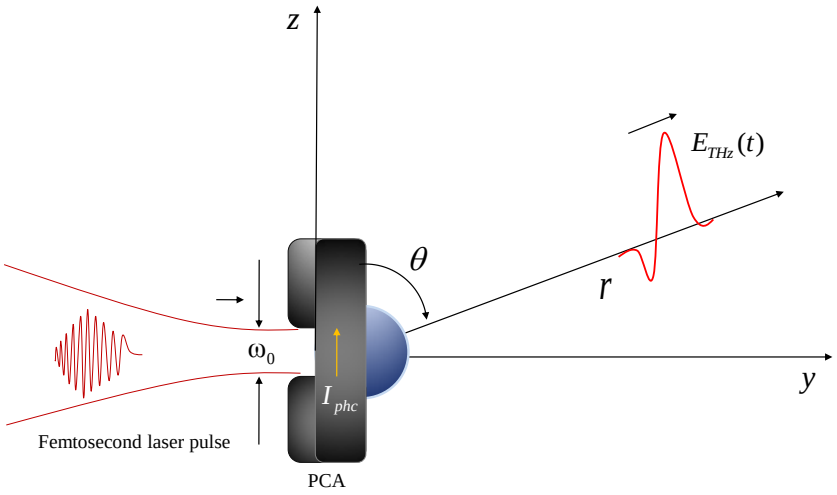

Figure 2.5: Schematic diagram of an electric dipole radiation from a PCA.

where $I(t)$ is the intensity profile of the optical pulse, e is the elemental electron charge, $n(t)$ the carriers' density and $v(t)$ the average electron velocity.

The time-dependent optical intensity is considered to be Gaussian:

$$I_{opt}(t) = \frac{\Phi}{2\sqrt{\pi}\Delta t} \exp\left(-\frac{t^2}{\Delta t^2}\right) \tag{2.8}$$

where,Φ is the total pump optical fluence, $\tau_p = \sqrt{\ln 2}\Delta t$ is the FWHM and Δt is the length of the Gaussian pulse.

The dynamics of the photo-carriers' density under excitation n_{phc} is governed by the following expression:

$$\frac{dn_{phc}(t)}{dt} + \frac{n_{phc}(t)}{\tau_{phc}} = \delta(t) \tag{2.9}$$

so

$$n_{phc}(t) = \begin{cases} e^{-t/\tau_{phc}} & \text{for} \quad t > 0 \\ 0 & \text{for} \quad t \leq 0 \end{cases} \tag{2.10}$$

where τ_{PhC} denotes photo-carriers life-time and $\delta(t)$ is a Dirac delta function, denoting the optical impulsive excitation. According to the Drude-Lorentz model (which describes effectively the carrier transport of the photo-generated electron), in the dynamics of the photo-generated free carriers in a semiconductor, the average velocity of the photo-carriers is governed by following differential equation [1],

$$\frac{dv(t)}{dt} = -\frac{v(t)}{\tau_s} + E_{DC}\frac{e}{m_{eff}} \tag{2.11}$$

where v is the average velocity of the carriers, E_{DC} is the DC bias field, considered to be constant, τ_s is the momentum relaxation time, e is the electric charge of the carriers and m_{eff} is the effective mass of the photocarriers (inertial resistance of an electron inside the semiconductor against an acceleration due to the force of applied external electric field). Solving Eq. (2.11), we get the time dependence of average velocity

$$v(t) = \begin{cases} \mu_e E_{DC}\left(1 - e^{-t/\tau_s}\right) & \text{for} \quad t > 0 \\ 0 & \text{for} \quad t \leq 0 \end{cases} \tag{2.12}$$

where the electron mobility is $\mu_e = e\tau_s/m_{eff}$.

Here, we assume that the bias field is constant ($E_{DC} = \text{const.}$) and since the holes are moving too slow compared to the electrons (for the majority of semiconductors $\mu_e \gg \mu_h$) the holes are not taken in account. The integration of equation (2.7) by insertion of the equations (2.10) and (2.12) leads to:

$$\begin{aligned} I_{PhC}(t) &= \int_0^{+\infty} I_{opt} e^{-(t-t')^2/\tau_p^2} e^{-t'/\tau_{PhC}} \mu_e E_{DC}\left(1 - e^{-t'/\tau_s}\right) dt' \\ &= \mu_e E_{DC} I_{opt} \int_0^{+\infty} e^{-(t-t')^2/\tau_p^2 - t'/\tau_{PhC}}\left(1 - e^{-t'/\tau_s}\right) dt' \end{aligned} \tag{2.13}$$

whose solution is

$$\begin{aligned} I_{phc}(t) = &\frac{\sqrt{\pi}}{2}\mu_e E_{DC} I_{opt} \\ &\times \left[\exp\left(\frac{\tau_p^2}{4\tau_{phc}^2} - \frac{t}{\tau_{phc}}\right) \cdot erfc\left(\frac{\tau_p}{2\tau_{phc}} - \frac{t}{\tau_p}\right)\right] \\ &- \exp\left(\frac{\tau_p^2}{4\tau_{phcs}^2} - \frac{t}{\tau_{phcs}}\right) \cdot erfc\left(\frac{\tau_p}{2\tau_{phcs}} - \frac{t}{\tau_p}\right) \end{aligned} \tag{2.14}$$

where

$$\frac{1}{\tau_{phcs}} = \frac{\tau_s + \tau_{phc}}{\tau_{phc}\tau_s} \tag{2.15}$$

and the $erfc$ is the complementary error function

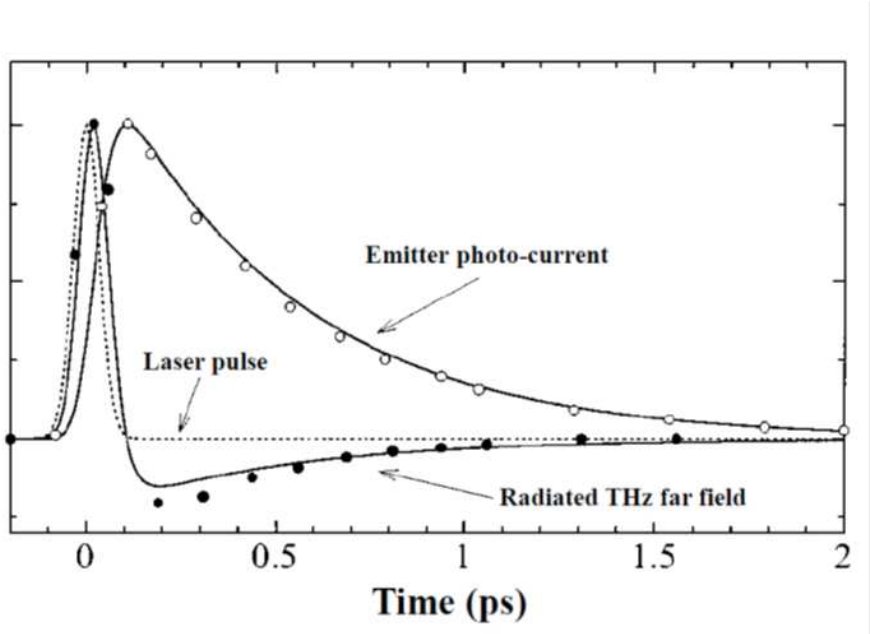

Figure 2.6: The photo-current in the emitter and the electric field amplitude of the corresponding THz far-field radiation as function of time. The dotted line represents the temporal shape of the laser pulse. The circles correspond to experimental data [1].

$$erfc(z) = 1 - erf(z) = \frac{2}{\sqrt{\pi}} \int_{x}^{\infty} e^{-t^2} dt \tag{2.16}$$

In Figure 2.6 is shown the evolution of the photo-current and the respective THz far-field as function of time. They are calculated from equation (2.14) and the equation (2.8) respectively. Here the parameters, photo-carriers' life-time (τ_{PhC}), the momentum relaxation time (τ_s), and the optical pulse duration $\left(\tau_p = \sqrt{\ln 2}\Delta t\right)$ are taken in account.

In a PCA more than 50% of THz radiation is emitted to the substrate side meanwhile approximately the other half is emitted to the free space through the lens substrate. This conclusion is based on the antenna theory that a dipole antenna emits roughly $\varepsilon^{3/2}$ times more power into the dielectric material than into the air [41], where ε is the dielectric constant of the substrate material. For high emission efficiency of a PCA, high carriers' mobility and high voltage breakdown materials are needed. The LT-GaAs semiconductor is used very often in PCA fabrication due to its advantageous characteristic parameters such as the high mobility ($200-400 cm^2/\mathrm{V.s}$), high resistivity ($10^6 \Omega$.cm) and high breakdown voltage ($4 \times 10^5 \mathrm{V}.cm^{-1}$) [42].

In summary, the process of generation of THz radiation from a PCA, illuminated with ultrashort laser pulse, can be regarded as it follows: under optical excitation, a photo-current is generated in the DC-biased PCA and the resulting rapidly changing current

radiates a THz pulse.

2.3.2 Detection of THz radiation by Photoconductive Antennas

Almost two decades ago David H. Austin and co-workers generated and detected, for the first time, THz pulses using PCAs [29]. The generation antenna was biased by 45 V and the detecting antenna was connectes directly to a current amplifier.

The same physical principle that drives the process of THz generation in PCAs also drives the gated detection of THz pulses. Therefore the photo-carriers' dynamics, discussed in the previous section (2.3.1), is applied to the process of THz field detection by PCAs although as an inverse process. Here, the electric field created by the applied voltage (bias) separates the electron–hole pair spatially (Figure 2.7). The electron, which has a higher mobility moves toward the positive contact faster than the hole that moves toward the negative electrode. So that the electron will reach the positive contact first and exit the semiconductor. This creates a net positive charge in the semiconductor, which is compensated by the introduction of an electron by the negatively biased ohmic contact [43].

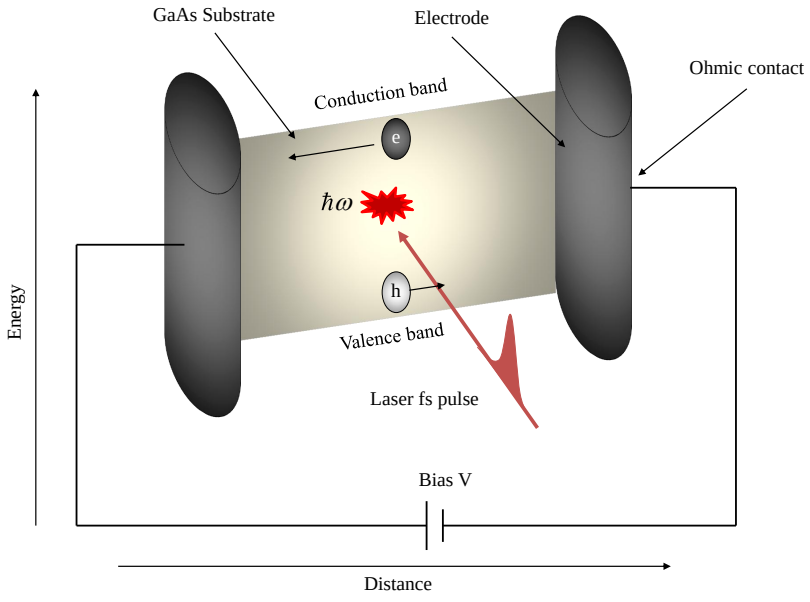

Figure 2.7: A photon is absorbed by an LT-GaAs semiconductor, creating an electron–hole pair.

The electron, with a velocity more than 10 times greater than the hole, traverses the semiconductor and is collected on the positive contact, causing another electron to be

introduced at the negative contact. Meanwhile, the hole is still on the way to reach the negative contact. Finally the hole reaches the negative contact and is collected in the stream of the external circuit. Thus, the length of the photoconductivity event is determined by the transit time of the sluggishly moving photo-carrier (the hole), $t_h = L/\upsilon_h = L_{PC}/\mu_h E$ where the subscript PC stands for photoconductive. Hence, the bandwidth of the detector PC can be determined. During the hole's transit time a number of electrons have traversed the semiconductor and the external circuit in order to maintain charge neutrality. So the one photon shot and its absorption triggers current flow. The ratio of the number of electrons collected per incident photon is the detecting PC gain, given by [44].

$$G_{PC} = \tau/t_e\,(1 + \mu_h/\mu_e) \tag{2.17}$$

where $t_e = L_{PC}/\mu_e E$.

The photoconductivity of the substrate material can be expressed as

$$\Delta\sigma = \lambda e\eta I\tau_s(\mu_e + \mu_h)/chd_{PC} \tag{2.18}$$

where η is the quantum efficiency h is the Planck's constant, $\mu_{e,h}$ are the mobilities of electrons and holes, and d_{PC} is the photocontuctive substrate thickness. The expression is valid only if all incident radiation is absorbed otherwise it must be multiplied by a factor, $1 - exp\,(-\alpha d)$, where α is the absorption coefficient at the working wavelenth, c is the speed of the light in vacuum.

The bandwidth is then determined by the transit time of the holes as follow:

$$B_{PC} = \frac{1}{\pi t_h} = \frac{\mu_h V}{\pi L^2} \tag{2.19}$$

The detection PCA is gated with a femtosecond pulse that was split off from the beam used to excite the generating atenna. Thus, the gating pulse (optical probe pulse (OPP)) creates photocarriers and the THz pulse provides the bias field to create a detectable current (typically in the range of nA) which feeds a current amplifier (Figure 2.9). Usually the output of the current amplifier is connected to a LIA or gated integrator synchronized with a chopper (an optical intensity modulator) for SNR enhancement, and then to a computer. The THz electric field waveform can be mapped out in time domain by measuring the current while the time-delay between the THz pulse and the optical probe beam is varied and controlled on the PC-display.

The photo-current $J(t)$ does not depend only on the incident THz radiation but also on the transient surface conductivity, $\sigma(t)$. Then $J(t)$ can be expressed as a convolution

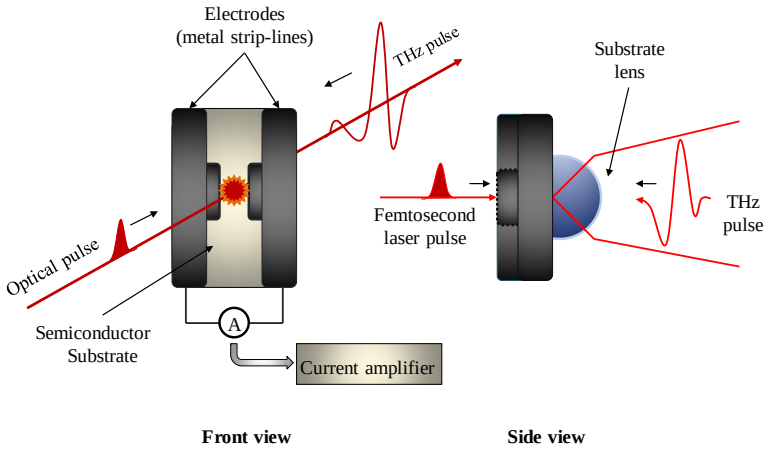

Figure 2.8: Schematic showing the PCA detector

in the following form:

$$J(t) = \int_{\infty}^{t} \sigma_s(t - t')E_{THz}(t')dt' \tag{2.20}$$

where $E_{THz}(t)$ is the THz electric field incident on the PCA gap. The $\sigma_s(t)$ is determined by the optical intensity, carriers' drift velocity and the photocarriers' density [40] [40].

Fourier transformation of the equation (2.20) yields

$$J(\omega) = \sigma_s(\omega)E_{THz}(\omega) \tag{2.21}$$

This result demonstrates that the detection bandwidth of the PCA-transceiver's detector, (Figure 2.8) is limited by the photo-carriers' dynamics in the semiconductor. Figure 2.9 shows roughly the process of THz generation and detection, the main configuration of components and signal analysis.

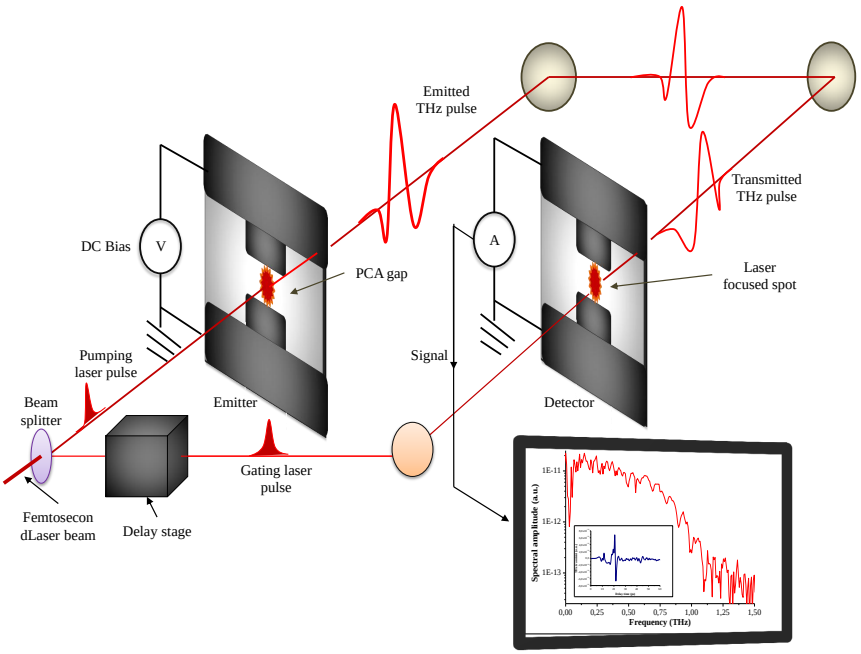

Figure 2.9: Diagram of photoconductive transceiver. The emitter is on the left; the receiver is on the right. The THz pulse is recorded as a function of delay time and the obtained time-domain signal is Fourier-transformed numerically.

To measure the electric field with high temporal resolution, the response-time of the detector, τ_R, has to be short in respect to the rate of change of the THz field. The response time can be estimated convolving the THz electric field $E_{THz}$with the detector's response-time τ_R. Figure 2.10 shows the schematic representation of the THz detection process. The time axis is determined by the delay time between the THz pulse and the gating laser pulse. In Figure 2.10(a), the THz pulse is not yet arrived in the antenna structure, therefore, the current is zero, since the antenna bias voltage, is provided by the THz pulse, and there is no net current flow through the antenna; in Figure 2.10(b) the positive peak of THz pulse is incident on the antenna simultaneously with the laser gating pulse, then current flows from the lower half of the antenna to the upper one; in Figure 2.10(c), the negative peak of the THz pulse is incident on the antenna simultaneously with the laser gating pulse, corresponding to a symmetric situation compared to Figure 2.10(b).

Considering that the laser gating pulse arrives at t=0 and the THz pulse arrives at $t = t_0$, then the time average current can be expressed as follows [45],

$$I(t) = \frac{2Lr\alpha}{w} \int_{-\infty}^{\infty} \sigma_s(t) E_{THz}(t - t_0 - \tau) d\tau \tag{2.22}$$

where, L is the distance between the strip-lines (the length of the dipole), α is the

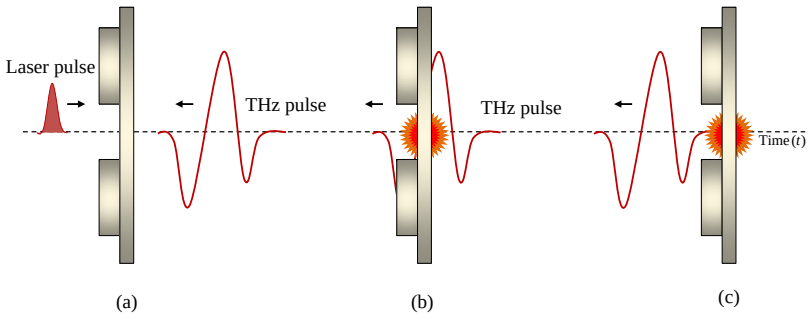

Figure 2.10: Schematic representation of the THz detection process.

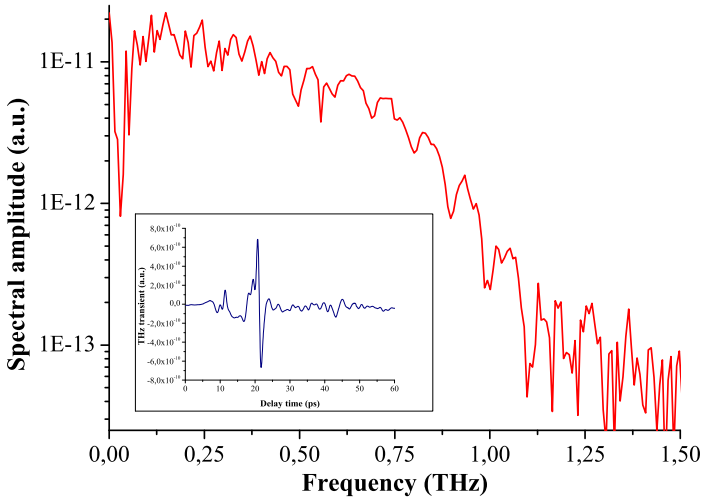

Figure 2.11: Broadband THz time pulse (inset) and its corresponding fast Fourier transform (FFT).

absorption depth in the semiconductor and w is the width of the dipole's gap.

Equation (2.22) indicates that $I(t)$ would be exactly proportional to the THz electric field, if the photoconductor response time was represented by a Dirac $\delta-$function.

This time dependent signal $I(t)$ can be numerically Fourier transformed using Fast Fourier Transform (FFT) and represented in the frequency domain. Figure 2.11 shows a broadband THz pulse in frequency domain with the corresponding time signal (inset). The shape of the detected THz pulse depends on the characteristics of the PCA receiver. Figure 2.12 shows THz signal waveforms detected with PCAs made of different semiconductor materials and the respective FFT spectra.

In summary, the detection is performed by the following way. A micro-scale dipole antenna is stuck on a semiconductor substrate with ultrashort carrier life-time $\leq$ ps [30]. For THz detection, the characteristics of the used PCA semiconductor and the PCA's design (fundamentally, its length, (L = 30-200 μm) are critical features in the efficiency

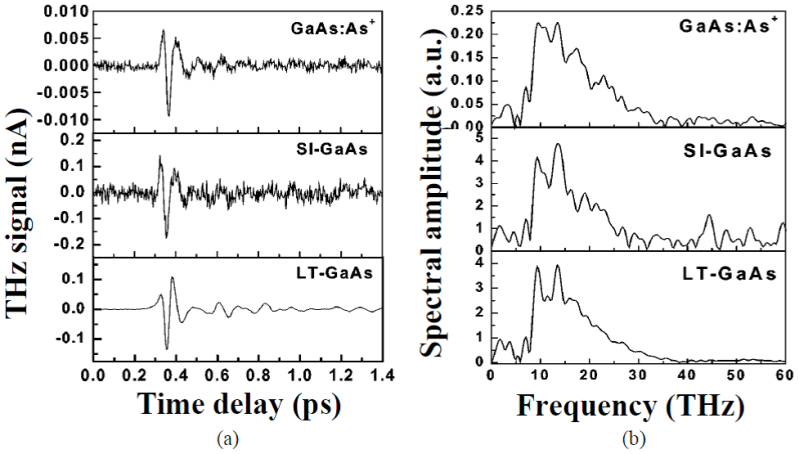

Figure 2.12: Time-resolved THz radiation waveforms emitted by 10 mm ZnTe (110) crystal are detected by different types of PCAs: GaAs:As+, SI-GaAs and LT-GaAs PCA,s Image representing detection of broadband THz field. (a) time signals; (b) corresponding FFT spectral amplitudes [2].

of the detector (Figure 2.13).

The antenna's width w is tens of micrometers and the antenna's gap $d_G = 5 - 10\,\mu m$ is approximately equal to the gating laser focus spot (d_{opt}), $\geq 5\,\mu$m. The ultrafast laser pulse knocking onto the PCA's gap generates electron-hole pair (see section 2.3.1) decreasing the conductivity of the gap because of the ultrashort recombination time τ_{ph} of the carriers. The arrival of the laser pulse works as a switch. It makes the gap resistance to change (in a picosecond time-scale), from quasi-insulating ($\rho \approx 10^7\,\Omega.cm$ for LT-GaAs [40]) to conducting and from conducting to quasi-insulating and so on.

The gap resistance is given by

$$R_G(t) = w/\sigma(t)A \tag{2.23}$$

where A is the gap cross section area and approximately equal to $2d\alpha$ where α is the absorption coefficient and $1/\alpha$ represents the absorption depth in the semiconductor.

2.3.3 Materials for PCAs

The semiconductor materials mostly used for THz generation and detection are indicated with their characteristics in the Table 2.2.

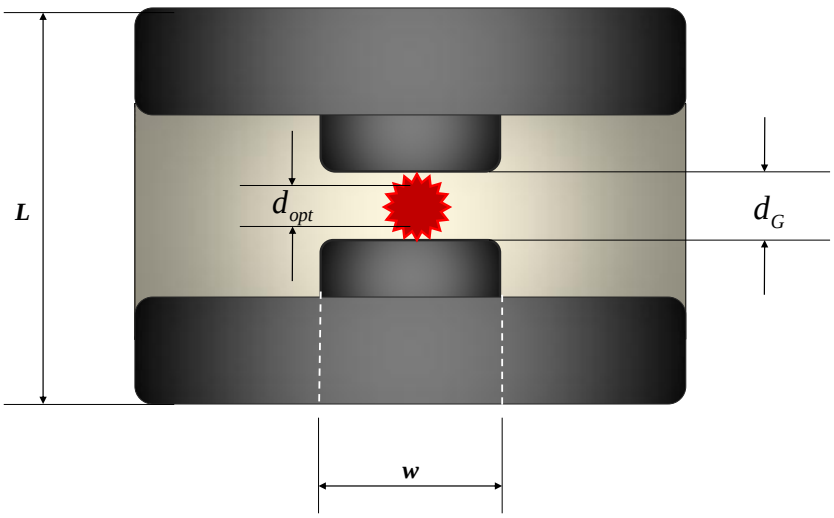

Figure 2.13: Schematic of the front view of a PCA dipole structure with the focused laser spot impinging into its gap.

Table 2.2: Materials and characteristics for PCAs

Photoconductive (PC) material	**Carrier lifetime** (ps)	**Mobility** $(cm^2V.s)$	**Resistivity** (Ω/cm)	**Band gap** $(eV$ at R.T.)
$Cr : SI - GaAs$	$50 - 100$	≈ 1000	10^7	1.43
$LT - GaAs$	0.25 aver.	$150 - 200$	10^6	1.43
$LT - In_{0.52}Al_{0.48}As$	0.4	5		1.45
$ErAs$	≈ 0.25	> 100	5×10^5	1.43
$SI - InP$	$50 - 100$	≈ 1000	4×10^7	1.34
Ion-implanted InP	2-4	200	$> 10^6$	1.34
Ion-implanted Ge	0.6	100		0.66
$RD - SoS$	0.6	30		1.10
Amorphous Si	$0.8 - 20$	1	10^7	1.10
MOCVD $CdTe$	0.5	180		1.49

2.4 Nonlinear Crystals

2.4.1 Optical Rectification in Non-linear Media

The development of broadband coherent sources and detectors of THz radiation constitute a key element in the progress of THz spectroscopic and imaging measurement capabilities. Actually, optical rectification arises as a result of the transient polarization which occurs when an ultrashort and high-intensity optical pulse interacts with the EO medium. The generated THz power is proportional to the square of the incident optical

power, and is determined by the second-order optical nonlinear coefficient ($\chi^{(2)}$), and varies with the relative orientation of the laser polarization and the crystallographic axes. Nowadays, lasers with pulse duration of $\sim 10\,\text{fs}$ are available, a fact that allows us to expand the bandwidth of coherent spectroscopy considerably. Optical rectification was one of the first techniques used to generate THz radiations and has the advantage over PCAs for the fact that its output saturates at much higher pump powers. DC optical rectification of 694 nm continuous wave (CW) laser in potassium dihydrogen phosphate (KDP) and potassium dideuterium phosphate (KD*P) was firstly demonstrated by Bass et al in 1962. Generation of a somehow broadband THz radiation (0.06 – 0.36 THz) was achieved by Yang et al. in 1971 by optical rectification of picoseconds Nd:glass laser pulses in litium niobate ($LiNbO_3$).

Recently Wu and Zhang, 1995 and Jepsen et al and Nahata et al., 1996, have demonstrated EO sampling of freely propagating THz pulses.

In optical rectification, crystals – as dielectric crystals ($LiNbO_3$,$LiTaO_3$, etc.), semiconductors (ZnTe, InP, GaAs, GaSe, etc.) and organic crystals (DAST, MA1:MMA, BNA, etc.) – rectify the oscillating electric field of an optical pulse to generate a quasi-DC polarization which follows the pulse envelope. The zinc-telluride (ZnTe), with high transparency in both optical and THz frequencies, and with large EO-coefficient ($r_{41} = d_{14} = 4\,\text{mp/V}$) is a widely used EO-crystal for THz generation and EO-sampling. Therefore, we will consider it in all examples throughout this section. It has no-inversion symmetry (non-centrosymmetric). In this crystal an efficient THz radiation generation may be obtained when the optical beam is polarized along the $[1\bar{1}0]$ crystallographic direction and propagates along the [110] axis. In this geometry the non-linear polarization is co-polarized with the optical beam.

Optical rectification is a process in which an optical pulse that is traveling through a non-linear crystal induces a time-dependent polarization change that leads to the radiation of an electromagnetic wave, whose polarization depends on the crystal orientation and on the incident pump polarization, and can be expressed as [37]

$$E_{THz}^{rad} \propto \frac{\partial^2 P(t)}{\partial t} \tag{2.24}$$

where $P(t)$ is the polarization.

Normally the frequency content of the radiated THz field has a strict relation with the pump beam bandwidth. So, an optical pulse with the duration $\tau = 10\,\text{fs}$ could led to a rectification of $\Delta\nu = 1/\tau = 100$ THz bandwidth. Since in experimental conditions there is an imperfect phase-matching between the group velocity of the incident optical pump and the phase velocity of the radiated THz field, limitation in bandwidth of the radiated THz field is expected. Now let us suppose that an electromagnetic field

propagates through a medium. It will tend to distort the atomic electronic structure of the medium, leading to the polarization of the medium. For example in an isotropic medium, like the zinc-telluride crystal (ZnTe), a scalar relationship of polarization (P), the electric susceptibility (χ), and the electric field (E) is used, and it is given as

$$P = \varepsilon_0 \chi E \tag{2.25}$$

where ε_0 is the permitivity of the free space.

This linear relationship is valid only for moderate fields, for higher fields, higher order terms are introduced and, as a result, the polarization takes the form of a power series expansion:

$$P_2^{nl} = \varepsilon_0(\chi^{(1)}E + \chi^{(2)}E^2 + \chi^{(3)}E^3 + \chi_4 E^3 + ...) \tag{2.26}$$

where χ^i is the i^{th}order susceptibility.

In this expansion, the term $\chi^{(2)}E^2$, represents the 2^{nd} order non-linear optical effect, which is associated to both optical rectification and the Pockells effect. Let us now assume that there is an incident optical wave with the form:

$$E = E_0 sin\omega t \tag{2.27}$$

then we will have

$$P^{(2)} = \varepsilon_0 \chi^{(1)} E \sin\omega t + \varepsilon_0 \chi^{(2)} E_0^2 \frac{1}{2}(1 - \cos 2\omega t) + ... \tag{2.28}$$

where, in this case, the 2^{nd} order non-linear polarization $P^{(2)}$, consists of a DC-polarization, $\varepsilon_0 \chi_2 E_0^2/2$ and a polarization with a $cos2\omega t$-dependence (which describes the SHG (second harmonic generation)). Therefore, the DC-polarization is a result of the incident optical electric field rectification by the 2^{nd} order non-linear χ of the medium. Now suppose there are two optical waves, $E_1 = E_0 \sin\omega_1 t$ and $E_2 = E_0 \sin\omega_2 t$. So, it yields:

$$P^{(2)} = \varepsilon_0 \chi_2 \frac{E_0^2}{2} \left[\cos\left(\omega_1 - \omega_2\right) t + \cos\left(\omega_1 + \omega_2\right) t\right] \tag{2.29}$$

It results in two terms: (a) $P^{(\omega_1 - \omega_2)}$, radiating at $\omega_1 - \omega_2$, which is responsible for THz-radiation generation, (b) $P^{(\omega_1 + \omega_2)}$, radiating at $\omega_1 + \omega_2$, which is not relevant for our purpose.

For efficient generation of THz radiation by optical rectification, we need single crystal with large EO coefficients, high second-order non-linearity, high quality structure, appropriate thickness and crystal orientation with respect to the linear polarization of the THz radiation. Additionally, the crystal surfaces must be optically flat at optical excitation wavelengths.

For greater interaction between the optical probe beam (OPB) and THz pulses in the crystal, and for the maximization of both the generation and sampling processes, longer interaction lengths are desirable. The phase matching is an imprescindible condition. It limits the interaction length in the crystal and restricts its usable length. Therefore, optical rectification process can be considered as a mixing of different spectral components of the optical pulse and THz frequency (ω_{opt} and $\omega_{opt} + \omega_{THz}$). For the wavevector k, the phase-matching condition is given by [40]

$$\Delta k = k(\omega_{opt} + \omega_{THz)}) - k(\omega_{opt}) - k(\omega_{THz}) = 0 \tag{2.30}$$

where k is the wave vector and ω_{opt} and ω_{THz} are the optical and the THz frequencies, respectively.

There is an ideal condition for THz radiation. If the refractive indices of the two frequencies are equal, $n_{opt} = n_{THz}$, meaning the two overlapped pulses propagate with the same velocity, the THz field would be constantly amplified as it propagates through the crystal. The refractive indices for the optical and the THz wavelengths for ZnTe are given as [46].

$$n^2_{Opt} = \frac{4.27 + 3.01\lambda^2}{\lambda^2 - 0.142} \tag{2.31}$$

$$n^2_{THz} = \frac{289.27 - 6\nu^2_{THz}}{29.16 - \nu^2_{THz}} \tag{2.32}$$

In real situations $n_{opt} \neq n_{THz}$ and, therefore, the velocity-matching condition is difficult to achieve. The efficiencies of non-linear THz generation and detection decrease with the increasing of the velocity mismatch. There is a tolerable velocity-mismatch distance called *coherence length* defined as the distance over which the optical pulse propagates before leading or lagging the THz wave by a phase shift of $\pi/2$. Neglecting the dispersion in the optical spectral range, the coherent length can be written as [47]:

$$l_c = \frac{c\pi}{\omega_{THz}\left|n_{opt(eff)}(\omega_0) - n_{THz}(\omega_{THz})\right|} \tag{2.33}$$

where c is the velocity of light, $n_{opt(eff)} = n_{opt}(\omega) - \lambda_{opt}(\partial n_{opt}/\partial\lambda)|_{\lambda_{opt}}$, $\omega_{THz} = 2\pi/\nu_{THz}$ is the THz frequency, ω_0 is the excitation laser frequency, n_{THz} is the refractive index at

THz frequency, n_{opt} is the refractive index at optical frequency and $n_{opt(eff)}$) is the group velocity refractive indices of the femtosecond optical pulse. The l_c for bandwidths up to 3 THz is $\sim$ 0.5mm and in the order of 50 μm for bandwidths larger than 3 THz [48].

The difference between the indices at optical and THz frequencies is normally small in all zinc blend crystals making possible the collinear velocity-matching.

There are some factors that affect the effectiveness of optical rectification such as: (a) the pulse duration of the laser, (b) the phase-matching conditions, and (c) the absorption of the EO crystal. The pulse duration of the laser is the main input for the crystal and determines the bandwidth of the THz pulse. Shorter pulses are needed in order the bandwidth be extended, and it is supposed that with the development of sub 10 femtosecond range laser, bandwidth of 100 THz could be generated. With such broadband pulses, it is impossible to select EO materials that fulfill the condition of group velocity matching for all frequency components. The thickness of the EO material must be small to obtain broad-bandwidth emission. The absorption in the EO crystal also affects the generation performance, so the thicker the crystal, the higher is the absorption, resulting in a lower output. Materials with a large second-order nonlinear coefficient are good candidates for the THz source [49]. Currently, ZnTe is the material of choice due to its high nonlinear coefficient, high damage threshold, and best phase-match condition with the Ti:sapphire laser. In contrast to PCAs the crystal must be pumped with a laser whose wavelength is longer than its bandgap $E_{ph} = hc/\lambda < E_g$ to get rid of absorption of the incoming radiation.

Zinc-blende semiconductors like ZnTe, Gap and GaSe are the widely used for THz generation by optical rectification since it generates very short and high-quality THz pulses. With higher electro-optic coefficients, the organic crystals, like 4-dimethylamino-N-methyl-4-stilbazolium tonsylate (DAST) [50] and, very recently, N-benzyl-2-methyl-4-nitroaniline (BNA) [51], have an enhanced capacity to generate stronger THz signals. However, the THz fields that they generate are very complex, in both time and frequency domains. They also, have a very large naturally occurring birefringence, which complicates their application and low-frequency phonon bands that limit the bandwidth in them. Because of this, the ZnTe crystal remains the widely preferred choice for the generation of THz radiation by optical rectification. Figure 2.14 shows the ZnTe crystal THz emission efficacy compared with other materials. It presents the relative performance of some emitters concerning the peak electric field amplitudes, the THz pulse energies and the energy conversion factors, as functions of the optical pulse energy [52].

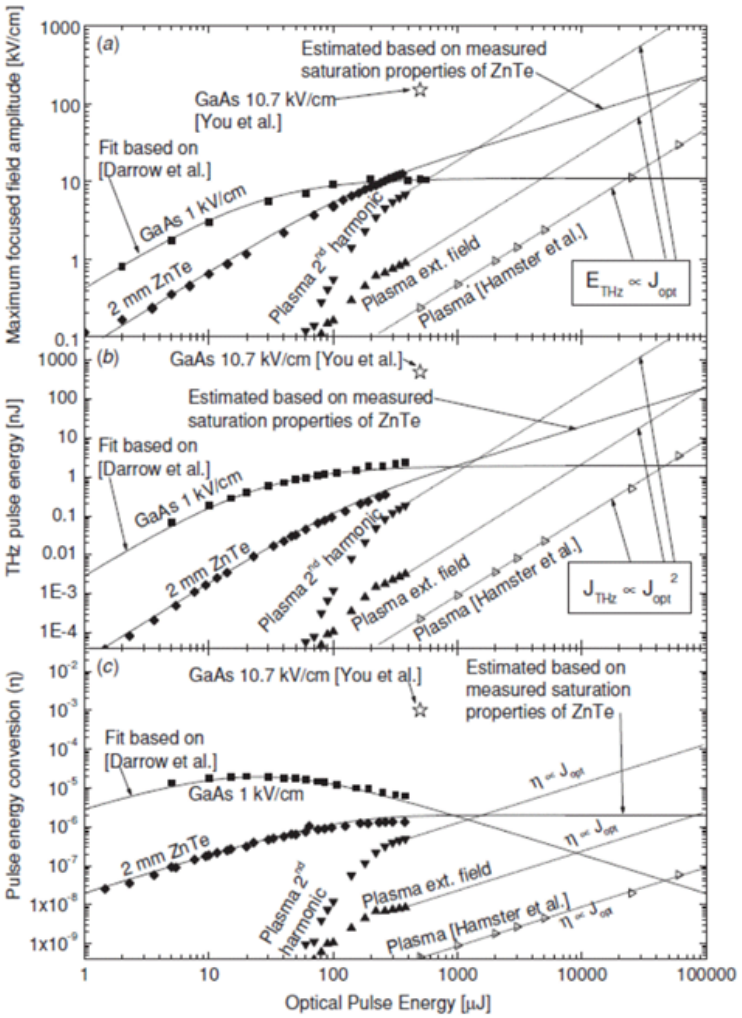

Figure 2.14: The THz emission efficacy of ZnTe compared with other THz emitters. Plots of the maximum focused field amplitude, the THz pulse energy and Pulse energy conversion are shown as function of the optical pulse energy [3].

2.4.2 Electro-Optic Sampling in Crystals

Like the already discussed PCA detectors, the EO sampling measures the electric field of THz pulses in time domain and determines accurately both the amplitude and the phase. The EO sampling can be considered as an inverse process of the optical rectification. In EO sampling, the THz field is measured by modulating an OPB inside the EO crystal, where it changes the polarization ellipsoid of the refractive index of the crystal. The linearly polarized OPB co-propagates inside the crystal with the THz beam, and its phase is modulated by the refractive index change induced by the electric field of the THz pulse. The existence of the THz field changes the birefringence of the EO crystal, causing the refractive index difference for polarizations along different axes

of the crystal. The birefringence induced by the electric field changes polarization of the probe beam. This polarization change is converted to intensity change by an analyzer (a Wollaston prism, for instance). A pair of balanced photodiodes is used to suppress the common laser noise while the signal is doubled. For ZnTe, when an electric field is applied, its ellipsoid of the refractive index is

$$\frac{x^2+y^2+z^2}{n_0^2} + 2r_{41}E_x yz + 2r_{41}E_y zx + 2r_{41}E_z xy = 1 \tag{2.34}$$

where where n_0 is refractive index of the crystal without electric field, x, y, z are coordinate units of the ellipsoid, r_{41} is EO coefficient of the crystal, and E_x, E_y, E_z are applied electric field along corresponding axes, respectively. Due to the Pockells' effect, the OPB experiences a phase-retardation $\Delta\phi$ in crossing the ZnTe EO crystal with thickness d which is given by [53]:

$$\Delta\phi = \frac{2\pi}{\lambda} d n_{opt}^3 r_{41} E_{THz} \tag{2.35}$$

The detection process is based on Pockells' effect existing in those crystals. Figure 2.15 presents a diagram illustrating a set-up for EO-sampling of THz pulses. Here, in the absence of THz field the optical probe beam (OPB) remains unaffected by the EO crystal and leaves it with horizontal polarization. It becomes circularly polarized after having passed through the $\lambda/4-$plate. The wollaston prism directs the two ortogonal components of the circularly polarized OPB to the two balanced photodiodes (BPD) with the same intensity, and the differential signal is zero. However, in the presence of THz field, the birefringence induced by the THz field in the EO crystal causes polarization change on the linearly polarized OPB. It becomes elliptically polarized. Then, the Wollaston prism (WP) splits the OPB into two orthogonal polarization components ($y-$ and $z-$components), which are directed to a balanced photodiodes differential detector (BPD-DD) connected to the differential of a Lock-in amplifier, where the intensity difference, $\Delta I = I_x - I_y$, of the two OPB components is measured. The obtained value is proportional to the applied THz field amplitude.

The two intensities which are directed to de BPD-DD by the WP are given by:

$$\begin{aligned} I_x &\approx \frac{I_0}{2}(1-\sin\Delta\phi) \approx \frac{I_0}{2}(1-\Delta\phi) \\ I_y &\approx \frac{I_0}{2}(1+\sin\Delta\phi) \approx \frac{I_0}{2}(1+\Delta\phi) \end{aligned} \tag{2.36}$$

where I_0 is the intensity of the incoming OPB and $\Delta\phi$ is considered to small ($\Delta\phi \ll 1$) a valid approximation for the majority of EO-samplings.

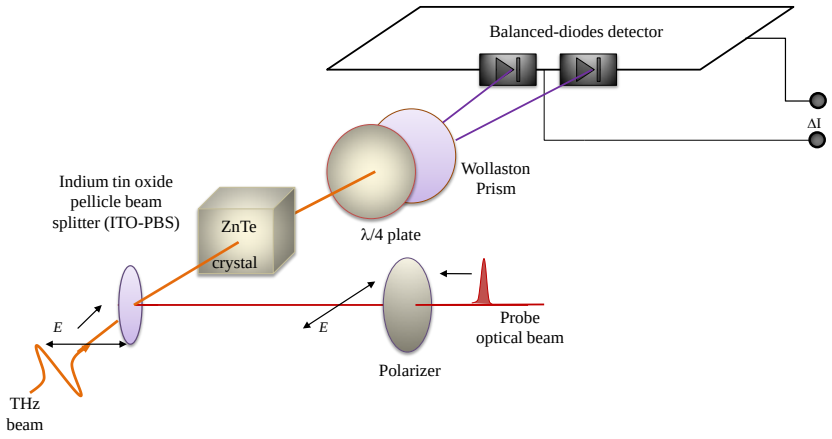

Figure 2.15: Experimental setup for detection of THz pulses in an EO crystal. The THz electric field induces a birefringence in the ZnTe crystal. An indium-tin oxide beam-splitter (ITO-BS) directs the THz and probe beam collinearly through the EO detector. Then a Wollaston prism (WP) directs the beams with two orthogonal polarizations to a balanced photodiodes differential detector (BPD-DD).

Figure 2.16 shows the geometry for optical and THz polarizations in the case of EO sampling using a ZnTe crystal. Both THz and optical beams are collinear at the entrance of the EO-crystal and the birefringence induced by the field is maximal when the two polarizations (THz and optical) are parallel to the $[1\bar{1}0]$axis of the $\langle 110\rangle$ – oriented ZnTe crystal.

From equations (**??**) and (2.36) the current of the balanced photodiodes' differential detector I_{BPD} is:

$$I_{BPD} = I_y - I_x = I_0\Delta\phi = \frac{2\pi d I_0}{\lambda} n_0^3 r_{41} E_{THz} \propto E_{THz} \tag{2.37}$$

In practical experiments, there are three factors limiting the spectral/temporal resolution of EO-sampling: (a) the finite pulse duration (τ_s) of the OPB, (b) the dispersion of the non-linear susceptibility and (c) the mismatch between the optical group velocity $v_{g(opt)}$ and the THz phase velocity $v_{ph(THz)}$. These factors are included in the detector's response function $F(\omega, \omega_{THz})$. The time-resolved EO signal can be described as the inverse Fourier transform of the product of the THz pulse complex spectral amplitude $E_{THz}(\omega_{THz})$ and $F(\omega, \omega_{THz})$:

$$E_{EOS}(t) = \int_{-\infty}^{\infty} E_{THz}(\omega_{THz}) F(\omega, \omega_{THz}) e^{-i\omega_{THz}t} d\omega_{THz} \tag{2.38}$$

This integral is equivalent to a convolution in time domain [54].

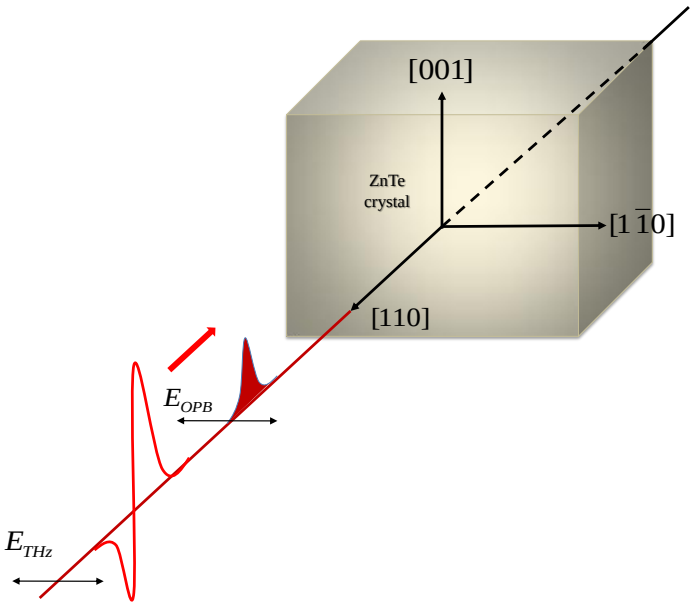

Figure 2.16: The geometry of the polarization and the crystal orientation for the THz pulse detection with ZnTe crystal. Both optical and THz fields enter the crystal collinearly and with horizontal linear polarization.

Table 2.3: Electro-Optic coefficients of some commonly used THz emitters and detectors

Material	Structure	Point Group Symetry	Electro-Optic Coefficient (pm/V)
ZnTe	Zincblende	$\bar{4}3m$	$r_{41} = 3.9$
GaP	Zincblende	$\bar{4}3m$	$r_{41} = 0.97$
GaSe	Hexagonal	$\bar{6}2m$	$r_{41} = 14.4$

Table 2.3 presents the linear electro-optic coefficients of some commonly used crystals for non-linear optical generation and detection of THz radiation. The three crystals are unaxial, therefore, crystals with one axis of rotational symetry only (the optical axis of the crystal or c-axis). Table 2.4 presents material used for THz generation by optical rectification [40] and Table 2.5 presentes a comparison of two THz generation techniques , by PCA and optical rectification in nonlinear crystals in terms of generation efficiency, bandwidth and spectral quality.

2.4.3 The Terahertz Optics

The manipulation of THz radiation (reflection, collimation and focusing) is performed using THz optical components. For an efficient THz-TDS system, the optics must produce diffraction-limited focal point at the sample with the minimum absorption.

Table 2.4: Materials used for THz generation by optical rectification

Semiconductors	**Inorganic Electro-Optic Crystals**	**Organic Electro-Optic Crystal**
GaAs	$LiNbO_3$	4-N-methylstilbazolium (DAST)
InP	$LiTaO_3$	N-benzyl-2-methyl-4-nitroaniline (BNA)
CdTe		(-)-2-(α-methylbenzyl-amino-5-nitropiridine (MBANP)
InAs		Electro-Optic Polymers
InSb		
GaP		
ZnTe		
ZnCdTe		
GaSe		

Table 2.5: THz Generation: Comparison between PCA and Optical Rectification

	Efficiency	**Bandwidth**	**Spectral quality**
Photoconductive Aantennas	Although high it is limited to low intensities	Restricted by carriers' recombination time and material absorption, typically $\sim 3\,\mathrm{THz}$	Good
Optical Rectification	Is dependent on pump intensity	Broad ($\sim 100\,\mathrm{THz}$) and strongly dependent on phase-matching and material absorption	Strongly dependent on bandwidth

In order to process equally the large spectral bandwidth of THz emitters, the optical system must be achromatic with flat response over the frequency range of the pulses.

Substrate Lens

In PCAs, substrate lenses are usually used in order to improve the coupling efficiency of the THz radiation into the free space. The Laboratory's THz-setup at the Vilnius Institute of Semiconductor Physics (ISP), where the experiments have been held, a high-resistivity (>10kΩ-cm) hyperhemispherical substrate silicon (Si) lens is used. Attached onto the GaAs substrate, it minimizes the reflections at the substrate-lens interface because the refractive index of the silicon closely matches that of GaAs substrate at THz frequencies. Alternatively to the hyperhemispherical lens a so called collimating lens is also used, although with some disadvantages, as we will see later. The role of the Si lenses is to decrease the cone radiation of the antenna with the minimum losses. All the rays coming out of the antenna, covering the half space in the forward direction, should be concentrated in a smaller cone with minimum losses at the interface lens-air. Figure (2.17) (a) shows the substrate and the lens with the indication of antenna emission angle ϕ and the internal-incidence angle θ at the interface lens-air. By geometrical considerations, the following relation can be written [55]:

$$(d - R)\, sin\theta = R sin\theta \tag{2.39}$$

where R is the radius of the lens and d is the distance of the point-like emitter to the vertice of the spherical lens.

In the hyperhemispherical lens, the emitter is positioned such that no rays are trapped by the internal reflections, while, in the collimating lens, the emitter is located at focus of the lens.

To avoid total internal reflections of the THz radiation in the interface lens-air, the angle θ must be equal to the critical angle θ_c when $\phi = \pi/2$. Using equation (2.39) and the definition of critical angle,$sin\theta_c = 1/n$, we get the following relationship:

$$(d - R)\sin\pi/2 = R\sin\theta_c \tag{2.40}$$

therefore

$$d - R = R(1/n) \tag{2.41}$$

The hyper-hemispherical lens is mounted in order to avoid total internal reflections and, therefore, the emitter-to-lens-tip distance must be

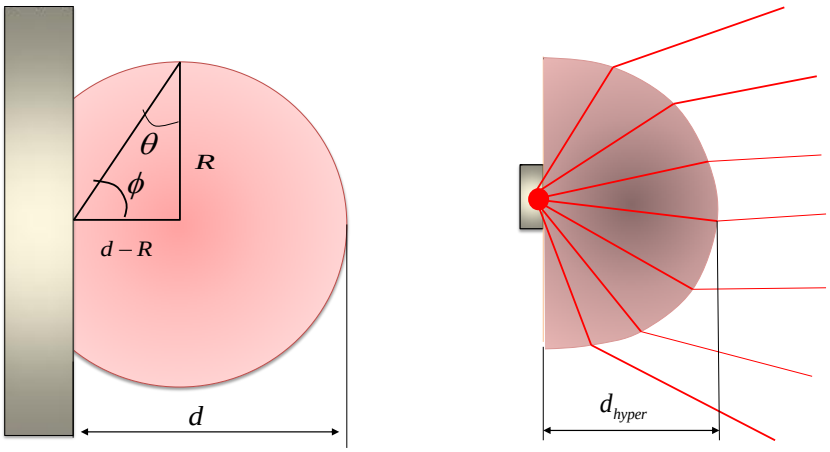

Figure 2.17: (a) Geometry of the lens over the PCA substrate, showing the antenna emission angle ϕ and the internal-incidence angle θ at the interface lens-air; R is the radius of the lens, d is the distance from the point-like antenna to the tip of the lens; (b) geometry of the hyper-hemispherical lens showing the distance d_{hyper}dhyper corresponding to the condition of absence of total internal reflection at the interface lens-air.

$$d_{hyper} = R\left(\frac{n+1}{n}\right) \tag{2.42}$$

where $n = 1.418$ is the refractive index of the silicon, and $d_{hyper} = 1.29R$. It is important to remember that reflections at the substrate-lens interface are minimized because of closely matched refractive indices (n_{Si} and n_{GaAs}).

To evaluate the divergence of the THz beam coming out of the hyper-hemispherical lens we must calculate the image of the antenna point source. Applying the imaging formula of a single spherical refractive surface, in the paraxial approximation, the position of the source image is found at the left side of the lens at a distance from the lens tip equal to L, where L is given by:

$$L = R\,(n+1) \tag{2.43}$$

For silicon $L = 4.4R$.

With a hyper-hemispherical lens, all the forward directed THz-rays can escape the substrate. The persisting problem is the beam divergence, which requires a further focusing element such a lens or a mirror. This type of lenses is advantageous over the other substrate lens design such as collimating hemispherical lens.

In the geometry of collimating hemispherical lens the emitter is at the focus of the substrate lens and the rays emerge from the lens almost collimated. Applying the

imaging formula of a single spherical refractive surface, in the paraxial approximation, we get for the focal length

$$f = d_{coll} = R\left(\frac{n}{n-1}\right) \tag{2.44}$$

where d_{coll} is the distance from the emitter to the tip of the lens including the substrate thickness (t), which implies that the effective thickness of the hemisphere is

$$h_{eff} = d_{coll} - t \tag{2.45}$$

For silicon $d_{coll} = 1.41$.

Off-Axis Parabolic Mirrors

The off-axis parabolic mirrors (OAPMs) are used to collimate, steer and focus the THz beam after it leaves the lens' hemisphere of the substrate lens. They have the shapes of paraboloid sections, as shown in Figure 2.18. For an efficient collection of radiation without significant losses a good choice of F-number or nominal focal ratio

($F\# = f/d$ where f is focal length and d is the entrance pupil diameter), of the mirror is needed.

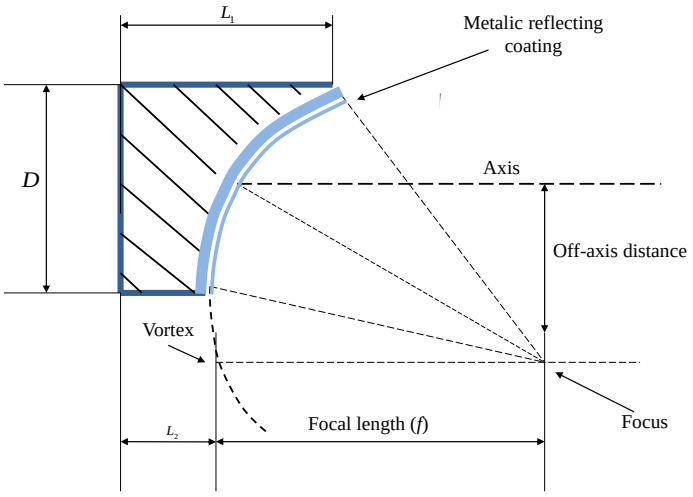

Figure 2.18: Sketch of an off-axis parabolic mirror.

The shape of the surface is calculated by the following expression

Table 2.6: Reflectivity of the usually used metals for coating OAPMs' reflective surfaces

Metal	Reflectivity	
	0.58 THz	**2.55 THz**
Silver (Ag)	0.996	0.995
Aluminium (Al)	0.995	0.994
Gold (Au)	0.994	0.994

$$Z = R^2/4f \tag{2.46}$$

where R is the radial distance from the vortex and f is the focal distance.

Their reflective surfaces are usually coated with metals whose reflectivity in the THz frequency region is close to 99% (Table 2.6).

Compared with lenses and bulk materials, which have inherent Fresnel losses and no negligible absorption, the metallic surfaces have minimal losses. The off-axis geometry is somehow difficult for beam alignment, because of its high sensitivity to astigmatism and other collimation errors, so that high-precision alignment procedures are needed, in practical applications, to get rid of them. The OAPMs work over a broad spectral range without spectral aberration.

Since quasi-optical THz systems deal with diffraction-limited beams, the fact that the OAPMs are free from spherical aberration, and that they can focus parallel beams to a point, is of crucial importance for practical experimental applications. Diffraction and limited reflections of the THz beam at the mirrors contribute to the reduction in the THz power. To get rid of this problem, the number of mirrors must be reduced, and the distance emitter-detector also has to be reduced to quasi-near field. In an experimental set-up, if two OAPMs are placed in a way that the axes of the parent parabolas coincide, the astigmatism is cancelled but, distortion is introduced. If the axes of the two OAPMs are 180^0 rotated relatively to their common optical axis, astigmatism of the two mirrors takes the maximum value. So, there is one ideal arrangement of the OAPMs', where the two OAPMs are placed such that their parent parabolas are with coincident axis as depicted in the Figure 2.19.

Scanning Optical Delay Stage

It is known that in a TDTS system a femtosecond laser beam is split into two, the pumping beam and the OPB. The two optical paths to the detector must be equal in the set-up calibration. TDTS system requires a scanning optical delay line to introduce a delay between the THz and the optical probe beams, in order to move the sampling

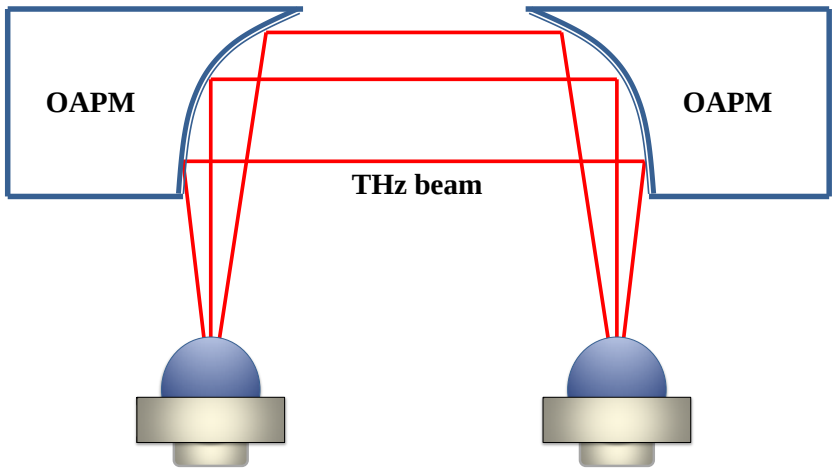

Figure 2.19: Two OAPMs with coincident axes of the parent parabolas.

gate across the THz signal to be sampled. Figure 2.20 shows a diagram illustrating the sampling of a THz pulse by a femtosecond optical pulse. A retro-reflective mirror system (Figure 2.21) was used in this work. It was mounted on a mechanical scanner normally used for this kind of application.

The scanning system has the maximum speed of $\sim 50.8\,\mathrm{mm}.s^{-1}$, a resolution of about 0.125μmand a repeatability of 5μm. The resolution of the THz spectrometer depends upon the step size of the delay line movement. For imaging application, a scan as fast as possible is required in order to increase the signal acquisition rate.

Nowadays typical point-by-point THz imaging process has a data acquisition rate of $20\,\mathrm{pi}.s^{-1}$ (pixels per second) corresponding to a scanning time of a few minutes per image. The length of the time-delay line determines the frequency resolution.

Lock-in Amplifier

Lock-in amplifiers (LIA) are used to detect and measure very small AC signals. The signal to be measured is compared to a reference signal for both its frequency and relative phase difference. The reference signal is provided by an optical chopper, which interrupts the optical beam periodically. The reference signal and the signal to be measured are combined to generate a difference and a sum frequency. Therefore, the OPB is periodically interrupted by a chopper. The frequency of the modulation provides the reference frequency, and the signals to be measured from the detector must have the same frequency, $\nu_s = \nu_{ref}$.

The input signals at the LIA's mixer are:

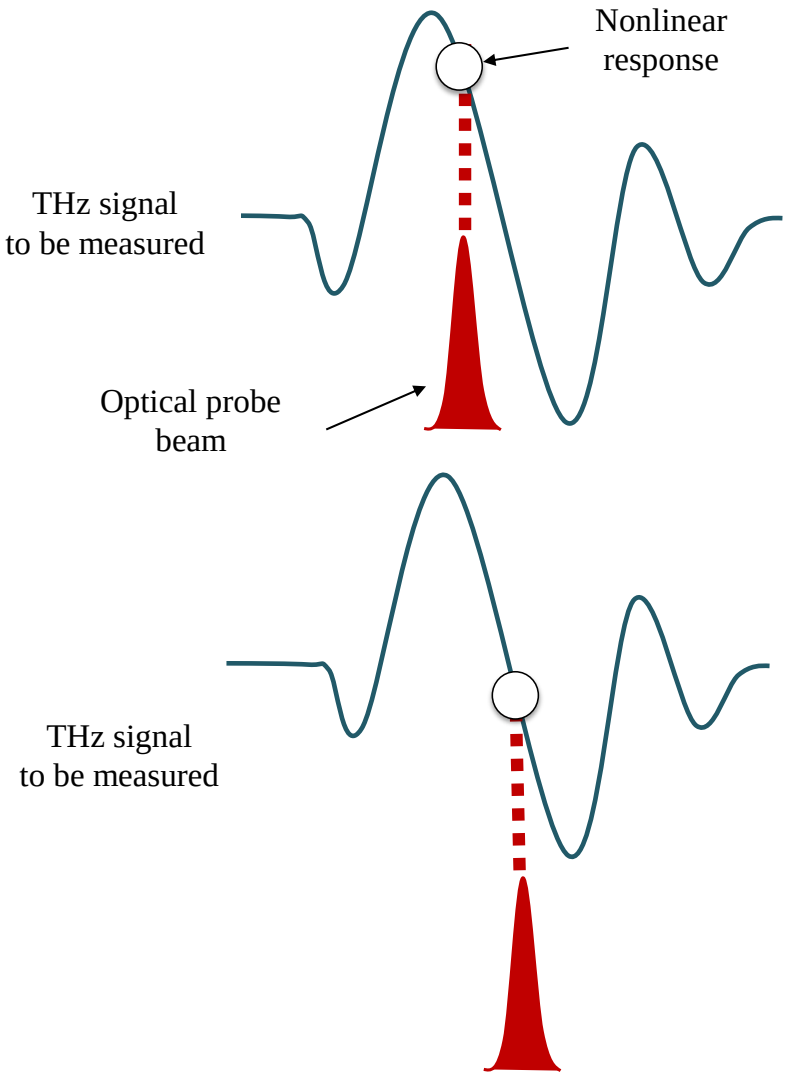

Figure 2.20: THz pulse sampling process. The THz signal is sampled by delaying the optical pulse.

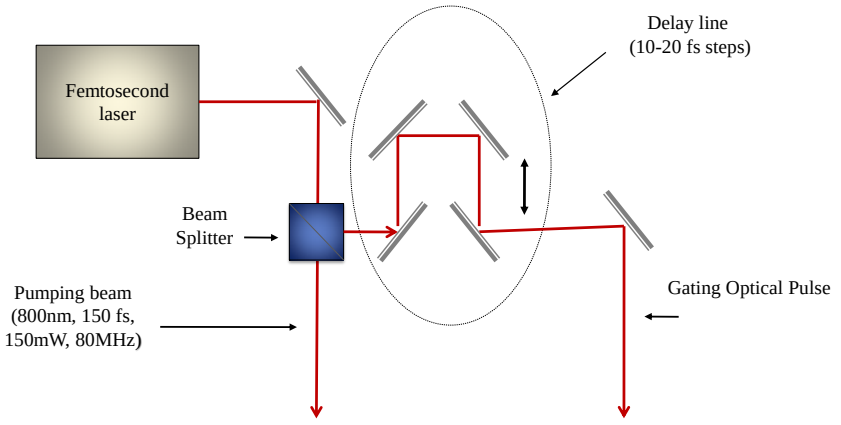

Figure 2.21: Partial block diagram of a THz spectrometer highlighting (the circled section with green dashed line) the optical delay line

$$A cos\left(\nu_s t + \phi\right) \text{ and } B cos\left(\nu_{ref} t\right) \tag{2.47}$$

and the output signals are

$$AB cos\left(\nu_s t + \phi\right) cos\left(\nu_{ref} t\right) = AB/2 cos\left[\left(\nu_s + \nu_{ref}\right) t + \phi\right] + AB/2 cos\left[\left(\nu_s - \nu_{ref}\right) t + \phi\right] \tag{2.48}$$

Accurate measurements may be made even when the signal is small and masked by background noises thousands of times larger. It is based on the technique known as *phase-sensitive detection* that singles out the component of the signal at the reference frequency and phase. Therefore, noise signals at a frequency other than the reference are rejected and do not affect the measurement (i.e., The phase difference between reference and signal can be adjusted to zero, and the low pass filter eliminates the sum frequency term and the resulting signal is DC). In this work a LIA was used to collect the data from the THz detector. The LIA time constant $\tau_{LIA} = 1/2\pi\nu_{\text{fil}}$where ν_{fil} is the -3dB frequency of the LIA's single filter only, and the optical delay time speed (off/on) must be carefully chosen in order the TDTS system accurately couple the entire pulse, maximizing the SNR and minimizing the total scan time. The data collection rate and the optical delay line have to be synchronized to control the bandwidth (B) and frequency resolution ($\Delta\nu$) of the system. The bandwidth is given by

$$B = \frac{1}{2\Delta t} \tag{2.49}$$

where Δt is the time step between data points collected along the THz pulse, and the frequency resolution $\Delta\nu$ is given by

$$\Delta\nu = \frac{1}{2\Delta t N} = \frac{1}{2T} \tag{2.50}$$

where N is the total number of data points and T the total time of the scanned pulse.

2.4.4 Summary

In this chapter, the two most commonly used techniques (PCAs and optical rectification) and the physical principles of generation and detection of THz pulses have been broadly discussed. The mechanisms of photocarriers' generation and the consequent THz pulse generation, as well as a brief description of the method of detection by TL-GaAs PCA used in this work are revised. A commonly used technique for the generation and detection of THz pulses that has not been used in this work was also

discussed. Attention has been paid to the differences of both THz generation and detection techniques such as biased semiconductor pump versus nonlinear crystal pump (in generation); the gated PCA detection versus EO sampling; the need of a current pre-amplification in PCA versus the straight connection to the LIA in EO sampling (in detection). Finally, in the last section, the important part od THz beam manipulation in experimental geometries is thoroughly described.

Chapter 3

Time-domain Terahertz Spectroscopy

3.1 Introduction

In time-domain THz spectroscopy (TDTS), a sub-picoseconds THz pulse (called the signal) is transmitted through or reflected by a sample and its time-domain profile is compared to a reference pulse without the sample (called the reference). The THz electric field is directly measured as a function of time and the frequency spectra of both signal and reference are obtained by numerical Fourier transformation. The analysis of the spectra yields the spectroscopic information of the sample material under study. Since the measurements are made on electric field instead of intensity, both amplitude and phase are determined, making possible, at once, the extraction of the sample frequency-dependent optical constants such as the absorption coefficient and the refractive index along the pulse's frequency envelop. This is an advantage compared to the well-established Fourier transform spectroscopy (FTS) which is based on the power detection with recourse to Kramers-Kronig data analysis, with all the uncertainties associated with it.

A TDTS is a pump-probe-like technique since the signal and reference are measured by sampling using a delayed probe optical pulse, taking the form of a time trace with subpicosecond resolution. Due to the coherent gated detection used in TDTS (the detector is kept off ofduring the time between two *detection events* avoiding the thermal background radiation noise), it is possible to operate at room temperature. The signal-to-noise ratio (SNR) is much higher than that of FTS. The Coherent-gated detection gives a noise equivalent power of $\sim 10^{-16} W/\sqrt{Hz}$, which is six orders of magnitude better than the pyro-detectors, normally used in Fourier transform spectrometers.

Since THz pulses used in TDTS have very low peak powers in comparison with optical pulses, nonlinearities are normally neglected, so that the treatment of the THz propagation is made on the bases of linear dispersion theory. Care must be taken with

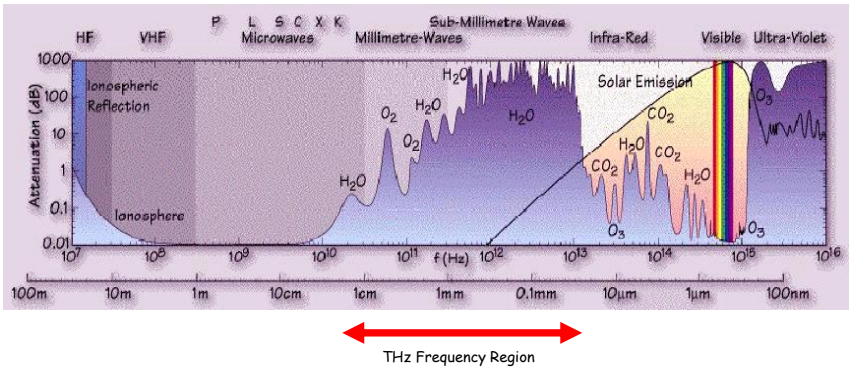

Figure 3.1: Atmospheric absorption spectrum. The THz radiation is heavily absorbed by the atmosphere, specially by water vapor contained in it [4].

the strong absorption of atmosphere water vapor (Figure3.1) along the beam path. In some experiments, the set-up is enclosed in a box filled with dry nitrogen (N2).

3.2 Time-Domain Terahertz Spectroscopy in Reflection geometry: Data Analysis

The optical parameters of a sample may be evaluated using reflection or transmission. The refractive index n and the absorption coefficient α of a strongly absorbing material, such as biological tissues, cannot be measured in a transmission experiment if the amplitude of the transmitted terahertz signal is not much larger than the detection limit. However, a reflection geometry (Figure 3.2) can be used to overcome this limitation.

The absorption coefficient and the refractive index are extracted using the following expression [[56].

$$\frac{E_s(\omega)}{E_{ref}} = \frac{t_{a,p}r_{p,s}}{t_{p,a}}(\omega)exp\left[i\frac{4\pi n_p l\nu}{c}\right] \tag{3.1}$$

where$E_s(\omega)$ is the measured electric field of the pulse reflected at the interface polyethylene-sample; E_{ref} is the measured electric field of the pulse at the front surface (air-polyethylene) of the sample holder polyethylene; $r_{p,s}$ is the complex reflection coefficient for the polyethylene/silicon-sample interface to be calculated, $t_{a,p}$ and $t_{p,a}$, are the known transmission coefficients for air-polyethylene and polyethylene-air interfaces. Since the absorptions of the air and polyethylene are negligible, the above transmission coefficients are assumed to be real; the n_p is the known refractive index of the medium

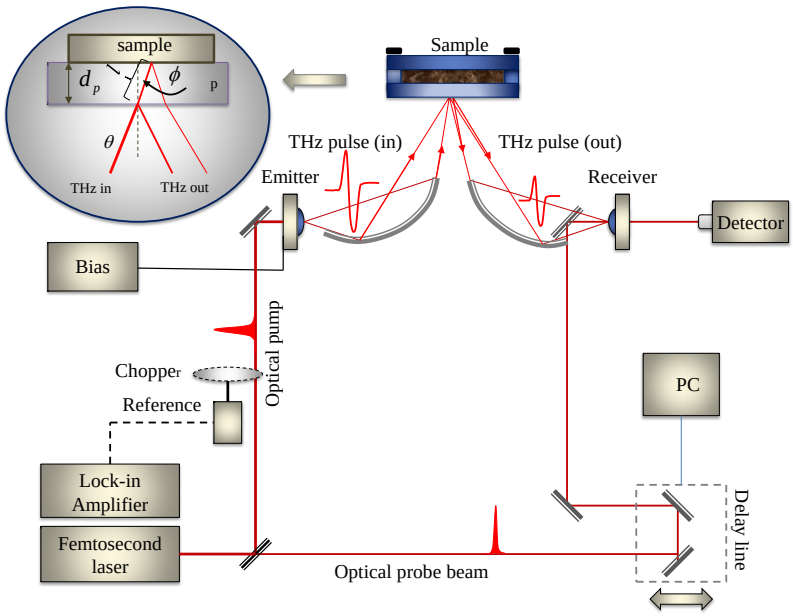

Figure 3.2: Diagram for TDTS reflection geometry. The biological tissue is sandwiched by two sheets/windows of a high density polyethylene with a thickness of <2mm. The reflections from the front and the backside of the window are the reference and the sample signal, respectively.

used as reference (polyethylene), and l is the effective thickness of the polyethylene sheet which can be calculated from:

$$l = d_p/cos\phi \tag{3.2}$$

where d_p is the thickness of the sample holder window and, ϕ is the reflection angle on the back side of the window (in contact with the sample). The known and measured quantities in equation (3.1) allow the determination of $r_{p,s}$, that can be written in its complex form:

$$r_{p,s}(\omega) = A\exp(i\theta) \tag{3.3}$$

where A is the amplitude and θ the phase.

Lets now consider the case of normal incidence, where the reflection and transmission coefficients have simpler forms. Then, the complex reflection coefficient becomes:

$$r_{p,s}(\omega) = \frac{n_p - \tilde{n}(\omega)}{n_p + \tilde{n}(\omega)} \tag{3.4}$$

where $\widetilde{n}(\omega) = n_s(\omega) + i\alpha_s(\omega)c/4\pi\nu$ is the complex refractive index of the sample; $n_s(\omega)$

is the real part of $\widetilde{n}(\omega)$; $\alpha_s(\omega)$ is the absorption coefficient; c, the velocity of light in vacuum, and ν, the frequency of THz radiation.

Substituting equation 3.3 in equation 3.4, we obtain to the sample index of refraction

$$n_s(\omega) = \frac{n_p\,(1 - A^2)}{1 + A^2 + 2A\cos\theta} \tag{3.5}$$

and to the absorption coefficient:

$$\alpha_s(\omega) = \frac{4\pi n_s v}{c}\frac{-2A\sin\theta}{1 + A^2 + 2A\cos\theta} \tag{3.6}$$

In the reflection configuration the extraction of these frequency-dependent parameters is a bit more complicated than in transmission configuration, as we will see later. Similarly to the transmission, both reference and sample signals are recorded. However, apart from a temporal shift of the sample and the reference pulse due to the reference polyethylene window, an additional spatial shift occurs due to refraction and the absorption data are contained within the phase information of the measurement, which is sensitive to system artifacts. Additionally there is one more difficulty, arising as a result of a polarization change due to reflection under a specific angle that causes the reference and sample pulses to be differently polarized. This is relevant, since the sensitivity of the detector is polarization-dependent.

3.3 Time-Domain Terahertz Spectroscopy in Transmission Geometry

In this thesis work, the experimental measurements have been made by using TDTS in transmission geometry as shown in Figure 3.3. A laser beam (800nm, 150fs, 200mW and 80MHz) was split into a pump and a probe beam using a 70% beam splitter (BS). The pump beam, with approximately 20mW is focused ($\sim 25\mu$m of beam spot size) between the electrodes of a photoconductive GaAs emitter antenna (PCA). A hemispherical high resistivity silicon lens is stuck onto the GaAs substrate; it has a high refractive index ($n = 3.43$), and it favors the emitter efficiency by minimizing the reflection losses and collimating the highly divergent THz beam.

As the THz signal is extremely weak – in the order of $> 10\,\mu$W – a current amplifier is needed. A lock-in amplifier (LIA, SR-810 Stanford Research Systems) synchronized with a chopper (optical mudulator) was also used to extract the signal from the thermal background and to enhance the SNR. Due to the coherent and gated detection nature of the TDTS technique, it was possible to measure the signals, masked by the thermal

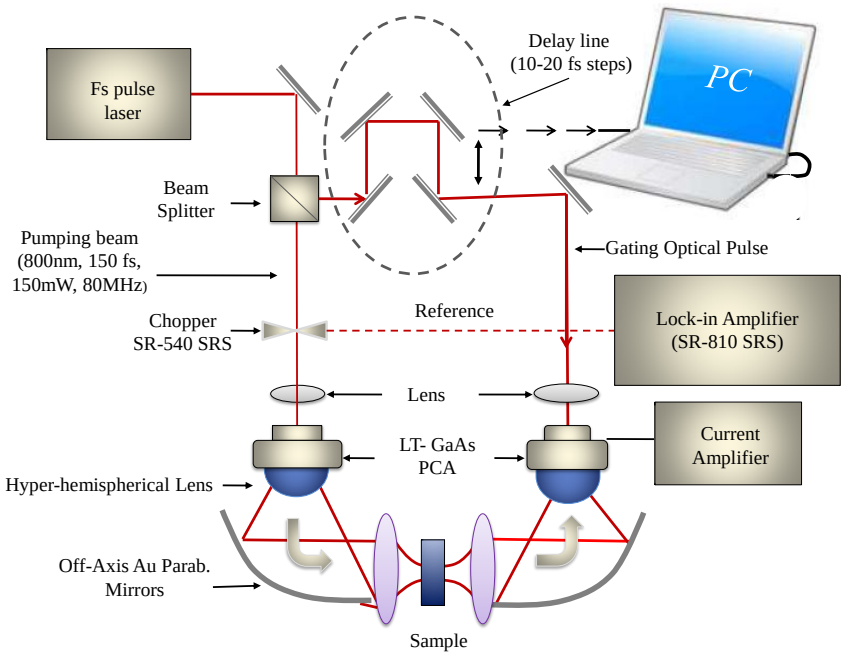

Figure 3.3: Experimental setup for transmission time-domain THz spectroscopy (TTDS) measurements using photoconductive antennas (PCAs) for generation and detection of THz pulses.

background noise. A computer controled delay-line, reads the LIA values at each position and records the THz pulse waveforms.

Figure 3.4 shows a diagram of a system for data acquisition (DAQ). The signal is firstly enhanced by a low-noise current amplifier (in case the THz detection is by a PCA) and then sent to the LIA which detects the signal at reference frequency. But, if the detection is by EO sampling the photodiodes are directly connected to a differential input of the LIA. A delay stage with dc-motor actuator, driven by a motion controller, moves a set of mirrors either continuously or stepwise with adjustable waiting time between steps. The mechanical precision of the movement is $\sim 0.1\,\mu$m corresponding to time shift of ~ 0.66 fs. In TDT spectrometer three parameters are of interest: the delay stage waiting time (t_{delay}); the LIA's time constant, the integration time (t_{LIA}); and the frequency of the chopper ($\nu_{chopper}$). For a higher SNR and narrower amplifier bandwidth noise, longer t_{LIA} is needed.

3.4 Time-Domain Terahertz Spectroscopy in Transmission geometry: Data Analysis

For TDTS measurements the following assumptions are considered: (a) the sample under measurement is a homogeneous dielectric slab with parallel and flat surfaces,

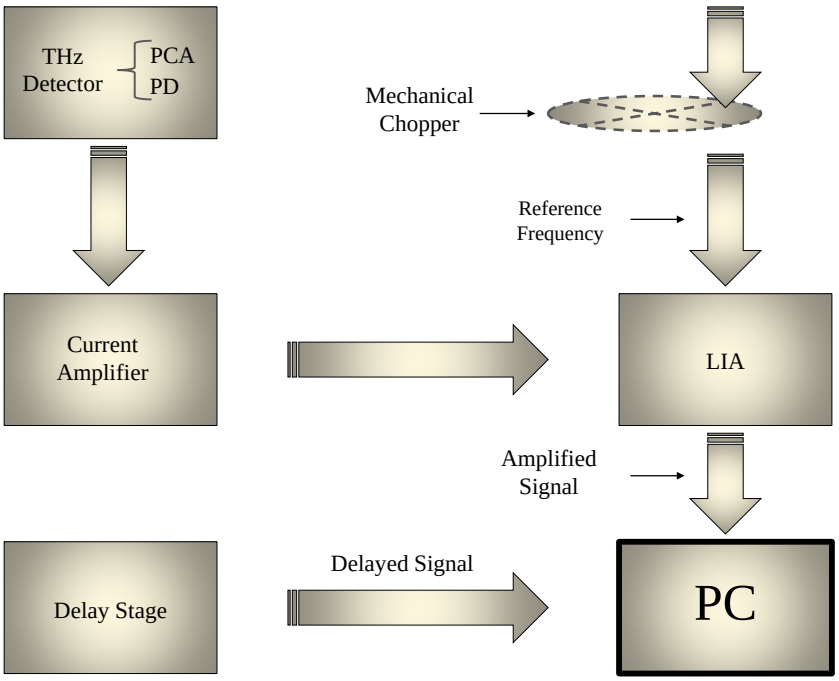

Figure 3.4: Data acquisition system (DAQ) diagram for PCA detection. If the detection is based on photodiodes (EOS), the current amplifier is eliminated and the photodiodes are connected directly to the differential input of the LIA.

where the scattering of THz rays is negligible; (b) the incident angle of the THz beam is normal to the sample surfaces; (c) the transverse dimension of the sample is larger than the incident beam waist, so there is no diffraction; (d) the reference signal is measured under the same conditions as the sample signal; (e) the resolution of the measuring apparatus is sufficiently high so that the quantization error is negligible, unless stated otherwise; (f) the measuring instruments are well-calibrated and (g) there is no human error in the measurements.

The determination of frequency-dependent optical constants of a sample using TDTS comprehends several steps, as illustrated in Figure 3.5 and Figure 3.6.

Since the quantity provided by a TDTS measurement is a time-domain signal, then a physical model is required to relate the measured signal to the optical properties of the sample. Normally the waveforms of the THz pulses have very narrow time-widths (~ 0.25ps).

As already stated, two pulses are recorded in TDTS: one with an empty sample holder; the other with the sample in the holder. In TDTS measurements, the measured signal is proportional to the electric field of the THz pulse $E_{THz}(t)$.

The pulse that propagates through the sample is called sample pulse $E_s(t)$; the pulse that propagates through the reference medium (with known dielectric constants) is called reference pulse $E_{ref}(t)$. Knowing the time evolution of those pulses, it is possible

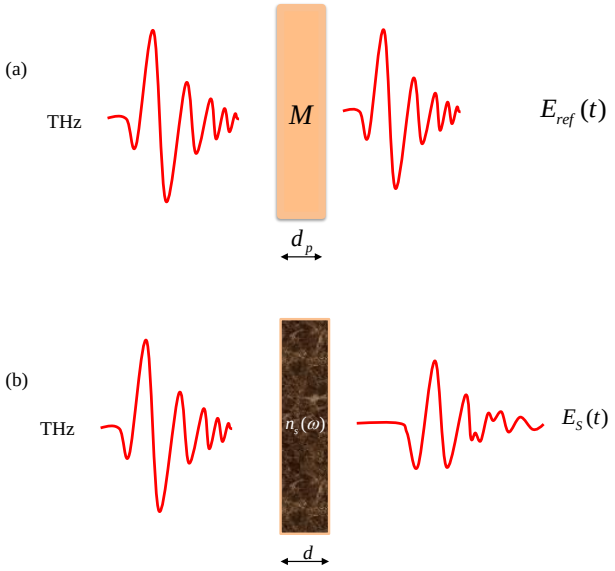

Figure 3.5: A diagram illustrating the experimental basics of TDTS. The THz pulse propagates through (a) a reference medium (M) and (b) the samples andwiched between two windows (not indicated in the figure) of reference medium.

to get the information about the frequency-dependent dielectric constants (absorption coefficient and the refractive index) of the sample. Figure 3.5 presents a diagram representation of a TDTS in transmission geometry. It can be noticed that the THz signal propagates through the reference medium and through the sample as well, over a distance d, the thickness of the sample. Lets now represent with M (assumed to be constant) the value of the refractive index of the reference medium, which is transparent at THz frequencies, i.e., quasi no-absorbing medium ($\alpha \approx 0$). The Fresnel amplitude transmission coefficients through the interfaces, reference medium – sample and, sample – reference medium for normal incidence are:

$$t_{M,s} = \frac{2M}{M + \tilde{n}(\omega)} \tag{3.7}$$

$$t_{s,M} = \frac{2\tilde{n}(\omega)}{M + \tilde{n}(\omega)} \tag{3.8}$$

where, $\widetilde{n}(\omega) = n_s(\omega) - i\kappa(\omega)$ is the complex refractive index of the sample. The real part of this expression denotes the real refractive index of the sample and the imaginary one is related with the absorption coefficient.

Taking the Fourier transform of $E(t)$ as:

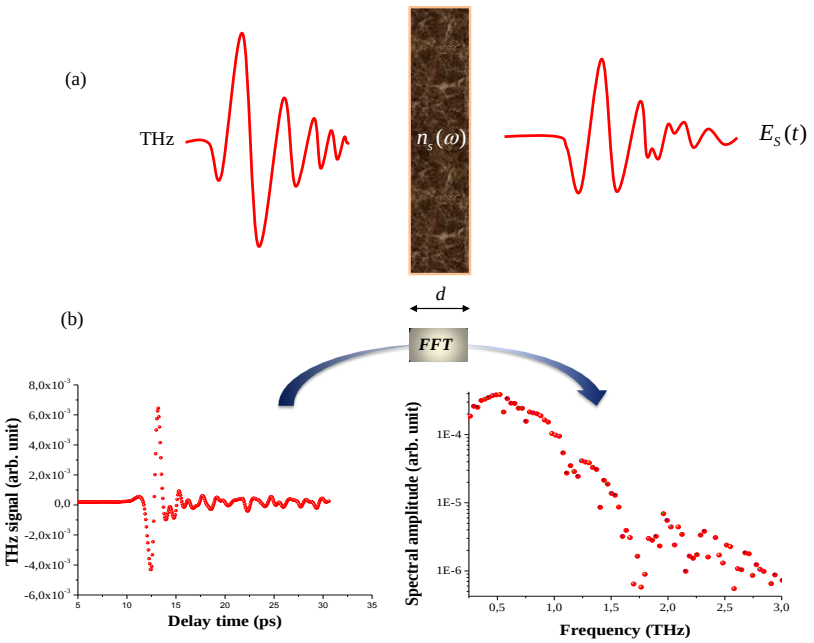

Figure 3.6: Transmission TDTS experiment. (a) Process of the extraction of the real and imaginary refractive index from the sample, (b) obtained time waveform and its Fourier transformation.

$$E(\omega) = \frac{1}{2\pi} \int_{-\infty}^{+\infty} e^{-i\omega t} E(t) dt \tag{3.9}$$

the Fourier transform of the THz signal transmitted through the sample can be written as:

$$E_S(\omega) = E_o(\omega) t_{M,s} Ph_s(\omega) t_{s,M} \tag{3.10}$$

where, $E_0(\omega)$ is the THz electric field shining on the first interface reference medium-sample; $t_{M,s}$ represents the transmission coefficient of that interface;$t_{s,M}$ the transmission coefficient of the second interface sample- reference medium¸ and $Ph_s(\omega) = exp(-i\phi_s(\omega)$ represents the phase factor, where $\phi_s = \kappa_s(\omega)d$ and $\kappa_s(\omega)$ is the wave vector of the sample pulse. The phase factor represents the phase, gained when the pulse propagates through the sample with thickness d.

The Fourier transform of the THz signal transmitted through the reference can be written as:

$$E_{ref}(\omega) = E_0(\omega)\phi_{ref}(\omega) = E_0 \exp\left(-i\frac{M\omega d}{c}\right) \tag{3.11}$$

Compared with the equivalent expression for the sample signal in equation (3.10) we

observe that the transmission coefficients are absent since they are equal to unit. The ratio of the two signals ($E_s(\omega)$ and $E_{ref}(\omega)$) gives the complex transmission of the sample, $T(\omega)$, sometimes called transfer function. For normal incidence, using equation (3.9) and equation (3.10), it can be written as:

$$T(\omega) = \frac{E_S(\omega)}{E_{ref}(\omega)} = \frac{4n_s(\omega)M}{(n_s(\omega)+M)^2} \exp\left(-i\frac{\omega d}{c}(\tilde{n}(\omega)-M)\right) \tag{3.12}$$

The effect of multiple reflections in the interfaces, reference medium - sample and sample - reference medium (Fabry-Pérot effect) as one of the TDTS measurement error sources may be accounted for, by incorporating the factor $FP(\omega)$as follows [[57]:

$$T(\omega) = \left[\frac{4n_s(\omega)M}{(n_s(\omega)+M)^2} \exp\left(-i\frac{\omega d}{c}(\tilde{n}(\omega)-M)\right)\right] FP(\omega) \tag{3.13}$$

where

$$FP(\omega) = \frac{1}{M - \left[\frac{n_s(\omega)-M}{n_s(\omega)+M} \exp\left(-2i\tilde{n}(\omega)\frac{\omega d}{c}\right)\right]} \tag{3.14}$$

This effect will be however neglected in our analysis because our samples are thick enough so that the Fabry-Pérot echo is considerably retarded, and therefore it is easily discriminated from the main signal. Also, aware of some error sources beside the FPE such as inhomogeneities in the thickness of the samples, mechanical positioning errors in the samples' mounting and replacement with with identical samples during several measurements etc., a special care was taken in order to get rid of them or to get them to minimum negligible in the measurement results.

Our aim is to find out the absorption coefficient and the real refractive index of the sample from the measurements of $E_s(\omega)$ and $E_{ref}(\omega)$. A relationship between them has to be established.

The ratio between the sample and the reference signal can be written as

$$\frac{E_S(\omega)}{E_{ref}(\omega)} = A(\omega)\exp(i\varphi(\omega)) \tag{3.15}$$

or using the equation 3.12

$$\frac{E_s(\omega)}{E_{ref}(\omega)} = A(\omega)exp(i\phi(\omega)) = \frac{4n_s(\omega)M}{(n_s(\omega)+M)^2}exp\left(-i\frac{\omega d}{c}(n_s(\omega)-M) - n_i(\omega)\frac{\omega d}{c}\right)$$
$$= \frac{4n_s(\omega)M}{(n_s(\omega)+M)^2}exp\left(-i\frac{\omega d}{c}(n_s(\omega)-M\right)e^{-1/2\alpha_s d} \tag{3.16}$$

where $n_i(\omega) = \alpha_s(\omega)c/4\pi\nu$

Since in the experiments, polyethylene was used as a reference medium then, $M = n_p$, where n_p represents the polyethylene refractive index. From equation (3.16) we can write the following expressions for the refractive index and absorption coefficient of the sample:

$$n_s(\omega) = \frac{c\phi(\omega)}{\omega d} + n_p \tag{3.17}$$

$$\alpha_s(\omega) = \frac{2}{d}\ln\left(\frac{4n_s(\omega)n_p}{A(\omega)(n_s(\omega)+n_p)^2}\right) \tag{3.18}$$

This procedure of the extraction of the material parameters cannot be used for an optically thin sample in which the main pulse and the multiple reflections are superimposed. The multiple reflections are also recorded and cause Fabry-Pérot resonances in the Fourier transformation of the terahertz signal. In addition, the relative error of the measured thickness of a thin sample is typically large, which leads to a large error in n and α.

3.4.1 Summary

In this chapter a brief discussion on methods for data analysis is presented. Although the reflection geometry has not used in this work, a short approach into basic data analysis formulation is presented. Being one of the instruments of outmost importance for this work, the data analysis for transmission geometry was thoroughly revised and the fundamental analytical expressions for refractive index and absorption coefficient extraction have been highlighted. To minimize error effects during the TDTS measurements and for sake of correct experimental data interpretation, a careful spectrometer setup and samples' mounting schemes have been engineered.

Chapter 4

Time-domain THz Spectroscopy and Continuous-wave THz Imaging on Ex-vivo Colon and Rectum Tissue

4.1 Time-Domain THz Spectroscopy on Ex-vivo Colon and Rectum Tissue

In light of developments over the last several decades, the notion of TDTS, implies generation and detection of THz pulses in a coherent manner using femtosecond laser pulses. The terahertz frequency range is one of the last-to-be-studied ranges in the whole scale from radio to $X - rays$. Effective broadband, coherent THz emitters and low-noise detectors became available only within the last few decades, mainly due to the development of lasers with ultrashort pulse duration.

Several research groups have been working on THz cancer diagnosis based on spectral detection of water [22, 58], since many cancerous tissues show higher hydration in comparison to the healthy (normal) ones [59], a situation which is also known from PET, NIR and MRI (magnetic resonance imaging) [60–62]. Other groups have been concentrated on the detection of cell structure modifications known to be associated with cancer [20, 27]. It was found the high hydration of neoplastic tissues is not the only factor contributing to the noticeable contrast on the THz absorption coefficient, refractive index spectra, and on the THz images. A number of works related with THz imaging of biological tissues, fixed with formalin and embedded in paraffin prior to the experiments, have found that the contrast between cancer-affected and the adjacent normal tissue persisted, although lower than in freshly excised tissue [20]. Chercasova et al [63], found absorption traces of tryptophan amino acid, proteins and trypsin in

dried bio-material, a fact that confirms the existence of factors contributing to the contrast other than water. Recently, A. Pierangelo *et al*, characterized human colon cancer *ex-vivo* using Mueller polarimetric imaging [64].

The presence of water in freshly excised tissues constitutes a great challenge since the strong absorption of water is potentially masking the absorption spectra of other contributing factors. Moreover, not expected sharp absorption peaks are expected to be observed in biological tissues' spectra because the samples contain a complex mixture of several molecules. For each molecule there are several chemical environments which contribute to the smooth-shape of the spectral features of the biological tissues.

To study the effect of water and other factors on the cancer contrast we decided to carry out an investigation on formalin-fixed tissues and paraffin embedded biological tissues. In this study, we show that the transmission time-domain terahertz spectroscopy (TDTS) and the complementary continuous wave terahertz imaging (CWTI), could contribute for the detection of colorectal cancer in ex-vivo. This study could be an intermediate step toward in-vivo detection of this type of cancer.

4.1.1 Hydration of cancer cells

It was found that a progressive increase in cell hydration, induced by successive genetic or epigenetic changes, is the basic mechanism of multistep carcinogenesis, and also that the degree of malignancy increases with the degree of cell hydration [65,66]. Moreover, the enhancement of metabolic activity by increased cell hydration will increase the ability of tumor cells to compete for nutrients with their normal counterparts. Increased cell hydration causes cancer by promoting cell division and oncogene expression, by inactivating genes inducing cell differentiation and by preventing apoptosis. The increased hydration of cancer cells accelerates their respiration rate – an effect which could play a major role tumor promotion and in the postulated mechanism of multi-step carcinogenesis.

The colon and rectum are biological tissues with elevated fat content, which implies that they have low water content. Consequently the contrast in THz measurements will be lower than in muscle tissue. There is a need for more research and suitable theoretical models in the THz techniques for cancer detection, as well as more experimental studies [20] in order the THz techniques for cancer detection to be well established.

The high contrast between tumor and normal tissues based on the presence of water can be useful for the implementation of THz diagnostic techniques for in-vivo or freshly excised tissue. THz studies on dehydrated or dried biological tissues have also shown good contrast (although lower than water) and, therefore, detection based on factors different from water can be also explored. Particularly, the distinguishable THz spectra

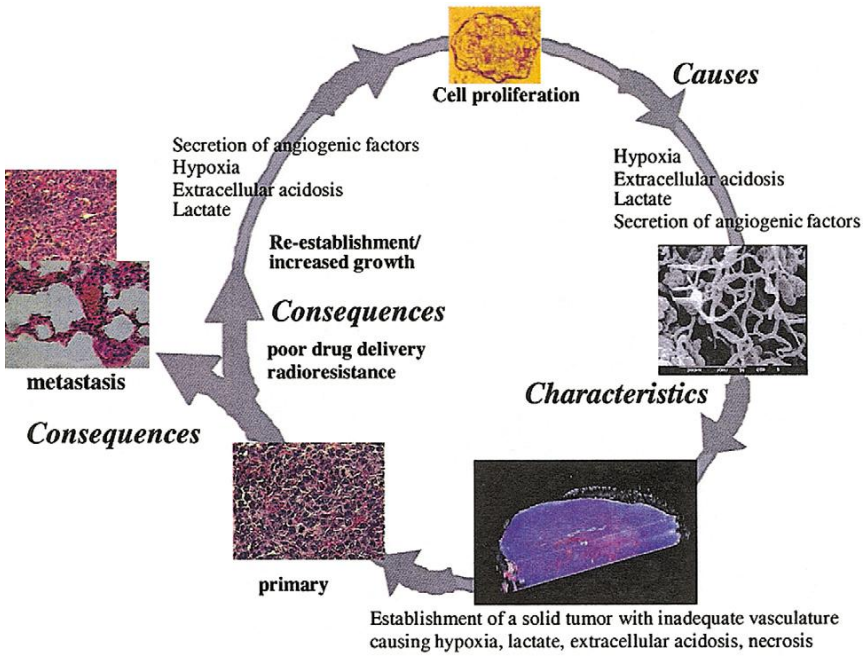

Figure 4.1: Diagramma representating the causes, characteristics and consequences of the tumor environment [5–9].

amongst the proteins indicate the potentiality of THz techniques for protein analysis and cancer detection.

4.1.2 The tumor microenvironment

The tumor microenvironment is a complex system of many cells that participate in tumor progression. The cells, vessels, and molecules, that surround a tumor, influence the tumor cells, and the microenvironment can be changed by the tumor. The hypoxia (low oxygen) and anoxia (complete lack of oxygen) and extracellular acidosis (low extracellular pH) are the hallmarks of the metabolic environment in the tumors, (Figure 4.1), [5–9]. Both oxygen tension (pO2) and pH are the utmost determinants on tumor growth, metabolism, and several therapeutic modalities such as radiotherapy, photodynamic, chemotherapy, etc.

Components of the microenvironment

The components of the microenvironment can be grouped into four categories: cancer cells, non-cancer cells, secreted soluble factors, non-cellular solid material, including the extra-cellular matrix.

4.1.3 Different types of tumors

Carcinomas result from altered epithelial cells, which cover the surface of our skin and internal organs. Most cancers are carcinomas. Sarcomas result from changes in muscle, bone, fat, or connective tissue. Leukemia results from malignant white blood cells. Lymphoma is a cancer of the lymphatic system cells that derive from bone marrow. Myelomas are cancers of specialized white blood cells that make antibodies.

4.1.4 Angiogenesis

Although tumor cells are no longer dependent on the control mechanisms that govern normal cells, they still require nutrients and oxygen in order to grow. All living tissues are amply supplied with capillary vessels, which bring nutrients and oxygen to every cell. As tumors enlarge, the cells in the center no longer receive nutrients from the normal blood vessels. To provide a blood supply for all the cells in the tumor, it must form new blood vessels to supply the cells in the center with nutrients and oxygen. In a process called angiogenesis [67], tumor cells make growth factors which induce formation of new capillary blood vessels (Figure 4.2). The cells of the blood vessels that divide to make new capillary vessels are inactive in normal tissue; however, tumors make angiogenic factors, which activate these blood vessel cells to divide. Without the additional blood supplied by angiogenesis, tumors can grow no larger than about half a millimeter and tumor cells also cannot spread, or metastasize to new tissues.

4.1.5 The Structure of the Gastrointestinal Tract

The intestine (bowel) is part of the digestive system - a tube that begins at mouth, forms stomach, small intestine, the large bowel (colon and rectum) and ends with the anus, see (Figure 4.3). The colon and rectum are located in this gastrointestinal tract (GIT) system. It is made-up of two main parts, the colon and the rectum, which are the lower part of the digestive tract measuring about 80 to 100 cm and 12 to 15 cm respectively. The colon absorbs large amount of water and salts from broken-down food and the rectum stores the waste material until it is removed from our body through the anus.

Colon and rectum cancers are those cancers which start in the colon and in the rectum respectively. Since they have many features in common, they are very often called with a unique name of colorectal cancer. The colon and the rectum cancers develop slowly along several years. Before cancer development, a growth of tissue or benign tumor normally starts as a non-cancerous polyp (non cancerous tumor) on the inner colon or

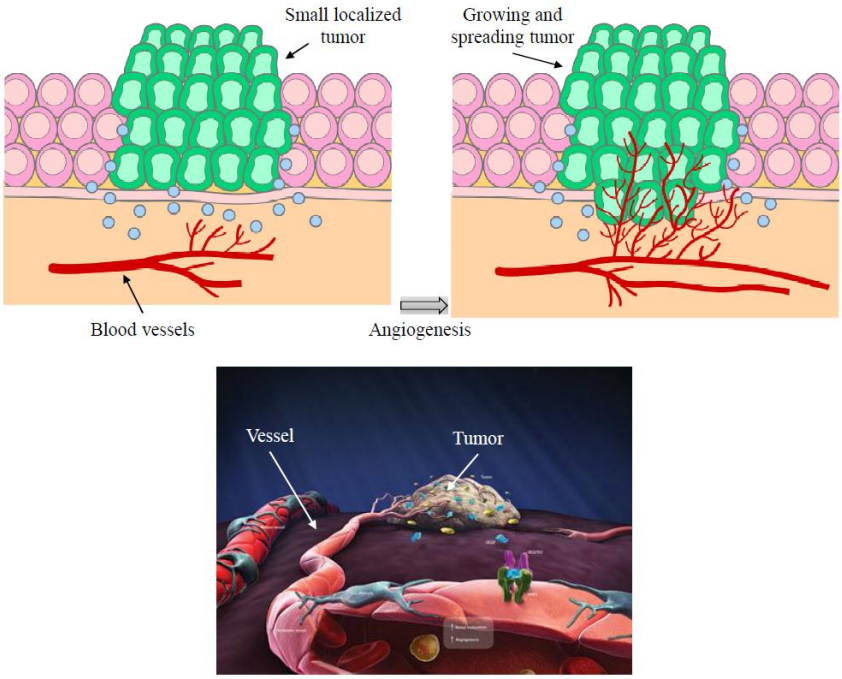

Figure 4.2: Tumor-induced angiogenesis [10]

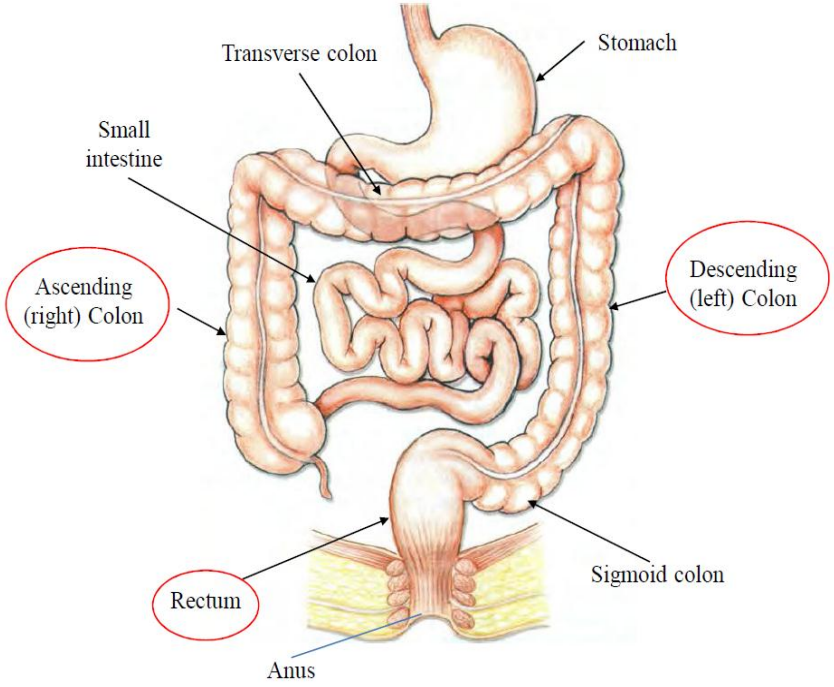

Figure 4.3: Gastrointestinal tract system. The parts within red circles are the targets of the present study [11]

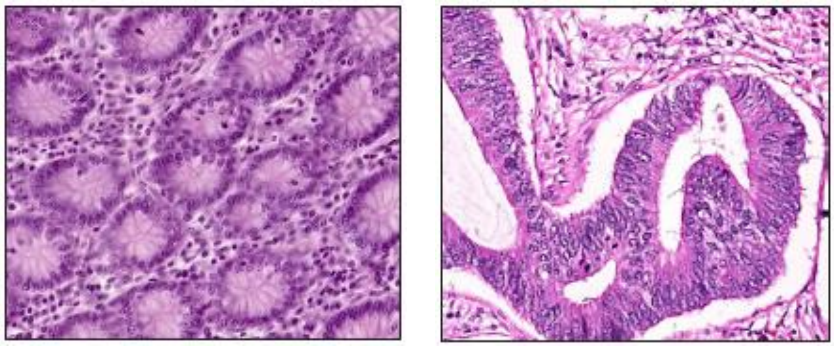

(a) (b)

Figure 4.4: (a) Normal colon tissue and, (b) colon adenocarcinoma, which may progress slowly without showing any symptoms up to 5 years.

Table 4.1: Types of GI carcinomas

Carcinoma	Description
Adenocarcinoma	Almost 95% of cancers of colon and rectum are adenocarcinomas. They begin in cells which forms glands that make mucus that lubricates the colon or rectum tube.
Carcinoid tumors	They start from specialized hormone-producing cells of the intestine.
Gastrointestinal stromal tumors	They start from specialized cells in the wall of the colon (intestine cells of Cajal).
Lymphomas	They start in lymph nodes, but may also start in the colon, rectum or other organ. Lymphomas are immune system cells' cancers.

rectum epithelium, (Figure 4.4). With the time it becomes an adenomatous polyps or adenomas that are polyps potentially transiting into cancer stage.

4.1.6 Types of cancer of colon and rectum

The types of cancer can be classified according to the type of biological tissue or body region they have started. A classification of the types of colorectal cancers is presented in Table 4.1. And in the Table 4.2, a list of brief definitions on colorectal cancers is presented.

Table 4.2: Brief definition of terms on colorectal cancer

Carcinoma	A type of cancerous, or malignant tumor originating in a glandular (tubular) structure
Polyp	A benign tumor found in the colon. Polyps can become cancerous.
Malignant tumor	Cancerous and capable of spreading
Invasive, Infiltrating tumor	Capable of spreading to other parts of the body
Lymphatic	Relating to lymph glands (lymph nodes).
Colon	The section of the large intestine leading to the rectum

4.1.7 Layers of the colon and rectum wall

The colon and rectum tract are sections of the large intestine, a tube-like structure characterized by a wall consisting of layers such as mucosa (the inner lining layer), muscularis mucosa (a thin muscle layer outer limit of the mucosa), submucosa (the fibrous tissue beneath the muscularis), muscularis propria (a thick muscular layer), and subserosa and serosa (the outmost layer of connective tissue covering most of the colon but, not the rectum), (Figure 4.5). The colon and rectum cancer starts in the innermost layer and grows through some or all of the outer layers and sometimes outward through the wall spreading to adjacent structures and the regional lymph nodes as can be seen in Figure 4.6.

4.1.8 Experimental Set-up and Sample Preparation

Experimental Set-up

Our measurements have been made using a broadband bench-top time-domain terahertz spectrometer system [68], where both the emitter and detector are PCAs. The set-up uses a pair of of-axis parabolic mirrors (OAPMs): one focus the THz beam in the samples and the other to collect the transmitted beam. The emitter is pumped by 150 fs pulses of a Ti:sapphire laser with a repetition rate of 80MHz. The system (see Figure 3.3) generates electromagnetic pulses of broadband THz radiation ranging from ~ 0.23 up to 3 THz with a spectral resolution of $<$15GHz. A photoconductive coherent detection allows the measurement of both amplitude and phase of the transient electric field. Using attached LabView-based software, it was possible to extract the frequency-dependent refractive index and the absorption coefficient.

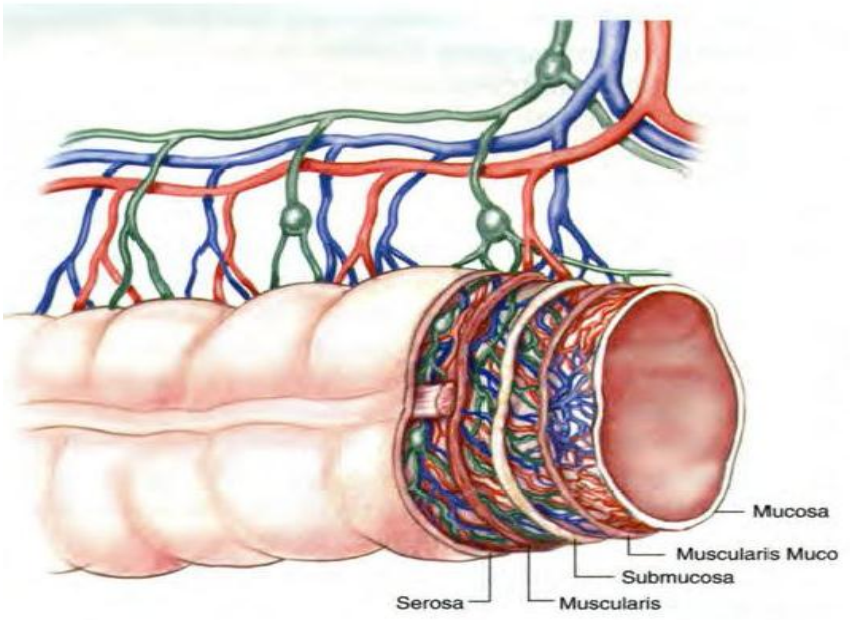

Figure 4.5: A section of colorectal layered wall [11].

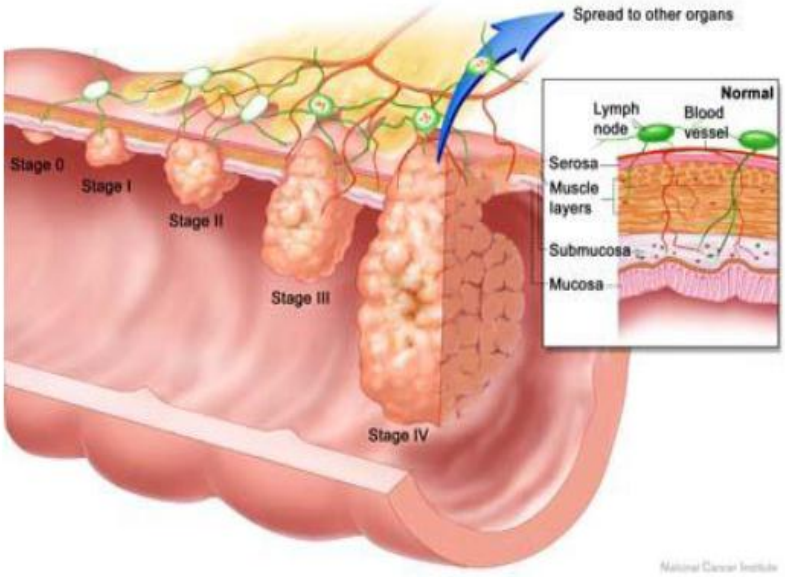

Figure 4.6: A longitudinally colorectal section indicating the stages of evolution of cancer: Stage 0, early cancer phase, found in the innermost lining layer of the colon or rectum; stage I, where the cancer has invaded more of the inner wall; stage II, where the cancer has spread outside the colon or rectum to nearby tissue; stage III, where the cancer has spread to lymph nodes but not to other parts of the body; stage IV, where the cancer has spread to other parts of the body [11].

Table 4.3: Main EKSPLA PCAs specification

Measure	Maximum permissible
Illuminated Emitter Resistance	8MΩ
Illuminated Detector Resistance	0.8MΩ
Pump Laser-Beam Power	125mW
Probe Laser-Beam Power	50mW
Power Supply Voltage	50V

Technical Implementation

The main challenge of the THz imaging and spectroscopy set-up is the alignment of the optical and THz beams. The optical beam has to be aligned with the emitter, the detector and all other optical components. The THz beam has to be aligned through the optical system including the OAPMs in order to maximize the quality of the THz signal reaching the detector. The mounting and alignment of the sample holder fixed to an arm-like post is also challenging.

The output shape of the THz pulse is sensitive to the position and alignment of the optical pump and the probe beam as well as the THz optics. The pump and probe beams sent to the emitter and the detector, respectively, have to be thoroughly monitored in order not to exceed their specifications (Table 4.3). Figure 4.7 shows the laboratory implementation of the schematic of the Figure 3.3.

4.1.9 Experimental data analysis

The transmitted THz electric field pulses were measured by a detector and Fourier transformed through a numerical operation. Considering normal incidence and neglecting multiple reflections in the interfaces, the complex transmission spectra for the reference (polyethylene sandwich containing polyet), $E_{ref}(\omega)$, and for the signal (polyethylene sandwich containing the sample), $E_s(\omega)$, can be expressed as [69]:

$$E_{ref}\left(\omega\right) = E_{in}\left(\omega\right) t_{a,p} t_{p.a} \exp\left(ik_p\right) \tag{4.1}$$

$$E_s\left(\omega\right) = E_{in}\left(\omega\right) t_{a,p} t_{p,a} t_{p,s} t_{s,p} \exp\left(-\frac{\alpha_s(\omega)d}{2}\right) \exp\left(i\kappa_s(\omega)d\right) \tag{4.2}$$

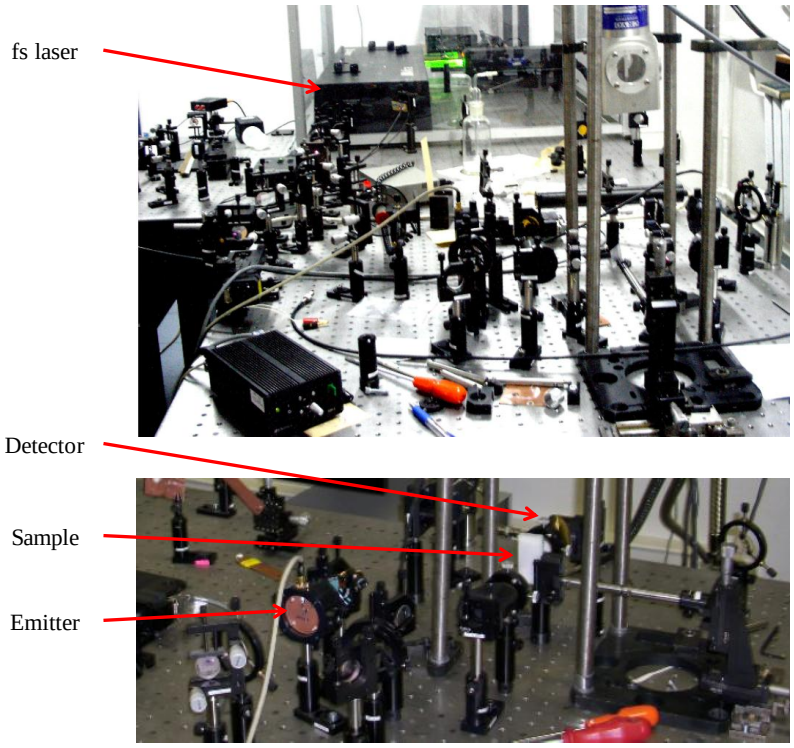

Figure 4.7: The bench-top TDTS set-up used in this work. The lower part of the picture shows the sample position.

where $E_{in}(\omega)$ is the spectrum of the incident pulse, $k_p = 2\pi n_p/\lambda_0$ and $k_s = 2\pi n_s(\omega)/\lambda_0$ are the amplitudes of the wave vector for the polyethylene and the tissue, respectively, λ_0 is the wavelength of THz radiation, $n_s(\omega)$ is the real average refractive index of the tissue, d is the tissue thickness, $\alpha_s(\omega)$ is the tissue absorption coefficient and, $t_{p,a} = 2n_p/(1+n_p)$, $t_{a,p} = 2/(1+n_p)$, $t_{p,s} = 2n_p/(n_p+n_s(\omega))$, $t_{s,p} = 2n_s(\omega)/(n_p+n_s(\omega))$ are the Fresnel transmission coefficients of THz pulses for normal incidence, where the subscripts p refers to polyethylene, and s to tissue.

From the ratio $E_s(\omega)/E_p(\omega) = A(\omega)\exp[i\varphi(\omega)]$, the index of refraction and the absorption coefficient can be calculated through the equations 3.17 and 3.18.

In the process of extraction of the optical frequency-dependent constants of materials, the dynamic range (DR) of a TDTS is also taken in account. Due to the typical single-cycle regime of the THz pulse, the spectral amplitude is strong at low frequencies, and normally a characteristic gradual roll-off occurs at high frequencies until the detected THz signal approaches the noise level at the experiment (Figure 4.8b).

The DR of a TDTS set-up is defined as the signal above the noise level of the spectrum. It is determined by the Fourier transformation of the measured temporal waveform (i.e., the spectrum of the THz radiation extracted from its time-waveform in the scanning period, $0-T$) above the noise level. The noise N includes the noise due to fluctuations

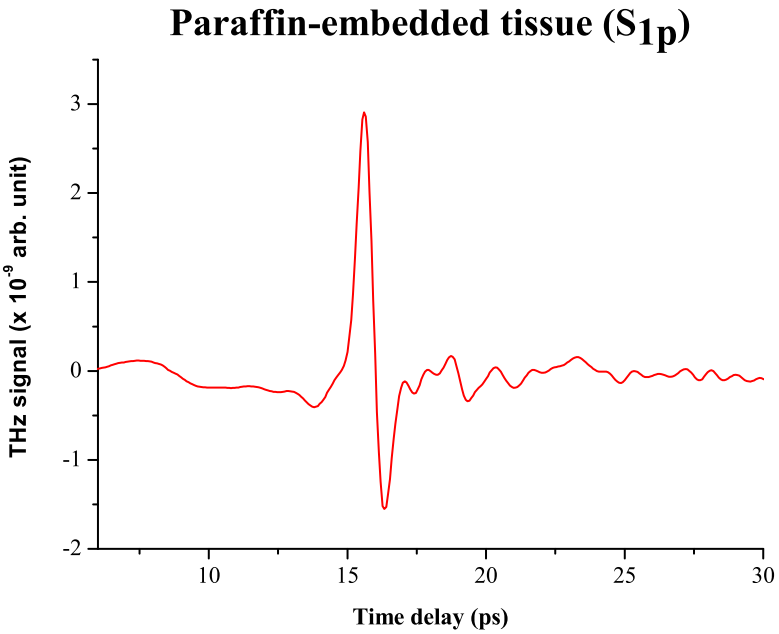

(a) Temporal signal

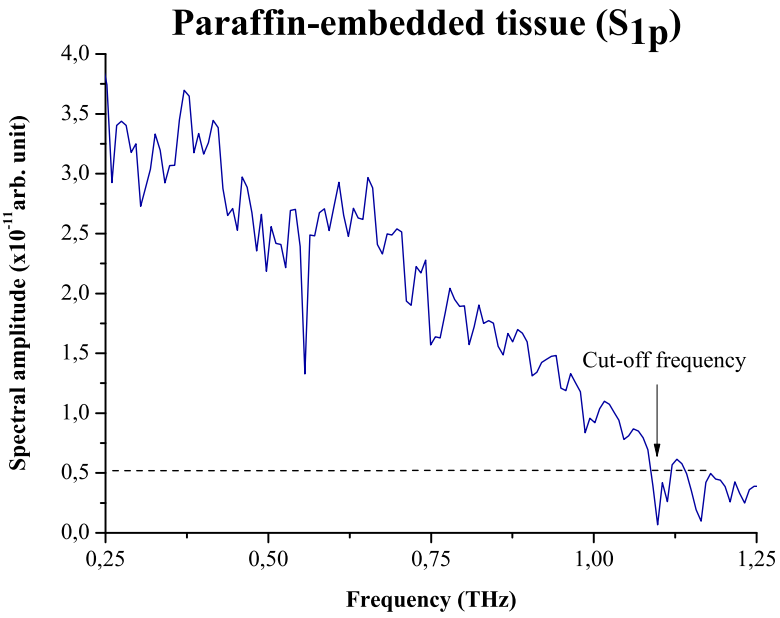

(b) Signal spectrum

Figure 4.8: A THz pulse transmitted through the paraffin-embedded sample (S_{1p}) measured in this work and the corresponding spectrum. In (b) the horizontal dot line represents the noise floor.

in the THz field, $N_{THz}(t) = R(t) \cdot E_{THz}(t)$, where $R(t)$ is a dimensionless random ratio, and the background noise from the detection of the THz. The background noise includes the optical probe-beam shot noise $N_{OPB}(t)$ in the detector which is proportional to the recorded current, and all noises in the detector gathered together, such as Johnson noise, amplification noise, thermal noise, the zero-THz-field photocurrent, etc.

Analytically the DR can be given by [[70].

$$DR(\omega) = \frac{k(\omega)}{\sqrt{\frac{\delta t}{2\pi}\left(\frac{\kappa}{S}\right)^2 + \frac{T\delta t}{2\pi}\frac{1}{D^2}}} \tag{4.3}$$

where $k(\omega) = E(\omega)/A_{THz}$ with A_{THz} representing the maximum amplitude of the THz field in time-domain, is a factor dependent upon the actual waveform, δt is the temporal intervals at which the temporal waveform of the THz pulse is sampled, $S = 1/\sigma_R$, is the temporal measurement signal-to-noise ratio (SNR), T is the sampling range, $D = A/s_B$ where A represents the maximum amplitude of the THz field in time-domain is the temporal dynamic range, and

$$\kappa = A^{-1}\sqrt{\int_{-\infty}^{\infty} |E(t)|^2 dt} \tag{4.4}$$

Actually, the DR limits the maximum magnitude of the absorption coefficient that could be observed along the higher frequencies. The effect of the DR may wrongly be perceived as an absorption peak in samples whose absorption increases toward high frequencies and begins rolling-off resembling a signal peak.

Figures 4.8a and 4.8b show a THz pulse and the corresponding frequency spectrum normalized to the noise level. This normalized spectrum is normally considered as a good measure of the frequency-dependent $DR(\omega)$ of the correspondent experiment.

From equation 3.18 it can be found that the maximum absorption coefficient, $\alpha_{max}(\omega)$ which can be measured reliably with a given $DR(\omega)$ corresponds to the situation where the sample signal is attenuated to a level approaching the noise level and can be given by [71], (i.e., the maximum of absorption coefficient data reliable can be obtained only in the range within the $DR(\omega)$ of the experiment:

$$\alpha_{\max}(\omega)d = 2\ln\left(DR(\omega)\frac{4n_s(\omega)}{(n_s(\omega)+1)^2}\right) \tag{4.5}$$

Values of $\alpha(\omega)$ larger than $\alpha_{max}(\omega)$ cause the detector saturation and therefore can't be measured.

4.1.10 Sample Preparation

Formalin Fixation and its effect on biological tissue

Chemical fixatives are used to preserve tissues for routine histopathological examination and the fixed samples maintain the structure of the cells including the sub-cellular components such as cell organelles such as nucleus, endoplasmic reticulum, mitochondria. They do that by irreversibly cross-linking proteins. In the case of formaldehyde, the main action of these aldehyde fixatives is the cross-linking of amino groups in proteins through the formation of CH2 (methylene) linkage. The most recommended fixative is a 10% neutral buffered formalin solution [72].

It is known that the biological tissue, mainly the skeletal muscle cell structure, contents water at high percentage, around 75 to 80% [73]. Embedding biological tissue in formalin, water is being replaced by gel-like rigid compound, reducing both the absorption coefficient and the refractive index. Since the adipose tissue contains less water than the muscle, the differences in the THz properties of this tissue typology will be very noticeable.

Frozen section fixation was the method used for the histological examination of the first set of colonic and rectal tissue of the present study. It is a rapid way to fix and mount histology sections. It allows rapid determination of tumor margins assuring that the tumor has been completely removed during the surgery.

Biological tissue has little inherent contrast in optical and electron microscopes. Staining is employed to give contrast to the tissue and to highlight particular features of interest (affected regions) [74] as shown in Figure 4.9.

The frozen tissue-samples, taken from a cryostat, have been sliced using a microtome, mounted on a thin glass slide and stained using the standard procedures. After histological observation of these thin samples, it was possible to demarcate the cancerous and health bulk regions of the thick sample for further THz studies (Figure 4.9).

Staining by Frozen Section Fixation Method

Biological tissue has little inherent contrast in either the light or electron microscope. Staining was employed to give both the contrast to the tissue as well as highlighting particular features of interest (demarcation of affected regions).

Paraffin Embedding of the Tissues

The aim of this type of tissue processing is to remove water from tissues and replace with a medium that solidifies to allow thin sections to be cut. Biological tissue must

(a) (b)

Figure 4.9: Staining and fixative process of colonic sample containing cancer diseased regions. (a) thin stained slice cut from a main specimen for demarcation of health (normal) and cancer diseased regions, (b) formalin fixed specimen for THz studies.

be supported in a hard matrix to allow sufficiently thin sections to be cut. For light microscopy, paraffin is the most frequently used. Samples are transferred through baths of progressively more concentrated ethanol to remove the water [72]. Formalin-fixed and paraffin-embedded tissues may be stored indefinitely at room temperature. Nucleic acids (DNA and RNA) may be recovered from them decades after fixation, making this tissue an important resource for historical studies in medicine [75].

Procedures of the Experiments

For our experiments, two sets of samples have been measured. The first set consists of two tissue typologies: colonic and rectal; both with normal and cancer affected regions (Figure 4.10). The second set consists of four samples: 1 normal colon tissue, and 3 colon tissue with normal and adenocarcinoma affected regions – all of the 4 tissues have been fixed in formalin (S_{if}, $i = 1, 2, 3, 4$) (Figure 4.11) and embedded in paraffin (S_{ip}, $i = 1, 2, 3, 4$) (Figure 4.12).

The samples have the same thickness (with a point by point variation less than 5%), unless otherwise stated, and they have been measured at the same environment conditions. Measurements have shown that paraffin has the same refractive index as polyethylene, $n_p = 1.50$ [76], for the complete range of the working frequencies, 0.23-1.25 THz.

The normal and cancer affected zones in each sample have been previously identified

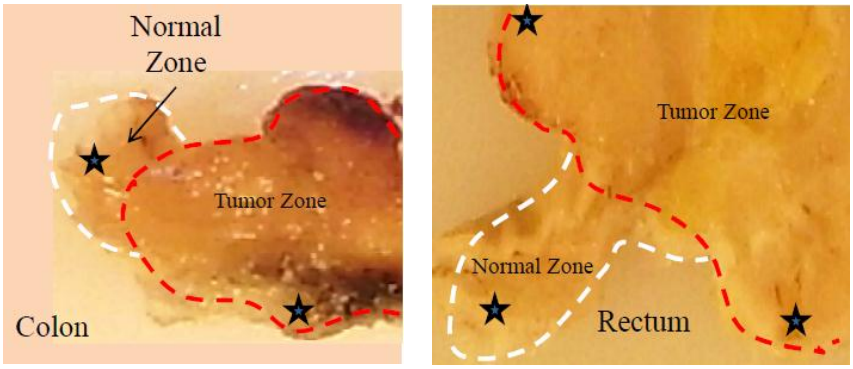

Figure 4.10: Colon and rectum tissues, with normal and cancer affected zones, that have been measured by TDTS.

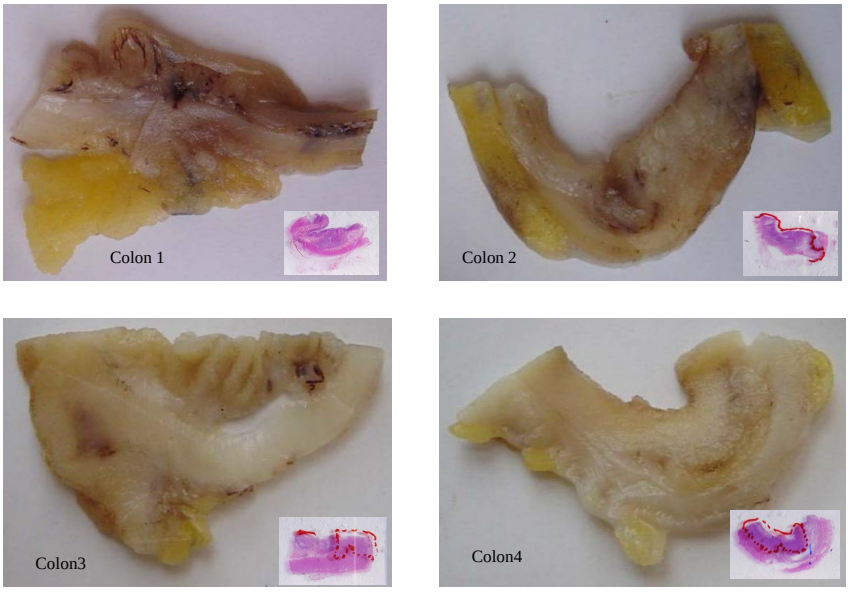

Figure 4.11: Formalin fixed colon tissue samples that have been measured by TDTS. The sample (Colon 1) comes from a normal tissue and the samples (Colon 2,3 and 4) content normal and cancer affected zones. The inset images are the stained slides used for histological examination.

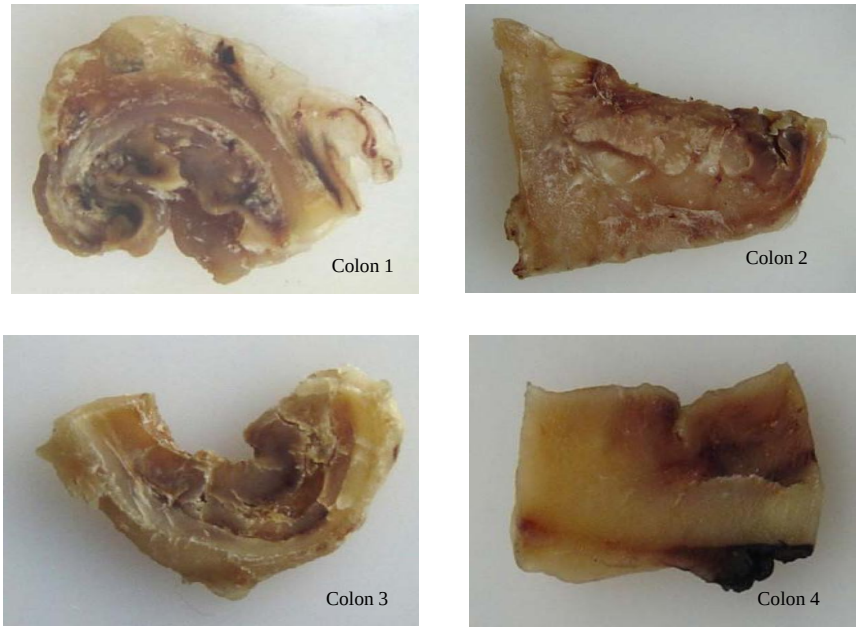

Figure 4.12: Paraffin embedded colon tissues that have been measured by TDTS. The colon tissue (Colon 1) is normal and, the tissues (Colon 2, 3 and 4) content normal and cancer affected zones. The effect of distortion and shrinkage of paraffin embedding process can be noticed in the images.

by histological examination through the stained slides (Figure 4.11). Measurements using TDTS have been performed in randomly chosen spots on the samples at room temperature. Before starting the measurements, the sample tissues have been sandwiched between two 50×30mm polyethylene plates of 2 mm thickness separated with a polyethylene spacer of variable thickness according to the thickness of measured sample, as shown in Figure 4.13. Both plates were slightly pressed onto the tissue in order to get rid of air gaps. Figures 4.13 and 4.14, are showing the process of sample mounting for the TDTS measurements.

4.2 Terahertz Imaging on Ex-Vivo Colon and Rectum Tissue

There are two types of THz imaging systems: continuous and pulsed. In this section continuous-wave THz imaging (CWTI) set-up is discussed, since the THz pulsed imaging (TPI) set-up has been the object of previous chapters. Some characteristics of THz imaging are also reviewed; the closing section is a detailed description of the imaging procedures of biological samples studied in this work.

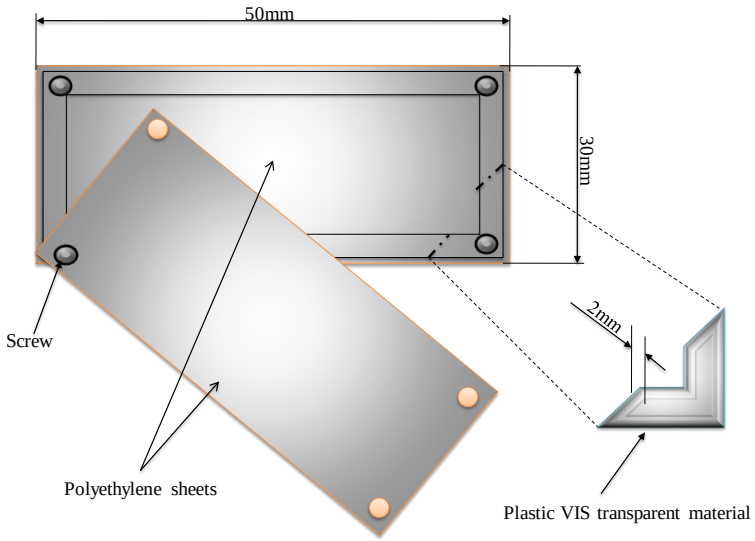

Figure 4.13: Schematic of the polyethylene sample holder. Two rectangular polyethylene thin sheets (2 mm thick), separated by a ring-like polyethylene spacer form a cell. The depth of the cell corresponds to the spacer's thickness. The specimen to be measured was dropped into the cell, and pressed with 4 screws in the cell corners, as can be seen in the Figure 4.14.

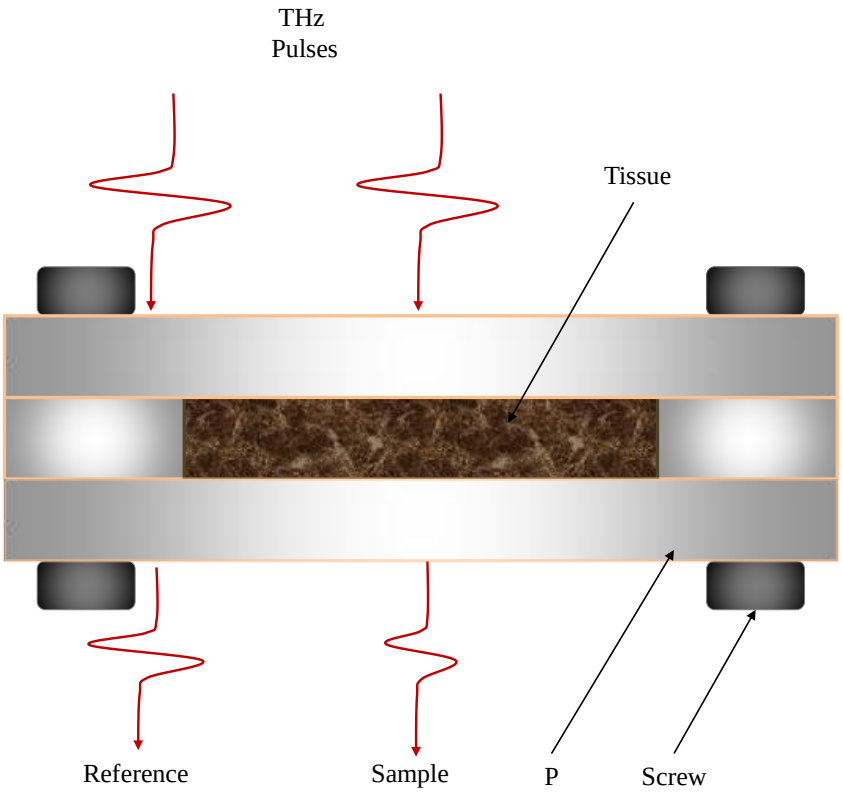

Figure 4.14: Schematic of the polyethylene holder cell, containing the bio-specimen to be measured by TTDTS.

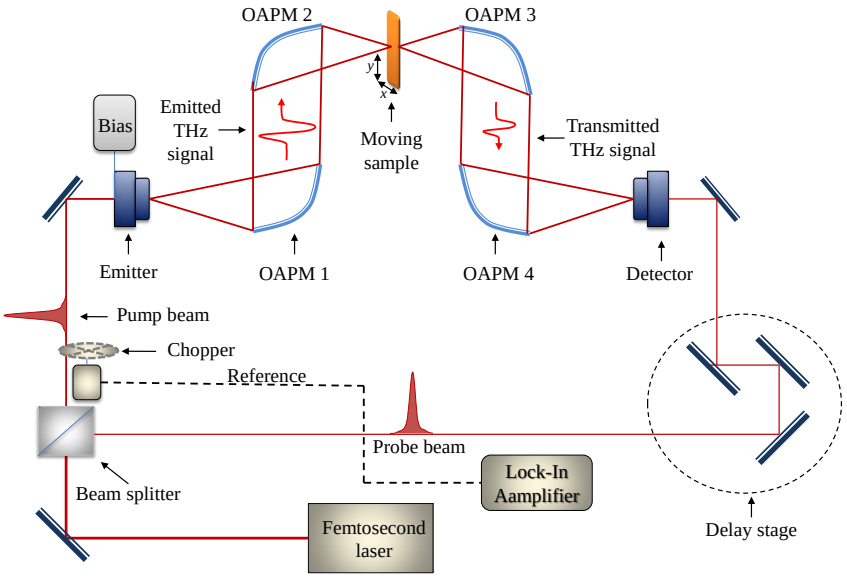

Figure 4.15: Typical TPI set-up

4.2.1 Terahertz pulsed imaging

Before going to the CWTI, let us briefly introduce the TPI. Non-linear methods or PCAs combined with ultrashort optical pulses are normally used for TPI. Here the generated THz pulses are passed through the studied sample and are detected afterward in time-domain. Figure 4.15 illustrates a typical TPI set-up.

In this THz imaging method the sample's image is obtained through the analysis of the changes in the amplitude $A(x, y)$ and phase $\phi(x, y)$ of the transmitted THz pulses. These changes map out the spatial variations (i.e., thickness, $d(x, y)$, absorption coefficient, $\alpha(x, y)$, and refractive index $n(x, y)$) of the sample. For the analysis of TPI data several approaches can be used in temporal and frequency domains. For the construction of the 2-D images, we may use the values of the maximum amplitude $A_{max}(x, y)$ or the arrival time $t_{arr}(x, y)$ of the temporal waveforms or, alternatively, the temporal spectrum for a specific frequency obtained by Fourier transformation of the temporal signal. Figure 4.16 shows a sketch of a TPI process in transmission geometry.

4.2.2 Continuous-Wave THz Molecular Gas Lasers

There are several gases that are used in molecular lasers producing lines in the range of 40 - 1200 mm (7.5 - 0.25 THz). Continuous-wave laser with powers of the order of several mW are available. The limitation of these sources is that they offer a discrete set of lines with no tuneability, and so are unsuitable for the majority of spectroscopic applications.

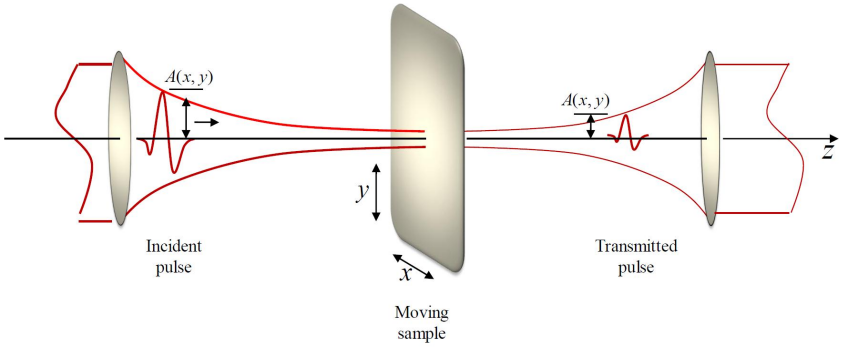

Figure 4.16: TPI by raster-scanning in transmission geometry

Table 4.4: THz generation performance of cw systems [12]

	Gunn Oscillator	**Gas Lasers**	**BWO**	**FEL**	**QCL**
Peak Power (mW)	0.1 - 100	1 - 180	1 - 50	10^8	10
Bandwidth (GHz)	10^{-2}	10^{-2}	10^{-2}	10^4	10^3
Tunability	Changing the length of the resonant cavity	Changing the excitation gas	Continuously tunable	Changing the magnetic field and the electrons' speed	Nontunable
Generated Frequency Range (THz)	0.1 - 0.8	1 - 6	0.2 - 1	10 - 100	1 - 3

Although there are numerous types of techniques for continuous-wave THz generation such as optical heterodyne down-conversion or photo-mixing, difference frequency generation (DFG), p-type germanium lasers, quantum-cascade lasers (QCL), free electron lasers (FEL), etc., in the present work an optical pumped THz molecular gas laser have been used. In Table 4.4generation performance for continuous-wave THz systems is presented.

Since the cw THz radiation sources in most CWTI systems are not synchronized (phase-locked) to an optical source which could be used for signal sampling, usually coherent detection cannot be used. The THz source and the detector are independent except in cases when the THz source is tunable, where it is possible to combine spectroscopic measurements with imaging like in TDTS systems. When a source with fixed frequency and a single detector are used, the CWTI systems are not capable to provide frequency-

Table 4.5: Comparison Between CW and Pulsed THz Systems [12]

	CW THz System	**Pulsed THz System**
Provided Information	Transmitted energy	Field magnitude, optical path length (transmission time), absorption spectrum, phase, pulse shape
Scanning Speed	$0.005\,\text{s.(point)}^{-1}$at 1 mm step size (limited by the translation stage maximum speed of $\sim 0.2\,m.s^{-1}$	$20 - 0.05\,\text{s.(waveform)}^{-1}$
Data Complexity	Low	High
System Complexity	Low	High
Approximate Cost of the System (EUR)	30 000,00 -100 000,00	60 000,00 - 200 000,00

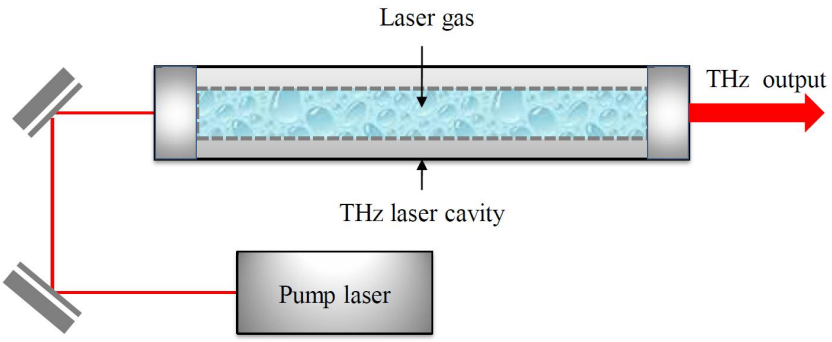

Figure 4.17: Schematic diagram illustrating a simplified view of a THz gas laser system

domain or time-domain information about the studied sample but only intensity data. Even so, they can yield energy transmission maps that are sufficient for many image applications. Furthermore, these systems are compact and simple. They do not require pump-probe system or time-delay lines and the image formation is overwhelmingly fast. The complexity of the optics is reduced compared to the THz pulsed systems and furthermore they are relatively low-cost (Table 4.5).

Because of the above enumerated reasons we have decided to use the CWTI system for sample imaging. Far-infrared (FIR) THz molecular gas laser from Edinburg Instruments have been used. A general sketch of a FIR laser is presented in the Figure 4.17.

The basic work principle of this type of lasers is quite similar to that of a normal laser systems, the only relevant difference is the existence of an intra-cavity waveguide used

Table 4.6: THz gas lasers [13]

Molecular gas	Chemical symbol	Radiated frequency (THz)	Power (mW)
Methanoic acid	HCO_2H	0.76	37
Methanol	CH_3OH	1.84	25
Difluoromethane	CH_2F_2	2.5	> 100

for confinement of the laser modes in transverse direction. These lasers employ a low-pressure molecular gas placed in a Fabry-Perrot cavity, and usually they are optically pumped with a grating-tuned CO_2 laser. Polar molecules are the gain media of THz gas lasers. They have strong absorption by the vibrational band coinciding with the emission band of the CO_2 laser, ranging from $9-10\mu$m. Some of the most common used gases are methanol (CH_3OH), difluoromethane (CH_2F_2), methanoic acid (HCO_2H), etc. They have been used in this work and their characteristics are presented in Table 4.6.

To understand how this THz laser works, we briefly re-examine the quantum-mechanical molecular processes. When the molecule has permanent dipole moment its rotational transitions absorb or emit photons. The type of molecules used for FIR lasers have permanent dipole moments so their rotational transitions are directly coupled to electromagnetic radiation through dipole interactions. The laser gases molecules are polyatomic molecules and they have complicated vibrational-rotational modes than those of diatomic molecules. As an example, consider the polyatomic molecule of water (H_2O). It has three rotational axes corresponding to three degrees of rotational freedom. In Figure 4.18 rotational degrees of freedom are shown only.

Figure 4.19$\upsilon = 0$ shows an energy-level diagram illustrating the optical excitation of a laser gas and the production THz radiation. The population inversion and gain occurs between rotational levels within excited vibrational bands.

The excitation caused by the optical pump occurs from the lowest vibrational mode, with a thermal population of rotational states given by [77]

$$N(J,K) =\propto g(J,K)e^{-E_{rot}(J,K)/K_BT} \tag{4.6}$$

where $E_{rot}(J,K) = BJ(J+1) + CK^2$ with rotational constants $B = \hbar/2I$ and $C = \hbar/\left(1/2I_c - 1/2I\right)$, is the rotational energy eigenvalues, to the first excited vibrational mode, $\upsilon = 1$. Thus THz radiation is emitted due to the optically induced population inversion between $J+1$ and $J-$leves for $\upsilon = 0$, and between J and $(J-1)-$levels $\upsilon = 1$. There also occurs a cascade transition from $J-1$ to $(J+1)-$ leves that contributes to THz radiation. Conversion efficiency here is low because a great percentage of the pumping is converted into heat. The theoretical limit on efficiency for this type of

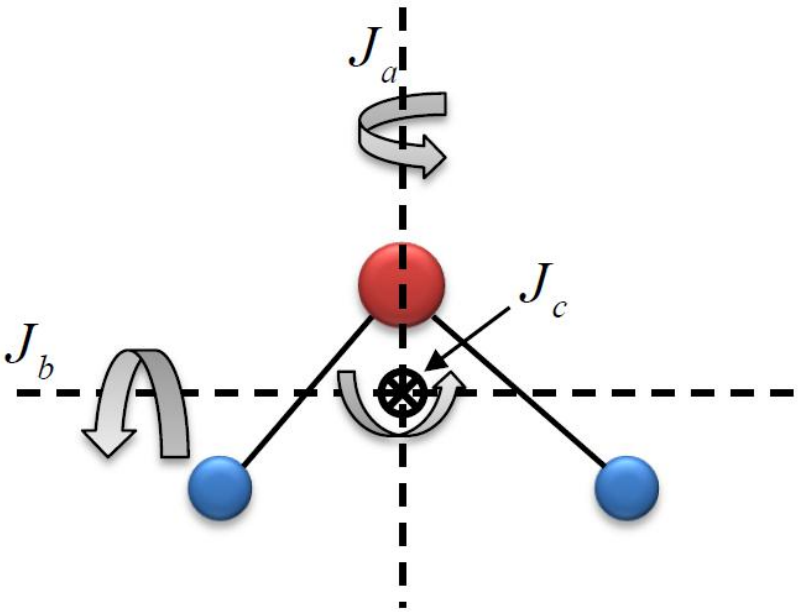

Figure 4.18: Diagram illustrating the three rotation axes of a water molecule

lasers is given by Manley-Rowe limit as follow [78]

$$\varepsilon = \frac{\nu_{THz}}{2\nu_{pump}} \tag{4.7}$$

where ε is the conversion efficiency of the pump into THz radiation, ν_{THz} is the frequency of the emitted THz radiation, and ν_{pump} is the frequency of the optical pump.

4.2.3 Continuous-Wave THz Imaging

As stated before (see chapter 3), there are two modalities of THz imaging, (a) transmission geometry imaging (for thin or minimally absorbing media) and (b) reflection geometry method (for thick or highly absorbing media). Owing to the characteristics of our samples we opted for transmission geometry modality. THz imaging can be considered as the latest technique introduced into the field of innumerous imaging technologies existent nowadays. Figure 4.20 illustrates the CWTI process. As it can be seen, the system does not need complex optics or delay-lines.

As it was already stated, our CWTI system relays on an optically pumped molecular gas THz laser, delivering a discrete spectrum of emission in the range of several mW, Kasalynas et al [79]. The laser power is monitored continuously with a bow-tie diode [80]. Pre-defined zones of the samples with dimension 40×40 mm have been

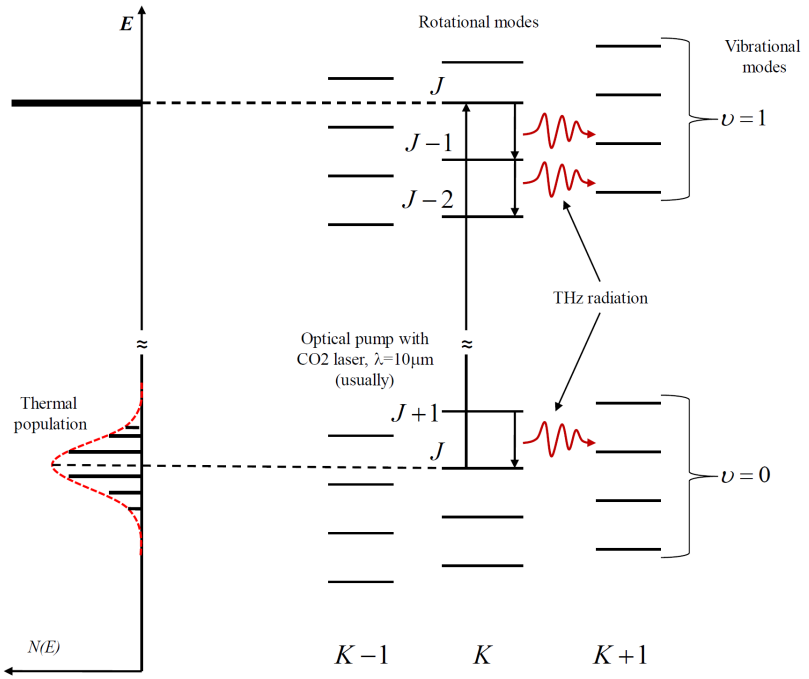

Figure 4.19: Schematic illustrating the energy-level diagram of a typical optical pumped THz gas laser

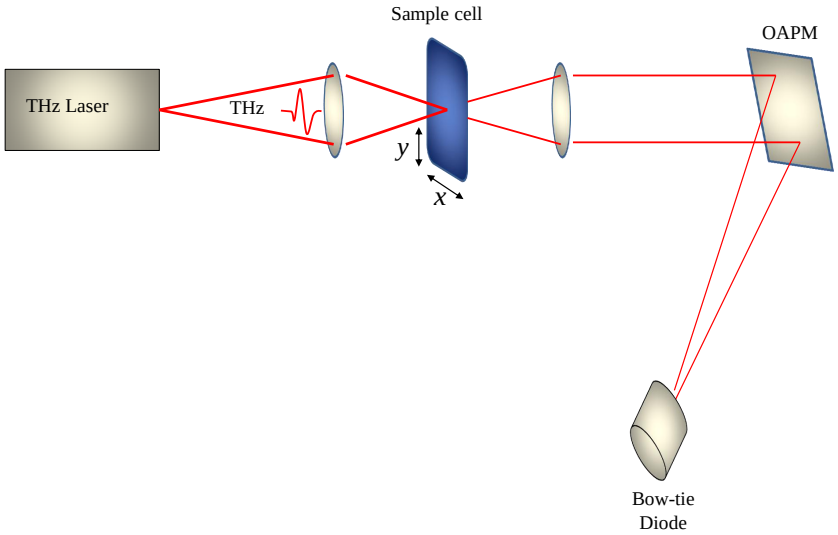

Figure 4.20: Schematic of CWTI system. The image is produced by raster-scanning of the sample. The THz imaging technology is still in its infancy and, therefore, it should be inopportune to predict the impact of this technology for years to come. For now the THz imaging is a unique and self-sufficient by its characteristics. It has already found applications which are inaccessible to other imaging techniques.

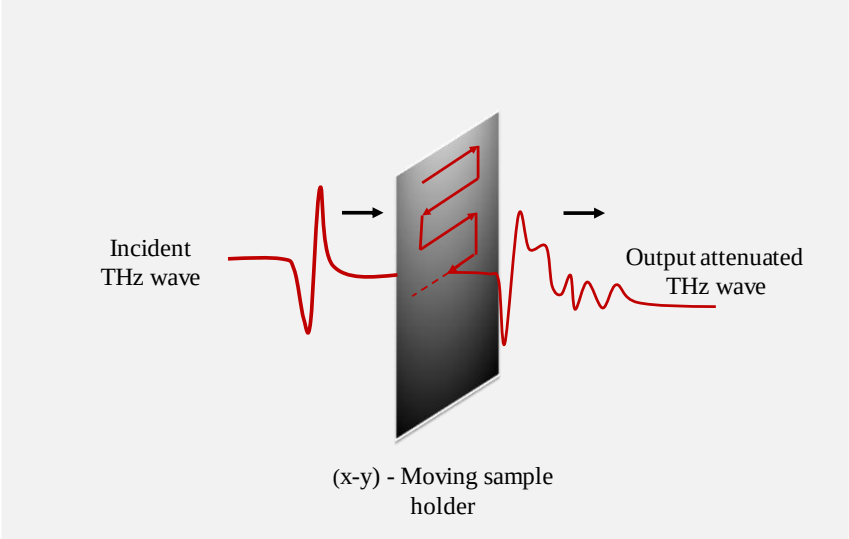

Figure 4.21: Sketch of a diagram showing the imaging procedure

imaged by scanning with a 0.95 mm beam spot diameter. Figure 4.22 is the technical implementation of the schetch shown in Figure 4.20.

The imaging method has been the raster-scanning of the sample by transmission, Figure 4.21. The sample was mapped pixel-by-pixel by raster-scanning using translation stage holding the sample. The detector measured the transmitted THz radiation through the sample. The measurements have been done at fixed frequencies of 1.84 and 0.76THz. Although THz medical imaging is at its incipiency our preliminary results (shown in the following chapter) and those of other research groups (existing in the literature) in this field, show its promising potential to provide a safe and efficient technique for medical diagnosis.

One of the promising advantages of the THz radiation in biomedical applications is that the THz techniques are non-invasive, non-ionizing ($1 - 10$ meV) and non-contact. Because of high water content of biological tissue and consequently the strong THz attenuation of this medium, the in-vivo imaging is limited to reflection geometry and for epithelial tissue diagnose only. This strong interaction of water with THz radiation, to a certain extent, becomes useful for biomedical applications. In fact, the THz imaging is sensitive to small changes in hydration levels of the biological tissue, a fact which could be a critical measure for medical diagnose for tissue normalcy and its diseased state, mainly in cancer detection. Previous studies on THz skin imaging and breast imaging [19, 20, 81] have demonstrated encouraging results in discriminating normal (health) from diseased tissue and that the obtained contrast showed well defined (when compared to histological findings) tumor margins. Up till now, studies focused to colon and rectum cancer are scarce, thus our work may be one of the few. This bring us more difficulties to make comparative analyzes on our results.

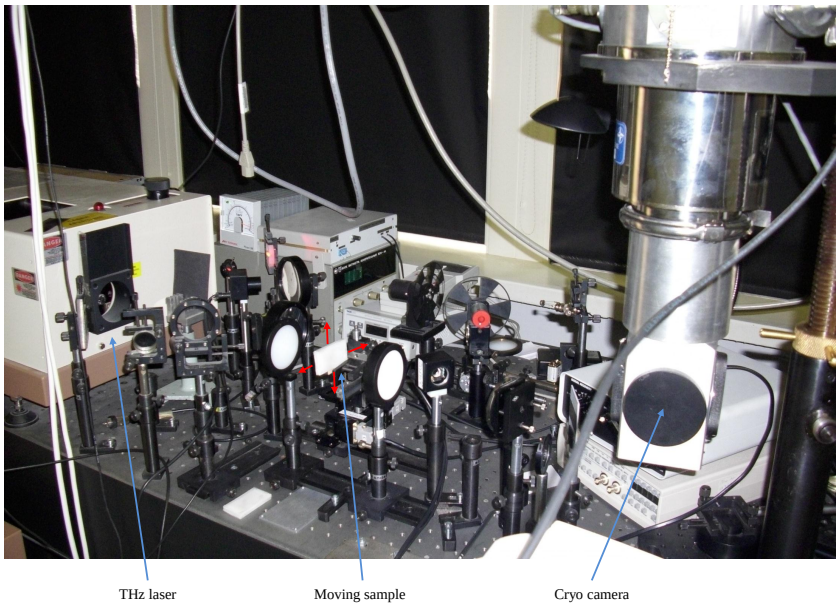

Figure 4.22: Photography of the technical implementation of the diagram of the Figure 4.20.

The THz imaging technology is still in its infancy and, therefore, it should be inopportune to predict the impact of this technology for years to come. For now the THz imaging is a unique and self-sufficient by its characteristics. It has already found applications which are inaccessible to other imaging techniques.

4.2.4 Summary

In this chapter, a brief introduction on cancer biology is made before entering the TDTS section. We describe the daunting task of the spectrometer setup, the experimental geometry alignment and the sample holder arm positioning. A brief treatment on tissues preparation (histopathologically), tissue container-cell preparation and tissue mounting procedures is shown. Experiments' dynamic range was additionally taken in account with a short explanation on how this concept is associated with the THz measurement process. Finally, a short introduction on working principles of a molecular gas laser generating/emitting continuous-waves at THz frequency range, that was used for the imaging section of this work.

Chapter 5

Experimental Results of Transmission Time-domain THz Spectroscopy and Continuous-Wave THz Imaging

5.1 Introduction

In the present chapter a summary of the experimental results is presented. In section 5.2, results of TDTS on colon and rectum tissue in transmission geometry are discussed, and in section 5.3, results of CWTI on randomly chosen tissues previously measured by TDST are also discussed.

5.2 Transmission TDTS on Colon and Rectum Tissue

Firstly a set of 2 samples with freshly excised colon and rectum tissue have been measured. Secondly a set of 8 samples comprised of four formalin-fixed colonic tissues and equal number of paraffin-embedded ones (i.e., four pairs (formalin-fixed – paraffin-embedded) have also been measured. For the sake of comparison, a normal colon tissue was also measured. As it was shown in Figure 3.5 and Figure 3.6, the THz pulse-train propagates through the sample with frequency-dependent refractive index $n_s(\omega)$ and absorption coefficient $\alpha_s(\omega)$. This pulse-train (sample signal) does experience reflection losses at the sample's interfaces as well as absorption throughout the sample, besides the changes caused by the spectrometer's optical components. The reference pulse only experiences changes caused by the optical components of the spectrometer. Thus, the extraction of the aforementioned optical parameters ($n_s(\omega)$ and $\alpha_s(\omega)$ of the sample, needs the time-domain data to be transformed into frequency-domain through Fourier

transformation. All the results presented in the present work have been obtained using the formulation for TDTS data analysis presented in chapter 3.

The TDTS measurements consisted of focusing the terahertz radiation into chosen spots of the samples and the record of the transmitted signal. Both the reference and the sample signal have been recorded. Then Fourier transformation was performed on the two THz time signals, $E_{ref}(t)$ and $E_s(t)$, and the refractive indices and absorption coefficients have been calculated. Depending upon the location of the chosen spot (i. e., less absorptive or strongly absorptive tissue's region), attenuation of the THz signal is noticeable in the recorded data transmitted through the sample. Since in thick samples, the sample pulse appears some picoseconds after the reference signal, it would be possible, using the relation $\Delta t = d(n-1)/c$, to estimate the refractive index of the measured points. In the relation, Δt represents the delay of the sample signal respect to the reference one, and d the thickness of the sample. This technique was not used in this work.

Since the central regions of the freshly excised colon and rectum tissues were strongly absorptive and therefore, no transmitted THz signal could be measured, the tissues

borders have been eligible for the randomly chosen spots for TDTS measurements. As was above stated, from the obtained time-waveforms the respective absorption coefficients and indices of refraction have been calculated using the spectral data yielded by Fourier transformation.

Figure 5.1 shows the transmitted time-waveforms for the reference signal and the sample signals. Figure 5.2 presents the spectral amplitudes of the signal corresponding to spots of normal rectum tissue and Figure 5.3, affected rectum tissue. Figure 5.4 and Figure 5.5 show the absorption coefficient and the index of refraction for rectum tissue respectively. Differences between healthy and cancer affected tissues are visible in this sample, over the complete working frequency range. The differences are not clear in the colonic tissue for frequencies higher than 1.5 THz (Figures 5.6 and 5.7). The presence of fat-like tissue structure, observed in both colon measured spots, may explain this result, as it will be discussed later. For completeness, plots of n as fuction of α have also been analyzed and are shown in Figure 5.8 , for rectum and Figure 5.9, for colon.

With the second group of samples we have not faced problems related with low THz beam transmittance, since they have been submitted to fixation processes (formalin fixation and paraffin embedding), actions that remove significantly the water content in the tissue, lowering consequently the power absorption of the samples. A sequence of data treatment of 3 measured spots for a single paraffin-embedded tissue is presented. It begins with a cluster of temporal waveforms: one passed through the polyethylene window only (reference) and three passed through 3 randomly chosen spots on the tissue

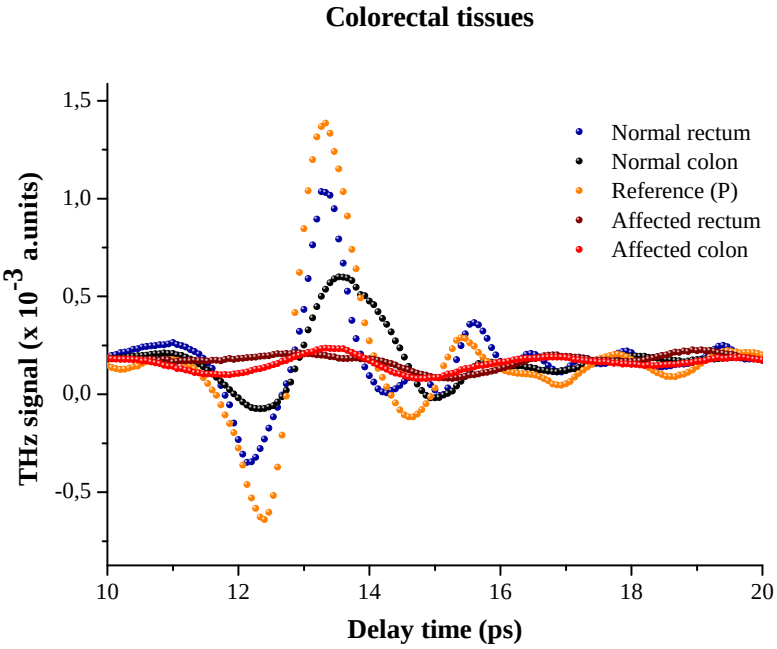

Figure 5.1: Time signals of colonic and rectal tissues.

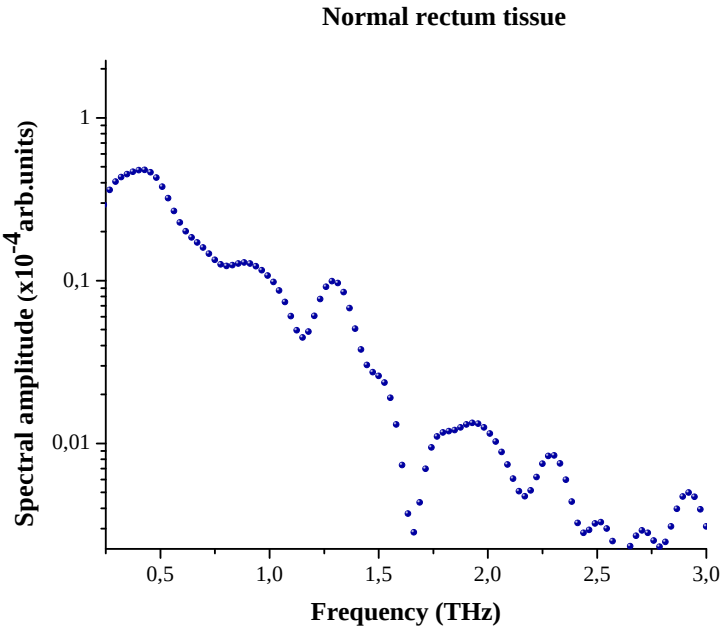

Figure 5.2: Spectral amplitude of normal rectum tissue.

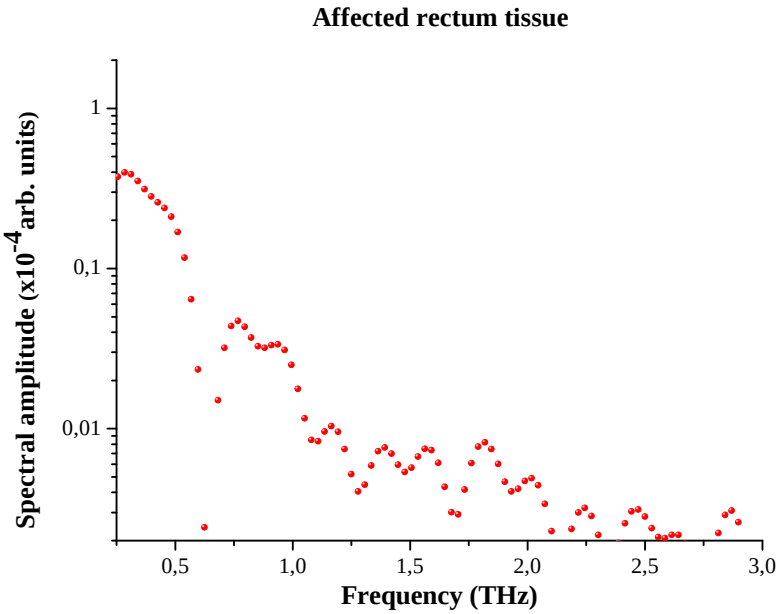

Figure 5.3: Spectral amplitude for affected rectum tissue.

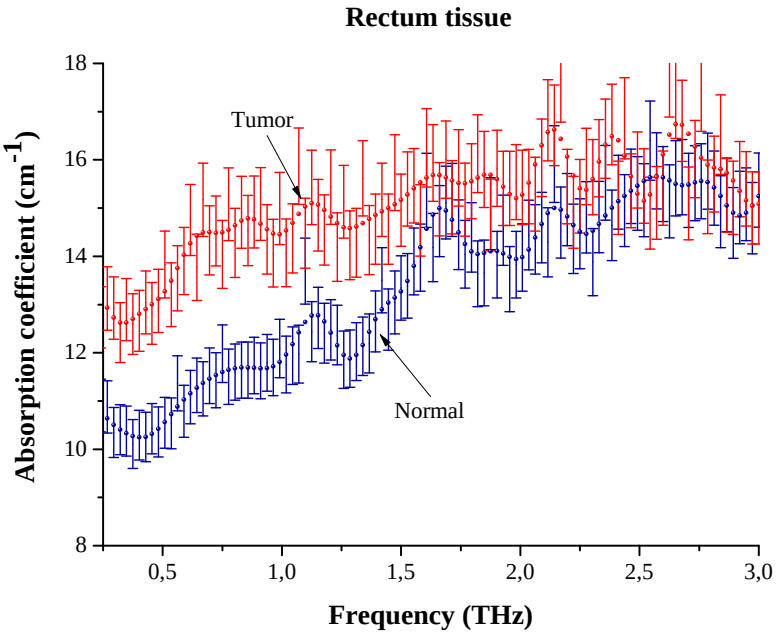

Figure 5.4: Calculated optical parameters of the normal and cancer affected rectum tissue: Absorption coefficient α.

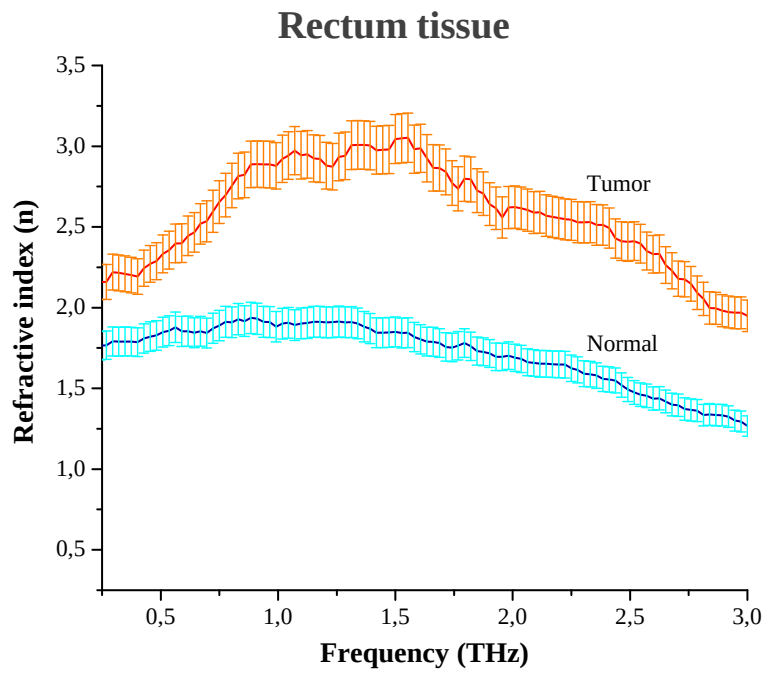

Figure 5.5: Calculated optical parameters of the normal and cancer affected rectum tissue: Refractive index n.

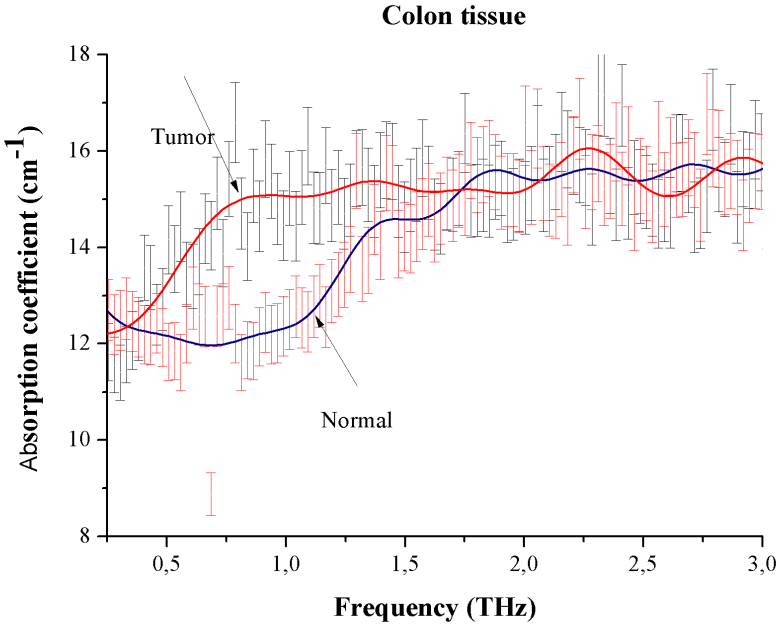

Figure 5.6: Calculated optical parameters of the normal and cancer affected colon tissue: Absorption coefficient α.

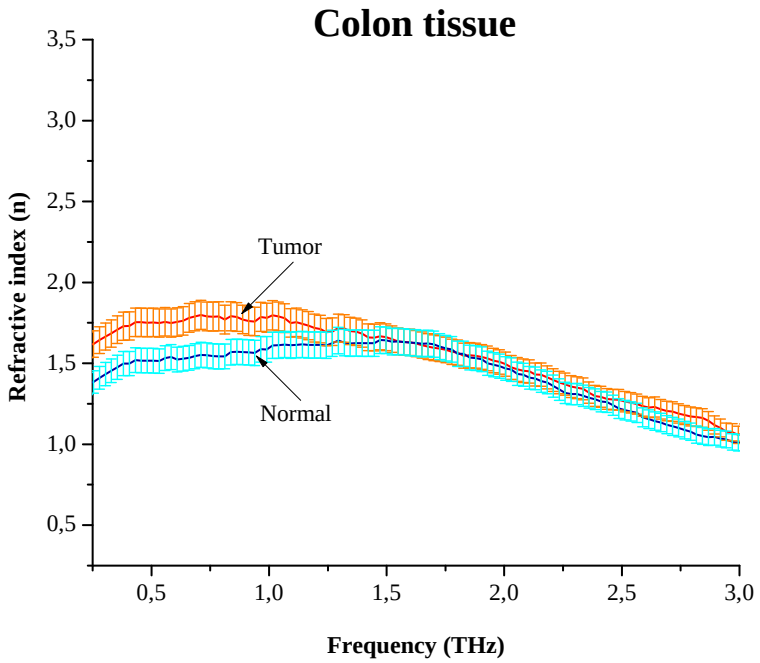

Figure 5.7: Calculated optical parameters of the normal and cancer affected colon tissue: Refractive index n.

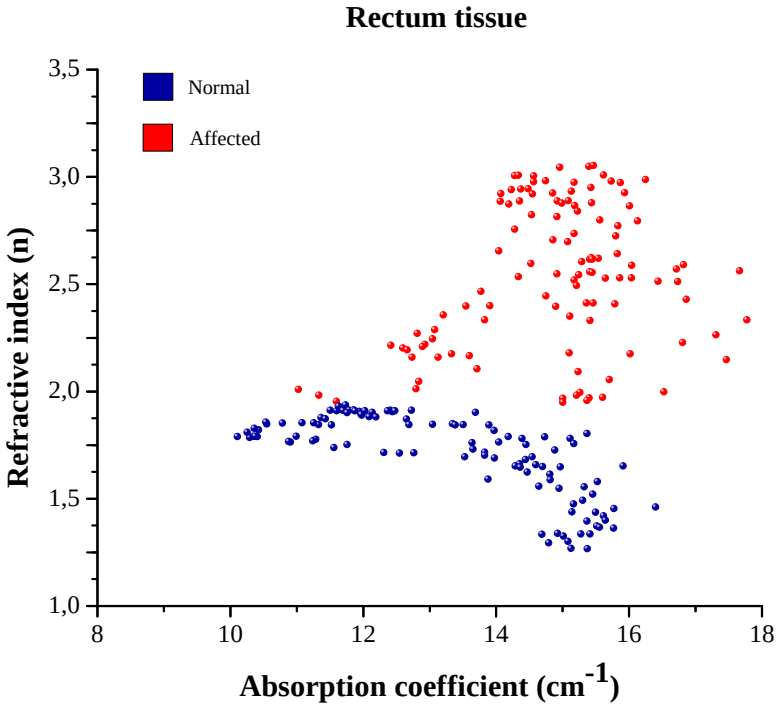

Figure 5.8: Refractive index as function of absorption coefficient of 2 different spots measured in a rectum tissue.

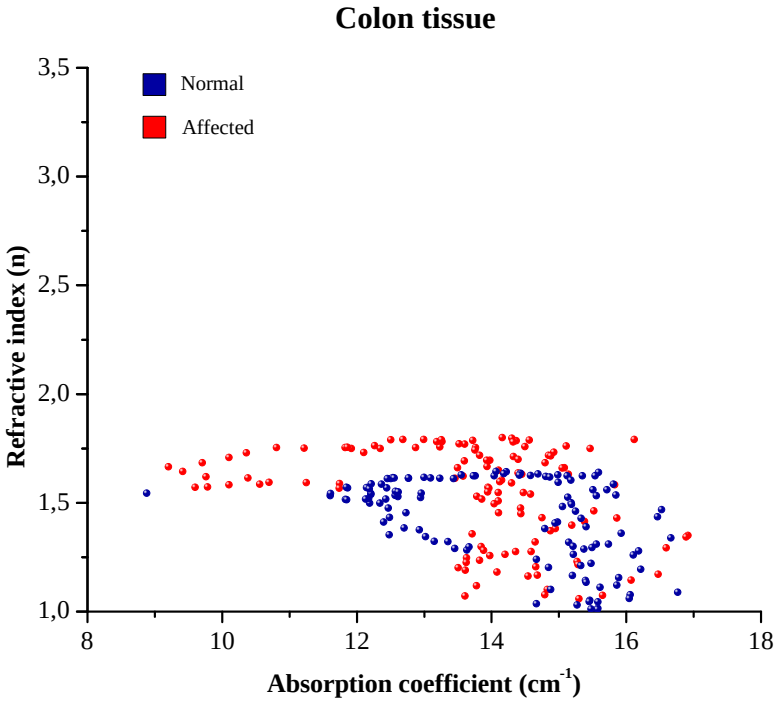

Figure 5.9: Refractive index as function of absorption coefficient of 2 different spots measured in a colon tissue.

(Figure 5.10). The following step comprised its transformation into frequency-domain through a Fourier transformation (Figure 3.6).

From this stage of data status, the frequency-dependent optical parameters, α and n, of the sample are then extracted (Figure 5.11 and Figure 5.12) using the equation 3.17 and equation 3.18. As with the colorectal tissues, a plot $\alpha(n)$ is here also presented in Figure 5.13. The plot corresponds to 3 measured spots of a paraffin-embedded colon tissue chosen as an example of evidence of discernible contrast between normal and affecte points. Figure 5.14 presents the calculated plots of the absolute indices of refraction for normal tissue samples in muscle (S_{4f} (λ), S_{4p} (λ)) and mucosa (S_{4f} (σ), S_{4p} (σ)) regions. The refractive index of the muscle (λ) is higher than the refractive index of the mucosa (σ). The refractive indices of formalin-fixed tissues are slightly higher than those of paraffin-embedded ones.

That difference is much smaller in the case of mucosa, where the indices of refraction for formalin fixed and paraffin embedded samples are very close. This can be explained by the higher percentage of hydration in the case of formalin fixed muscle [19, 60, 81] in comparison to mucosa, justifying a large difference between $S_{4f}(\lambda)$ and $S_{4p}(\lambda)$ and no difference between $S_{4f}(\sigma)$ and $S_{4p}(\sigma)$. In all cases, the refractive indices decrease with frequency.

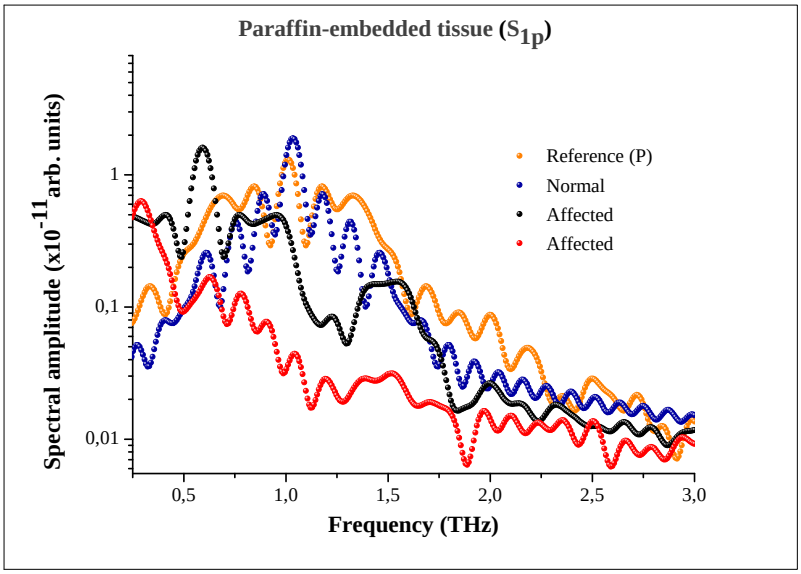

Figure 5.10: Reference and tissue time signals. Tissue signals correspond to 3 measured points of one of paraffin-embedded tissues (S_{1p}).

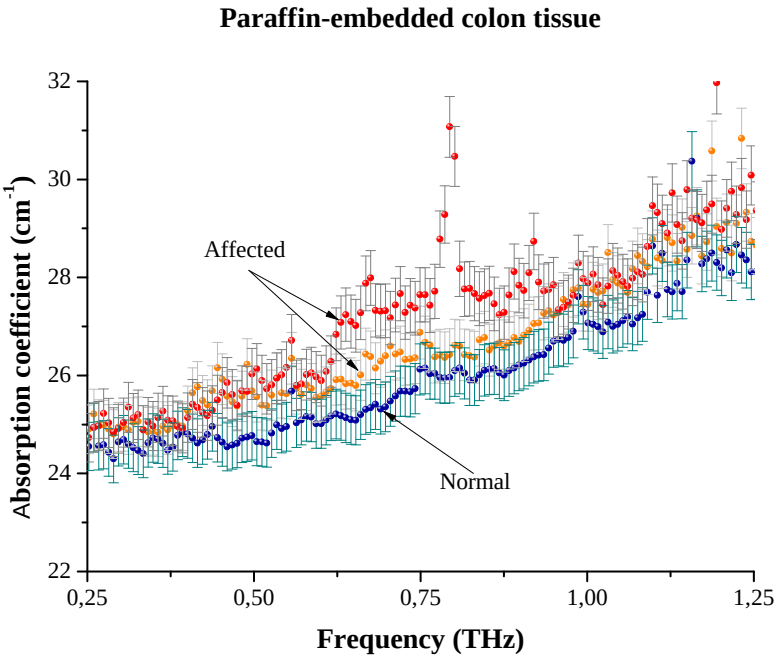

Figure 5.11: The absorption coefficients correspondent to time signals of the 3 measured points of the Paraffin-embedded colonic sample.

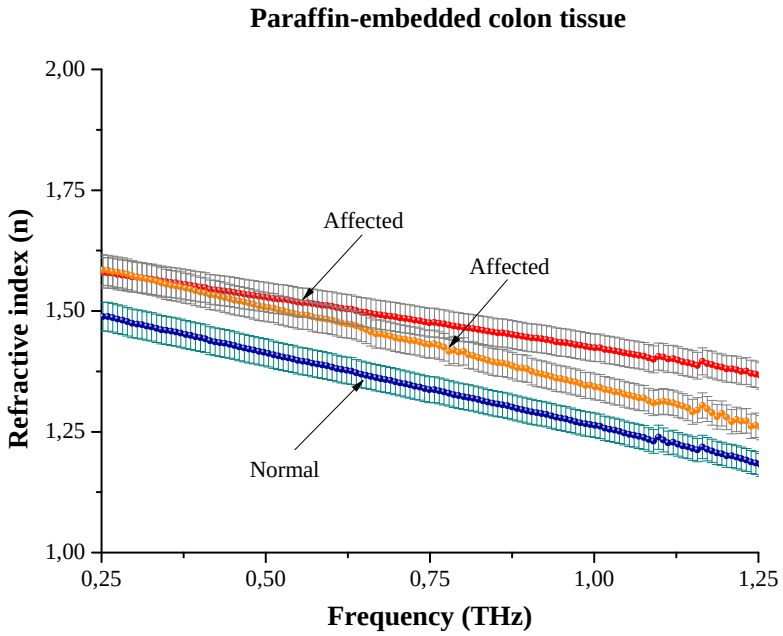

Figure 5.12: Refractive indices of the 3 measured points of the paraffin embedded colonic sample.

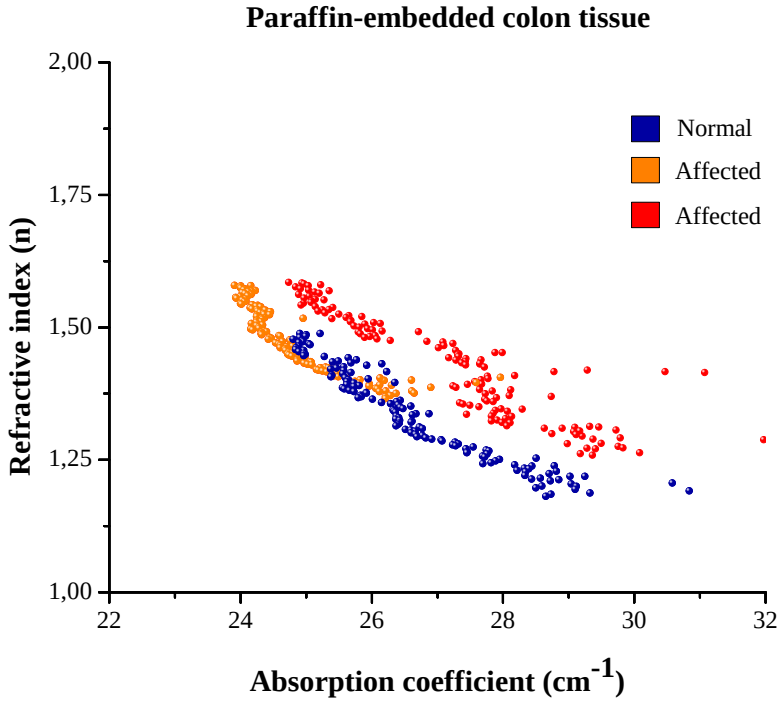

Figure 5.13: Refractive index as function of absorption coefficient of 3 different spots measured in a paraffin-embedded colon tissue.

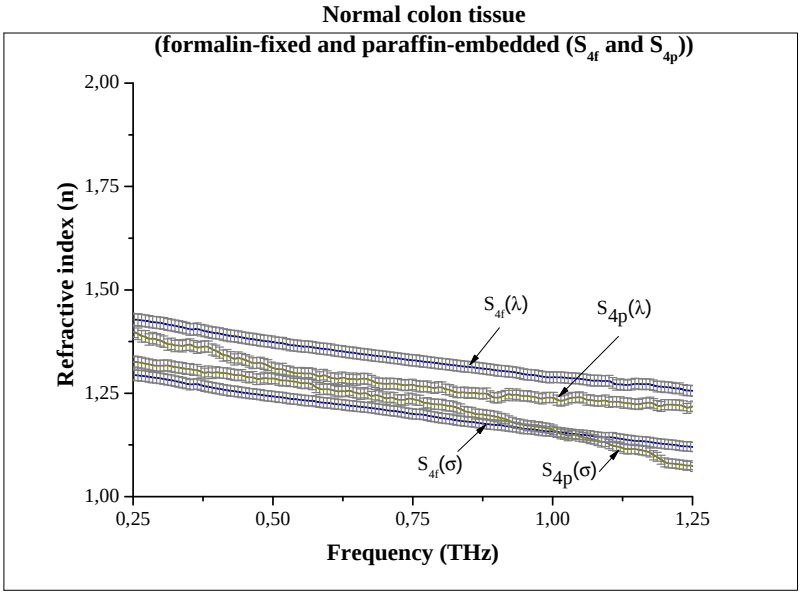

Figure 5.14: Refractive index plot for formalin fixed (f) and paraffin embedded (p) normal colon tissues: muscle (λ) and mucosa (σ).

Figures 5.15 and 5.16 present the calculated plots of the relative variation of the refractive indices $\Delta n_s/n_s = (n_{can} - n_{norm})/n_{norm}$ (where the subscripts, *can* refers to cancer and *norm* to normal) as function of frequency, for the sample groups: formalin fixed (S_{1f} and S_{2f}) in Figure 5.15, and paraffin-embedded (S_{1p} and S_{2p}) in Figure 5.16. Two cancer affected spots (α and β) and one normal spot (ν) in each sample have been measured by TTDTS. The values of the relative variation of the refractive indices are larger than zero in all samples. That means the refractive indices of the cancer affected spots in each sample are higher than that of normal spot in the same sample. It is reasonable to conclude that higher values of $\Delta n_s/n_s$ correspond to higher cancer development stage. Actually, since $\Delta n_s/n_s$ is larger in both, formalin fixed and paraffin embedded samples for the case of the spots α, as compared to the spots β, in both samples 1 and 2, we may conclude that spots α correspond to a more dense tumor. In the case of sample 1, that difference is stronger and therefore the difference in the cancer stage development should in principle be higher. The curves corresponding to the samples S_{3f} and S_{3p} are not shown, since they show similar behavior as the samples S_{2f} and S_{2p}, respectively.

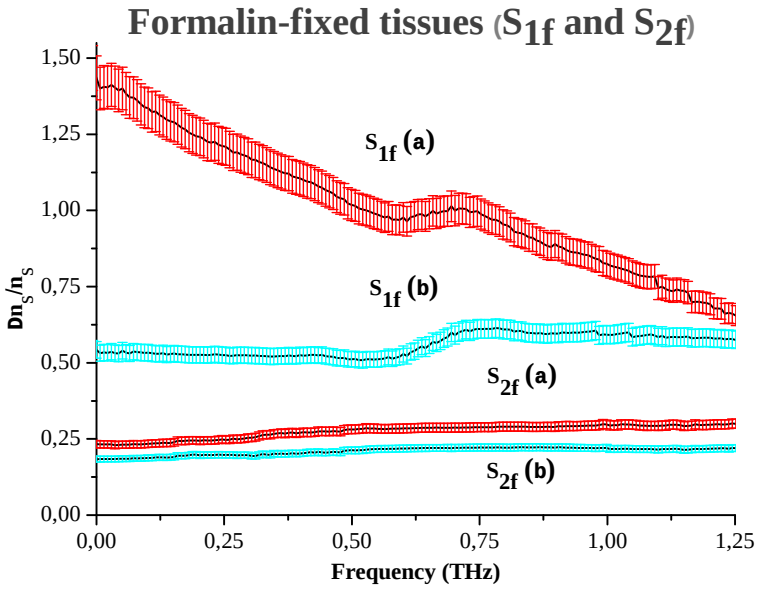

Figure 5.15: Spectra of the relative index variation for formalin-fixed samples, measured at the cancerous regions spots α and β.

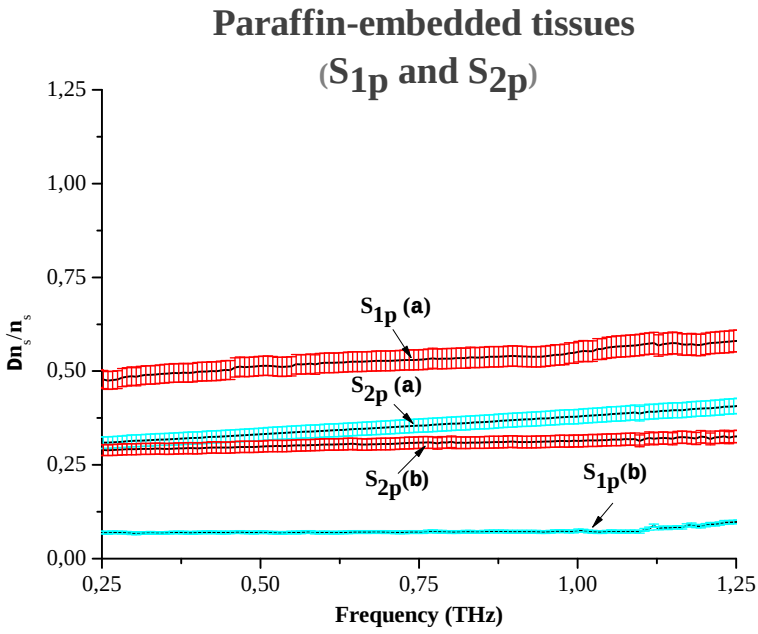

Figure 5.16: Spectra of the relative index variation for paraffin-embedded samples, measured at the cancerous regions spots α and β.

5.3 Continuous Wave THz Imaging (CWTI) on Colonic and Rectal Tissues

The absorption of biological media in the THz frequency range is caused by low-frequency weak inter- and intramolecular vibration and vibrational modes such as hydrogen bonds. Scanning a sample with a THz beam imaging by an appropriate technique, such as CWTI, it is possible to get 2D absorption maps of the sample.

The samples used for CWTI have been chosen among those used for TDTS measurements, and the measurements have been made at the same environment conditions. The samples have been mounted on a computer-controlled $X-Y$ translation stage, in order to be scanned, point by point, with the focused THz beam, using the spectrometer set-ups of Figure 4.20 and Figure 4.22. By scanning the selected areas of the samples, shown in Figures 5.17 and 5.18, with a continuous wave (CW) THz radiation, it was possible to get the absorption coefficient distributions. The imaging time for the entire window area of was less than 20 minutes. Figure 5.17 shows the 2-D absorption images for colon and rectum samples for a fixed wavelength $\lambda = 163\mu$m, or frequency $\nu = 1.84$THz, which corresponds to the beginning of water absorption band whose absorption peak is known to be centered at 5.4THz [20]. Following the imaging of the first set of samples, we proceeded with the second set.

The images of the absorption coefficient distributions of two samples, S_{1f} and S_{2p}, have been obtained with this technique, by scanning the areas of the samples with the focus spot of continuous wave THz radiation at a fixed wavelength of $\lambda = 393\mu$m or frequency $\nu = 0.76$THz.

Figure 5.18 shows the photographs of two samples and the respective absorption images. It can be observed that the cancer areas, as identified by histopathological analysis, show higher absorption coefficient (red color) than the normal areas.

The spots α and β that have been studied by TTDTS in the previous section present higher absorption coefficients, and the spot ν, lower absorption coefficient. The reddish areas in the THz images of Figure 5.18 correlate well with the histopathologic findings. A normal border effect can be observed in blue-green color at the sample borders. The orange area in S_{1f} of Figure 5.18 (c) corresponds to normal mucosa and the green area to normal muscle. The difference in colors is due to the difference of the absorption coefficient which is higher for the mucosa. Both higher refractive indices and absorption coefficients seem to be a signal of the presence of cancer in the studied samples, although their increasing with cancer density cannot be generally taken from our data. In the case of index of refraction, our results are apparently conclusive in that respect, but this is not so in the case of the absorption coefficients, as shown in

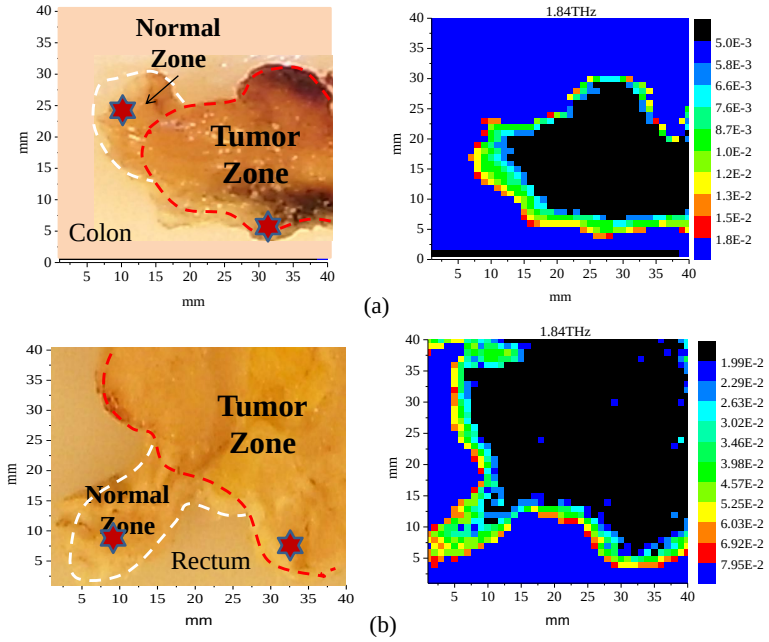

Figure 5.17: Sample images with visible light (left) and the corresponding images with THz continuous wave at $\lambda = 163\mu$m ($\nu = 1.84TH$) (right). The samples contain affected and healthy zones: (a) colon tissue, and (b) rectum tissue. The black areas, which correspond to stronger absorption, indicate the presence of cancer. The stars in the images represent the measured points in the TDTS experiments.

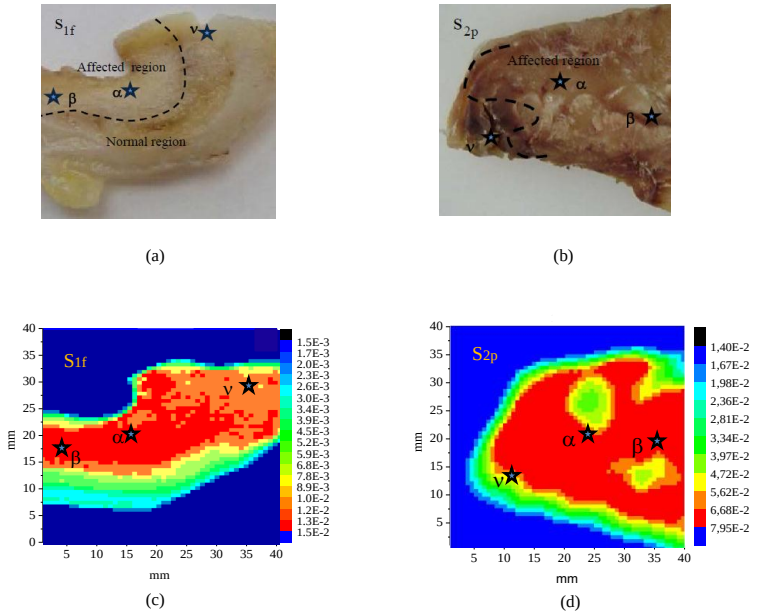

Figure 5.18: Samples that have been imaged by CWTI at the wavelength $\lambda = 393\mu$m ($\nu = 0.76$THz): (a) and (b); CWTI images of the samples: (c) and (d). The reddish areas, corresponding to stronger absorption, correlate quite well with the cancer affect regions determined by histological observation.

the CWTI image of Figure 5.18 (c) where spot α should present a more reddish color than spot β. More detailed studies of the correlation between refractive indices and absorption coefficients in cancer affected tissues are, therefore, needed for clarification.

5.3.1 Summary

In this chapter results of all of the experiments realized toward the aims of the present work are presented, starting with those of TDTS on colorectal and colon. Time waveforms corresponding to the reference medium and normal and affected points of differents tissues are shown. Plots of absorption coefficient and refractive index of the tissues obtained from the time signals data are presented. The obtained TDTS data are analyzed using the analytical formulations discussed in chapter 3 and the optical parameters (α and n) are calculated and plotted. The spectra of the two parameters show a noticeable contrast between health and diseased tissues. For the sake of degree of confidence on the calculated α and n values, error bars have been added with 95% of confidence. Using CWTI setup, selected samples, taken from those previously measured in TDTS, have been imaged (at a fixed frequency of 1.84 THz for colorectal tissues, and 0.76 THz for the only colonic tissues) in order to validate the TDTS findings. All this information helped us to better understand, visualize and confirm the existence of hidden contrast factors other than water, a fact that we have been looking for as the

main objective of the present work.

Chapter 6

Conclusions and Further Work

This chapter provides a summary of the study carried out in this thesis work that was presented in the previous chapters, and provides suggestions for future research work. It presents some arguments that indicate that the THz techniques have the potential to be a superior complement to the techniques for cancer screening in use nowadays.

In the work of several groups [20,31,56,81] with freshly excised tissues, the differences on the refractive indices and absorption coefficients in cancer affected samples have been mainly attributed to the presence of a higher concentration of water [59, 65, 66]. However, other possible factors have been pointed out by authors of numerous studies envolving formalin-fixed, dehydrated and paraffin-embedded tissues [82, 83]. Thus, additional studies have been suggested toward the determination of the other contrast-contributing factors, in order effective THz techniques and methods to be well established.

Some cancer contrast factors are already known such as: (1) the increase in the vasculature due to the release of growth factors that also lead to rapid cell division and higher cell densities [19]; (2) the conditions within the tumor microenvironment, that differ considerably from those of normal tissue [5–9], for instance, low oxygen levels (hypoxia). Angiogenesis is one of the main responses of the tumor to overcome the hypoxia; (3) the rapid and uncontrolled cell division that leads to an increased cell density and/or to the presence of certain proteins, and (4) tryptophan and other amino acids play a crucial role in the proliferation of tumor cells [84], and their influence in the contrast is still in evaluation [63]. There is a dependence of the tumor development upon the nutrients received through the blood. Tumor cells, like all other cells need amino acids for their proliferation [85–87]. The majority of the tumor cells have the capability to gather amino acids more than normal cells can.

To summarize, we have checked the relevance of other factors, besides the water, for THz cancer detection. We have studied two sets of tissue samples: one set is fixed in

formalin, where water exists, and the other set is dehydrated and embedded in paraffin. Both types of samples have been taken from the same bio-structural typology and the measured spots belong to the same regions. Using TTDTS and CWTI, we have shown that cancer affected regions of all samples show higher refractive indices and absorption coefficients that distinguish them from the normal ones. The present study reinforces the feasibility of these THz techniques for colon cancer detection. It also demonstrates the higher percentage of water in cancerous tissues is not the only factor contributing to the contrast of the observed refractive index and the absorption coefficient.

6.1 Future research work

The present status of the THz technique's capability in real biomedical application is in its dawn infancy, limited only for in-vivo skin and ex-vivo tissue diagnostic screening. Up till now the contrast mechanisms and the exact contrast factors are not clearly understood. The present study aimed to confirm the existence of other factors beside the water. Water is already known as a strong contrast factor as by refractive indices as well as by the absorption coefficients spectra. At the present stage of development of THz techniques, imaging and spectroscopy in transmission geometry will likely be difficult to be applied in in-vivo screenings. Reflection geometry is the only promising method for in-vivo skin and internal organs' diagnose, and therefore, for all types of THz diagnosis techniques more studies are still needed.

There are some research tasks that have to be done in further research work: (1) how to overcome the limitation of THz in penetration depth; (2) the development of endoscopic THz capabilities by improving the THz reflection modality; it could be implemented by the use of incorporated THz-chips in fiber optics guides for internal organs and gastrointestinal (GI) tract cancer screening; (3) the characteristics of the THz pulse shape changes drastically with the alteration of the positions of any of optical components of the quasi-optical THz set-ups; it would be worth modeling the THz pulse shape and comparing it with the real THz pulse-shape with the effects of each of THz-system's optical components included in its final pulse-shape and frequency spectrum; (4) improvement of the methods for filtering by signal processing of Fabry-Pèrot effect and water vapor noise removal, also would be a recommendable further task. We highlight that, in next THz works, we plan to address our experiments to reflection imaging and spectroscopy in order to approach its application in real world as for skin as well as for internal organs.

Appendix A

Tables

Table A.1: Techniques for the Screening of Colon and Rectum Cancer

BLOOD TESTS	**Complete Blood Count**	Anemia assessment (some people with colon or rectum cancer become anemic because of prolonged bleeding from the tumor.
	Tumor Markers	Substances such as carcinoembryonic antigen and CA 19-9 may be generated by colon or rectum cells and released into the blood-stream, the technique serves to show how well the treatment is going, in people who already have been diagnosed with colon or rectum cancer and are in ongoing treatment.
TESTS FOR COLON AND RECTUM POLYPS OR CANCER	**Biopsy**	The removal of a small piece of tissue once a suspected colon or rectum cancer is found by any diagnostic test method. It a time consuming and painful medical procedure.The removal of a small piece of tissue once a suspected colon or rectum cancer is found by any diagnostic test method. It a time consuming and painful medical procedure.
	Lab Test of Samples	The colonoscopy or surgery biopsied samples are sent to histopathological examination

Table A.2: Imaging Techniques for Colon and Rectum Cancer

Computed tomography (CT or CAT)	X-ray test that produces cross-sectional images with a considerable level of spatial resolution.
CT-guided needle biopsy	The introduction through the skin of a needle to the suspected tissue mass inner the body.
Ultrasound	Endorectal and intra-operative ultrasound
Magnetic resonance imaging (MRI)	Uses radio-waves instead of X-rays and provides well-resolved images of soft tissue.
Chest X-rays	Performed in people who already have been diagnosed with colon or rectum cancer to verify whether the cancer has spread to the lungs.
Positron emission tomography (PET)	Is a technique that produces a map of the body radioactivity, despite not spatially well-resolved. Fluorodeoxyglucose (FDG), a radioactive sugar is injected into the bloodstream and then, cancer cells absorb large amounts of the FDG and, with an aid body radioactivity, despite not spatially well-resolved. Fluorodeoxyglucose (FDG), a radioactive sugar is injected into the bloodstream and then, cancer cells absorb large amounts of the FDG and, with an aid of a camera, a picture (or a map) of areas of radioactivity is generated.
Angiography	An X-rays technique for blood vessels assessment

Table A.3: Current Novel Methods in Colonoscopy

Technique	Advantage	Desadvantage
Chromo-endoscopy	Cost effective, simple adenomas and dysplasia detection improvement	Operator dependent and do not determine polyp histology
Confocal Fluorescence Microscopy	Improved spatial resolution, detects superficial tumor invasion, gives 3D images and accuracy comparable with that of histologic examination	Systemic fluorescence agents required, not suitable for the screening of large mucosal areas.
Fluorescence Spectroscopy	May distinguish normal from dysplastic tissues, large areas of mucosal screening in real time, easily identifies flat adenomas	Problems on patients with bowel inflammation, mucosal folds artifact
Light-Scattering Spectroscopy	Strong signal, employs white light (cost effective), distinguishes normal from dysplastic tissue	Poor reproducibility of the signal, small sampled tissue.
Optical Coherence Tomography (OCT)	Highly improved spatial resolution and superficial tumor invasion identifiable	Very costly facility and subjectivity in image interpretation
Raman Spectroscopy	Objective, molecular specific technique, can differentiate wide range of pathologies	Time consuming, small volume of sampled tissue

Bibliography

[1] D. Leonel, G. Frédéric, R. Jean-François, and J.-K. Coutaz, "Analytical modeling and optimization of terahertz time-domain spectroscopy experiments using photoswitches as antennas," *IEEE Journal of Selected Topics of Quantum Electronics*, vol. 7, pp. 605–623, 2001.

[2] T.-A. Liu, "Ultrabroadband terahertz field detection by photoconductive antennas based on multi-energy arsenic-ion-implanted gaas and semi-insulating gaas," *Applied Physics Letters*, vol. 83(7), pp. 1322–1324, 2003.

[3] T. Loffler, K. Markus, and M. Thomson, "Comparative performance of terahertz emitters in amplifier-laser-based systems," *Semiconductor Science Technology*, vol. 20 (7), pp. S134–S141, 2005.

[4] D. R. Grischkowisk and D. Mittleman, *Sensing with THz Radiation*. Springer, 2002.

[5] P. Vaupel, "The role of hypoxia-induced factors in tumor progression," *The Oncologist*, vol. 9 (Supl. 5), pp. 10–17, 2004.

[6] P. Vaupel, "Tumor microenvironmental physiology and its implications for radiation oncology," *Seminars in Radiation Oncology*, vol. 14 (3), pp. 198–206, 2004.

[7] R. J. Gillies, N. Ragunhand, G. Karczmar, and Z. Bhujwalla, "Mri of the tumor microenvironment," *Journal of Magnetic Resonance Imaging*, vol. 16, pp. 430–450, 2002.

[8] D. Fucumura and K. R. Jain, "Tumor microenvironment abnormalities: Causes, consequences, and strategies to normalize," *Journal of Cellular Biochemistry*, vol. 101, pp. 937–949, 2007.

[9] T. Reynolds, S. Rockwell, and P. M. Glazer, "Genetic instability induced by the tumor microenvironment," *Cancer Research*, vol. 56, pp. 5754–5757, 1996.

[10] L. J. Kleinsmith, D. Kerrigan, J. Kelly, and B. Hollen, "Understanding cancer and related topics, understanding angiogenesis," tech. rep., National Cancer Institute, 2006.

[11] NCI, *The Cancer of the Colon and Rectum*. NIH, 2006.

[12] C. H. Lee, *Microwave Photonics*. CRC Press, 2006.

[13] T. Hori and Hiromot, "Characteristis of a far-infrared molecular laser optically pumped by a high-power co2 laser," *International Journal Infrared Milli Waves*, vol. 13 (4), pp. 1–14, 1992.

[14] D. H. Auston, "Picosecond optoelectronic switching and gating in silicon," *Applied Physics Letters*, vol. 26, pp. 101–103, 1975.

[15] D. Austin and K. C. C. time-domain far-infrared spectroscopy, "Coherent time-domain far-infrared spectroscopy," *Journalof Optical Society of America B 2*, vol. 2 (4), p. 606, 1985.

[16] D. Austin and M. Nuss, "Electromagnetic generation and detection of femtosecond electrical transients," *IEEE Journal of Quantum Electronics*, vol. 24 (2), pp. 184–197, 1988.

[17] M. F. Kimmit, "Restrahlen to t-rays - 100 years of terahertz radiation," *Journal od Biological Physics*, vol. 29, pp. 75–85, 2003.

[18] R. M. Woodward, B. E. Cole, V. P. Wallace, R. J. P. D. D. Arnone, E. H. Linfield, and M. Pepper, "Terahertz pulse imaging in reflection geometry of human skin cancer and skin tissue," *Physics in Medicine and Biology*, vol. 47, pp. 3853–3863, 2002.

[19] E. Pickwell, B. Cole, A. J. FitzgeraldJ, M. Pepper, and V. P.Wallace, "In vivo study of human skin using pulsed terahertz radiation," *Physics in Medicine and Biology 49 1595-1607*, vol. 49, pp. 1595–1607, 2004.

[20] A. J. Fitzgerald, V. P. Wallace, M. Jimenez-Linan, L. Bobrow, R. J. Pye, A. D. Purushotham, and D. D. Arnone, "Terahertz pulsed imaging of human breast tumors," *Radiology*, vol. 239 (2), pp. 533–540, 2006.

[21] V. P. Wallace, "Terahertz imaging detects cancerous tissue," *SPIE Newsroom*, vol. 10.1117/2.1200812.1406, 2008.

[22] S. Y. Huang, Y. Wang, D. Yeung, A. T. Ahuja, Y. T. Zhang, and E. P. MacPherson, "Tissue characterization using terahertz pulsed imaging in reflection geometry," *Physics in Medicine and Biology*, vol. 54, pp. 149–160, 2009.

[23] V. P. Wallace, A. J. Fitzgerald, E. P. MacPherson, R. J. P. P. F. Taday, N. Flanagan, and T. Ha, "Terahertz pulsed spectroscopy of human basal cell carcinoma," *Applied Spectroscopy*, vol. 60 (10), pp. 1127–1133, 2006.

[24] R. M. Woodward, V. P. Wallace, D. Arnone, E. H. Linfield, and M.Pepper, "Terahertz pulse imaging of skin cancer with time and frequency domain," *Journal of Biiological Physics*, vol. 29, pp. 257–261, 2003.

[25] E. P. MacPherson, V. P. Wallace, A. J. Fitzgerald, B. E. Cole, R. J. Pye, and T. Ha, "Simulating the response of terahertz radiation to human skin using ex-vivo spectroscopy measurements," *Journal of Biomedical Optics*, vol. 10, p. 064021, 2005.

[26] P. H. Bolivar, M. Brucherseifer, M. Nagel, H. Curz, A. Bosserhoff, and R. Buttnere, "Label-free probing of genes by time-domain terahertz sensing," *Physics in Medicine and Biology*, vol. 47, pp. 3815–3821, 2002.

[27] M.-F. Penet, G. K. Glunde, A. J. Michel, A. P. Pathak, and Z. M. Bhujwalla, "Molecular and functional mri of the tumor microenvironment," *The Journal of Nuclear Medicine*, vol. 49 (5), pp. 687–690, 2008.

[28] G. Gallerano, "Ove of terahertz radiation sources," in *FEL Conference*, 2004.

[29] D. Austin, K. P.Cheung, and P. R. S. P. photoconducting Heratzian dipoles, "Picosecond photoconducting heratzian dipoles," *Applied Physics Letters Phys. Lett. 45, 284-286*, vol. 45, 284-286, pp. 284–286, 1984.

[30] K. Sakai and M. Tani, "Introduction to terahertz pulses," *Topics of Applied Phsysics*, vol. 97, pp. 1–31, 2005.

[31] J. Zhang, Y. Hong, S. Braunstein, and K. Shore, "Terahertz pulse generation and detection with lt-gaas photoconductive antenna," *IEEE Proc. Optoelectronics*, vol. 151, pp. 98–101, 2004.

[32] D. Grischkowsky, S. Keiding, V. V. Exter, and C. Fattinger, "Farinfrared time-domain spectroscopy with terahertz beams of dielectrics and semiconductors," *Journal of Optical Society of America B*, vol. 7 (10), pp. 2006–2015, 1990.

[33] G. Zhao, R. N. Schouten, N. van der Valk, W. T. Wenckebach, and P. C. M. Plankena, "Design and performance of a thz emission and detection setup based on a semi-insulating gaas emitter," *Review of Scientific Instruments*, vol. 74 (4), pp. 1715–1719, 2002.

[34] M. Tani, S. Kana, M. Nakajima, M. Iida, and K. Sakai, "Generation and detection of ultrabroadband terahertz radiation with photoconductive antennas," in *0-7803-7423-1/02/ 02002 IEEE.*, 2002.

[35] T. Masahiko, M. Herrmann, and K. Sakai, "Generation and detection of terahertz pulsed radiation with photoconductive antennas and its application to imaging," *Meas. Sci. Technol*, vol. 13, pp. 1739–1745, 2002.

[36] S. M. Sze and K. K. NG, *Physics of Semiconductor Physics.* Willey-Interscience, 2006.

[37] Zhang, *Introduction to THz Wave Photonics:.* Springer, 2009.

[38] B. B. Hu and M. C. Nuss, "Imaging with terahertz waves," *Optics Letters*, vol. 20 Issue 16, pp. 1716–19, 1995.

[39] H. Zhang, J. K. Wahlstrand, S. B. Choi, and S. T. Cundiff, "Contactless photoconductive terahertz generation," *Optics Letters*, vol. 36 (2), p. 225, 2011.

[40] R. A. Cheville, *Terahertz Spectroscopy: Principles and Applications.* CRC Press, 2007.

[41] E. R. Brown, O. B. Mcmahon, and K. Parker, "Photonic-crystal antenna substrates," *The Lincoln Laboratory Journal*, vol. 11 (2), pp. 159–173, 1994.

[42] S. Sengupta, I. Wilke, and P. S. Dutta, "Ultrafast carrier mobilities in high-resistivity iron-doped ga0.69in0.31as photoconducting antennas," *Applied Physics Letters*, vol. 95, pp. 1–3, 2009.

[43] J.-P. Colinge and C. A. Colinge, *Physics of Semiconductor Devices.* Springer, 2005.

[44] S. Kasap, *A illustrated Dictionary of Optoelectronics and Photonics: Important Terms and Effects.* Alan Greenspan, 1999.

[45] L. T-An, M. T. M, and P. C-Ling, "Thz radiation emission properties of arsenic-ion-implanted gaas and semi-insulating gaas based photoconductive antennas," *Journal of Applied Physics*, vol. 93 (5), 2996-3000, pp. 2996–3000, 2003.

[46] S. B. S. P. S. B. Casalbuoni S, Schlarb H and W. A, "Numerical studies on electro-optic sampling of relativistic electron bunches," tech. rep., Tesla Report, 2005.

[47] A. Yariv, *Quantum Electronics.* Willey, 1989.

[48] E. I. Ackerman, J. Capmany, and C. H. C. et al, *Microwave Photonics: Devices and Applications.* Wiley, 2008.

[49] A. Leitenstorfer, S. Hunsche, J. Shah, and M. Nuss, "Detectors and sources for ultrabradband electro-optic sampling: Experiment and theory," *Applied Physics Letters*, vol. 74 (11), 1999.

[50] M. Tang, H. Minamide, Y. Wang, T. Notake, S. Ohno, and H. Ito, "Tunable terahertz-wave generation from dast crystal pumped by a monolithic dual-wavelength fiber laser," *Optics Express*, vol. 19(2), p. 779, 2011.

[51] K. Miyamoto, S. Ohno, M. Fujiwara, H. Minamide, H. Hashimoto, and H. Ito, "Optimized terahertz-wave generation using bna-dfg," *Optics Express*, vol. 17(17), p. 14832, 2009.

[52] M. Bass, "Optical rectification," *Physics Review Letters*, vol. 9, pp. 446–448, 1962.

[53] C. Winnewisser, P. U. Jepsen, M. Schall, and V. Schya, "Electro-optic detection of thz in litao3, linbo3 and znte," *Applied Physics Letters*, vol. 70, pp. 3069–3071, 1997.

[54] G. Gallot, J. Zhang, R. W. McGowan, T.-I. Jeon, and D. Grischkowsky, "Measurement of the thz absorption and dispersion of znte and their relevance to the eo detection of thz radiation," *Applied Physics Letters*, vol. 74 (23), pp. 3450–3452, 1999.

[55] J. Rudd and D. Mittleman, "Influence of substrate-lens design in terahertz time-domain spectroscopy," *Journal of Optical Society of America B*, vol. 19(2), pp. 319–329, 2002.

[56] A. Nahata, A. S. Weling, and T. F. Heinz, "Wideband coherent terahertz spectroscopy using optical rectification and electro-optic sampling," *Applied Physics Letters*, vol. 69 (16), pp. 2321–2323, 1996.

[57] W. Withayachumnankul, "Direct fabry-pérot effect removal," *Fluctuation Noise Letters*, vol. 6 (2), pp. 227–2339, 2006.

[58] G. M. Png, J. W. Choi, B. Ng, S. P. Mickan, and D. Abbott, "The impact of hydration changes in fresh bio-tissue on thz spectroscopic measurements," *Physics in Medicine and Biolology*, vol. 53, pp. 3501–3517, 2008.

[59] M. He, A. K. Azad, S. Ye, and W. Zhang, "Far-infrared signature of animal tissues characterized by terahertz time-domain spectroscopy," *Optics Communications*, vol. 259, pp. 389–392, 2006.

[60] M. Bruehlmeier, U. Roelcke, P. Blauenstein, J. Missimer, P. Schubiger, J. Locher, R. Pellikka, and S. M. Ametamey, "Measurement of the extracellular space in

brain tumors using 76br-bromide and pet," *Journal of Nuclear Medicine*, vol. 44, pp. 1210–1218, 2003.

[61] I.-C. Kiricuta and V. Simplaceanu, "Tissue water content and nuclear magnetic resonance in normal and tumor tissues," *Cancer Research*, vol. 35, pp. 1164–1167, 1975.

[62] J. E. Downing, W. M. Christopherson, and W. Broghamer, "Nuclear water content during carcinogenesis," *National Institut of Health*, pp. 1176–1180, 1961.

[63] O. P. Cherkasova, M. M. Nazarov, and A. P. Shkurinov, "Terahertz spectroscopy of biological molecules," *Radiophysics and Quantum Electronics*, vol. 52 (7), pp. 518–523, 2009.

[64] A. Pierangelo, A. Benali, M.-R. Antonelli, T. Novikova, P. Validire, B. Gayet, and A. D. Martino, "Ex-vivo characterization of human colon cancer by mueller polarimetric imaging," *Optics Express*, vol. 19 (2), pp. 1582–1593, 2011.

[65] G. I. Mclntyre, "Cell hydration as the primary factor in carcinogenesis: Unifying concept," *Medical hypothesis*, vol. 66, pp. 518–526, 2006.

[66] G. I. Mcltyre, "Increased cell hydration promotes both tumor growth and metastasis: A biochemical mechanism consistent with genetic signatures," *Medical hypothesis*, vol. 69, pp. 1127–1130, 2007.

[67] M. K. Gupta and R.-Y. Qin, "Mechanism and its regulation of tumor induced angiogenesis world j. of gastroenterology, 1144-1155," *World Journal of Gastroenterology*, pp. 1144–1155, 2003.

[68] J. Macutkevic, R. Grigalaitis, R. Adomavicius, A. Krotkus, J. Banys, G. Valusis, K. Bormanis, and A. Sternberg, "Broadband dielectric spectroscopy of ferroelectric phase transitions in pbsc1/3nb2/303 ordered ceramics," *Ferroelectrics*, vol. 369, pp. 185–189, 2008.

[69] H. Ying, P. Huang, L. Guo, Wang, and C. Zhang, "Terahertz spectroscopic investigations of explosives," *Physics Letters*, vol. 359, pp. 728–732, 2006.

[70] J. Xu, T. Yuan, S. Mickan, and X.-C. Zhang, "Limit of spectral resolution in terahertz time-domain spectroscopy," *Chines Physics Letters*, vol. 20 (8), pp. 1266–1268, 2003.

[71] P. U. Jepsen and B. M. Fischer, "Dynamic range in terahertz time-domain transmission and reflection spectroscopy," *Optics Letters*, vol. 30 (1), pp. 29–31, 2005.

[72] J. A. Kiernan, "Formaldehyde, formalin, paraformaldehyde and glutaraldehyde: What they are and what they do," *Microscopy today*, vol. 00-1, pp. 8–12, 2000.

[73] Y. Sun, M. Fischer, and E. P. MacPherson, "Effects of formaling fixing on the thz properties of biological tissues," *Journal of Biological Optics*, vol. 14 (6), pp. 06401–17, 2009.

[74] T. Boenisch, A. J. Farmilo, R. H. Stead, and at al., eds., *Immunochemical Staining Methods Handbook*. Dako Corporation, 3rd ed., 2001.

[75] D. W. Cromey, "Formaldehyde fixatives," *Cellular Imaging Core Newsletter*, pp. 1–3, 2004.

[76] R. Piesiewicz, C. Jansen, S. Wietzke, D. Mittliman, M. Koch, and T. Kurner, "Properties of building and plastic materials in the thz range," *International Journal Infrared Milli Waves*, pp. 1–9, 2007.

[77] G. W. Chantry, *Long-wave optics: The science and technology of infrared and near-millimetre waves*. Academic Press, 1984.

[78] E. R. Mueller, "Optically-pumped thz laser techniology," tech. rep., Coherent.

[79] I. Kasalynas, D. Seliuta, R. Simniskis, V. Tamosiunas, K. Kohler, and G. Valusis, "Terahertz imaging with bow-tie ingaas-based diode with broken symetry," *Electonics Letters*, vol. 45, p. 833, 2009.

[80] D. Seliuta, I. Kasalynas, V. Tamosiunas, S. Balakauskas, Z. Martunas, S. Asmontas, G. Valusis, A. Lisauskas, H. G.Roskos, and K. Kohler, "Silicon lens-coupled bow-tie ingaas broadband terahertz sensor operating at room temperature," *Electonics Letters*, vol. 42 (14), pp. 825–827, 2006.

[81] P. C. Ashworth, E. P. MacPherson, E. Provenzano, Pinder, S. E. Pinder, and V. P. Wallace, "Terahertz pulsed spectroscopy of freshly excised human breast cancer," *Optics Express*, vol. 17 (15), pp. 12444–12453, 2009.

[82] T. Loffler, K. J. Siebert, S. Czasch, T. Bauer, and H. Roskos, "Visualization and classification in biomedical terahertz pulsed imaging.," *Physics in Medicine and Biology*, vol. 47, pp. 3847–3852, 2002.

[83] P. Knobloch, Schildknechtc, T. Cleine-Ostmann, M. Koch, and S. Hoffmann, "Medical thz imaging: an investigation of histopathological samples," *Physics in Medicine and Biology*, vol. 47, pp. 3875–3884, 2002.

[84] A. Tankiewics, D. Dziemianczyk, P. Buczko, I. J. Szarmach, S. Z.Grabowska, and D. Pawlak, "Tryptophan and its metabolites in patients with oral squamous cell carcinoma," *Advances in Medical Sciences*, vol. 51, pp. 221–224, 2006.

[85] J. K. Isselbacher, "Sugar and amino acids transport by cells in culture-differences between normal and malignant cells," *New English Journal of Medicine*, vol. 286, pp. 929–933, 1972.

[86] L. A. Peneto, P. Oliveira-Silva, E. M. C. Gonzales, R. Maciel, P. B. Jurgilas, A. Melibeu, P. C-Costa, and C. A. Serfaty, "Nutritional tryptophan restriction impairs plasticity of retinotectal axons during the critical period," *Experimental Neurology*, vol. 217, pp. 108–115, 2009.

[87] B. Yu, F. Zeng, Y. Y. Q. Xing, A. Chechin, X. Xin, I. Zeylikovich, and R. R. Alfano, "Torsional vibrational modes of tryptophan studied by terahertz time-domain spectroscopy," *Biophysical Journal*, vol. 86, pp. 1649–1654, 2004.